TECHNISCHE UNIVERSITÄT MÜNCHEN

Fakultät für Physik

Oskar-von-Miller Lehrstuhl für Wissenschaftskommunikation

Influence of Reaction Parameters on the Bottom–Up Synthesis of Two–Dimensional Polymers

Stefan Schlögl

Vollständiger Abdruck der von der Fakultät für Physik der Technischen Universität München zur Erlangung des akademischen Grades eines

Doktors der Naturwissenschaften
(Dr. rer. nat.)

genehmigten Dissertation.

Vorsitzender: Univ.-Prof. Dr. Martin Zacharias

Prüfer der Dissertation:

1. Univ.-Prof. Dr. Wolfgang M. Heckl
2. Univ.-Prof. Dr. Friedrich Simmel

"The only remedy for superstition is science."
"Das einzige Mittel gegen den Aberglauben ist die Wissenschaft."

Henry Thomas Buckle (1861)

from *History of Civilization in England*, 2nd vol., J.W. Parker & Son: London, p. 142.

Contents

List of Acronyms

(hkl)	Miller Indices of crystallographic planes like (100) or (111)
2D	Two-Dimensional
3-21G	DFT Basis Set
6-31G	DFT Basis Set
BLYP	Becke, Lee, Yang and Parr functional
CA	Ceperlay Alder functional
CC	Counterpoise Correction
CCD	Charge-Coupled Device
cc-pVTZ	correlation-consistent polarized Valence Quadruple Zeta
CGF	Contracted Gaussian Functions
COF	Covalent Organic Framework
DBPBA	3,5-DiBromoPhenylBoronic Acid
DFT	Density Functional Theory
FFT	Fast Fourier Transform
GGA	General Gradient Approximation
GTO	Gaussian Type Orbitals
HBr	Hydroxy-Bromine
HDT	Heatable Drift Tube
HOMO	Highest Occupied Molecular Orbital
HOPG	Highly Oriented Pyrolytic Graphite
KOH	Potassium Hydroxide Solution
LDA	Local Density Approximation
LEED	Low Energy Electron Diffraction
LT	Low Temperature
LUMO	Lowest Unoccupied Molecular Orbital
NMR	Nuclear Magnetic Resonance
PBE	Perdew-Burke-Ernzerhof functional
PCOT	PolyCycloOctaTetraene
PW	Plane Wave
PW92	Perdew-Wang 1992 functional
QMS	Quadrupole Mass Spectrometer
RT	Room Temperature
SSR	Surface Stabilized Radicals

STM	Scanning Tunneling Microscope
STO	Slater Type Orbitals
TBPB	1,3,5-Tris(4'-BromoPhenyl)Benzene
TBrB	1,3,5-TriBromo-Benzene
TBrTFB	1,3,5-TriBromo-2,4,6-TriFluoro-Benzene
TDBPB	1,3,5-Tris(3,5-DiBromoPhenyl)Boroxine
TeBrHFBP	3,3',5,5'-TetraBromo-2,2',4,4',6,6'-HexaFluoro-BiPhenyl
TIB	1,3,5-TriIodoBenzene
TIPB	1,3,5-Tris(4'-IodoPhenyl)Benzene
TITTF	Tetraiodotetrathiafulvalene
	(4,5,4',5'-Tetraiodo-2,2'-bis(1,3-dithiolylidene))
TPBHR	TriPhenylene-Boroxine-HexaRadical
TPD	Temperature Programmed Desorption
TTF	TetraThiaFulvalene
UHV	Ultra-High Vacuum

Abstract

As a matter of principle, silicon based micro-technological top-down production methods can lead to semiconductor devices with predefined electric and structural properties only. However, bottom-up synthesis in the field of nanotechnology can overcome these limitations. This fabrication method is used for the synthesis of tailor-made two-dimensional polymers with specific electric and mechanical properties. Within a retrosynthetic analysis, appropriate molecular building blocks and reaction pathways towards the desired (semi-) conducting polymer are designed.

In the work presented, essential reaction parameters and processes of *en route* or on-surface activation of molecular building blocks and their subsequent polymerization into two-dimensional networks are systematically studied under ultra-high vacuum conditions.

Scanning tunneling microscopy is the method of choice for real space characterization of on-surface synthesized polymers. The polymerization process is further scrutinized by means of low energy electron diffraction and mass spectrometry. Theoretical insights into two-dimensional polymers are gained by density functional theory calculations, which allow for the determination of structural and electric properties. Aromatic molecules consisting of phenyl rings and halogen functional groups are deposited onto catalytically active metal and inert graphite surfaces. In-crucible condensation reaction of boronic acid groups is used to synthesize molecules with increased complexity *in situ* prior to deposition. Both the catalytic ability of metal surfaces and thermal treatment of molecules on surfaces leads to activation through halogen homolysis reactions.

Experiments indicate that halogen atoms adsorbed on metal surfaces inhibit the polymerization reaction and hamper network growth. Different molecular building block sizes and geometries influence the two-dimensional polymer topology and can be used for tailoring structural and electronic parameters.

Moreover, substitution of pendant groups can influence the reaction pathway, although these side groups are not involved in the chemical reaction process. Self-assembly after dimerization of such molecules into ordered structures is explained by self-limiting recombination of molecules after partial dehalogenation of functional groups. Pre-activation and homolysis of the carbon-bromine bond of brominated phenyl rings prior to deposition is realized by a heatable drift tube, leading to halogen adlayers on an inert surface.

The presented insights enhance the knowledge of surface-mediated polymer synthesis and provide approaches for reliable reaction pathways of long-range ordered two-dimensional polymers.

Kurzzusammenfassung

Die siliziumbasierten *top-down* Produktionsmethoden in der Mikrotechnologie führen ausschließlich zu Halbleiterstrukturen mit durch das Material festgelegten elektrischen und strukturellen Eigenschaften. Jedoch kann die *bottom-up* Synthese aus dem Bereich der Nanotechnologie diese Einschränkungen überwinden. Hierzu wird diese Produktionsmethode auf die Synthese von maßgeschneiderten zweidimensionalen Polymeren mit entsprechenden elektronischen und mechanischen Eigenschaften angewandt. Mittels eines retrosynthetischen Ansatzes zur Analyse der gewünschten (halb-)leitenden Polymere werden passende molekulare Bausteine und Reaktionswege bestimmt.

In der vorliegenden Arbeit werden verschiedene Reaktionsparameter und Prozesse der oberflächenbasierten Aktivierung der molekularen Bausteine und ihrer anschließenden Polymerisation in zweidimensionale Netzwerke im Ultrahochvakuum systematisch untersucht. Rastertunnelmikroskopie ist die Methode der Wahl um die Polymere nach ihrer Synthese direkt auf der Oberfläche zu charakterisieren. Des Weiteren wird der Polymerisationsprozess mittels Beugung niederenergetischer Elektronen an Oberflächen sowie durch Massenspektrometrie untersucht. Theoretische Erkenntnisse werden mit Hilfe von Dichtefunktionaltheorieberechnungen gewonnen, welche Einblicke in mechanische und elektronische Eigenschaften der zweidimensionalen Polymere ermöglichen.

Aromatische Moleküle, welche aus Phenylringen und funktionellen Halogengruppen bestehen, werden auf katalytisch aktive Metalloberflächen und nicht reaktive Graphitflächen aufgebracht. Darüber hinaus wird eine Kondensationsreaktion von Boronsäuregruppen direkt im Aufdampftiegel genutzt, um komplexere Moleküle zu synthetisieren. Die Homolyse der Halogenatome und somit die Aktivierung der Moleküle erfolgt entweder durch die katalytische Aktivität der Metallatome oder durch eine thermische Nachbehandlung. Die durchgeführten Experimente legen den Schluss nahe, dass auf Metalloberflächen adsorbierte Halogenatome die Polymerisationsreaktion beeinträchtigen und somit das Netzwerkwachstum behindern. Verschiedene Größen und Geometrien der molekularen Bausteine beeinflussen die Topologie der zweidimensionalen Netzwerke und können darüber hinaus auch gezielt für gewünschte strukturelle und elektronische Eigenschaften eingesetzt werden.

Eine Substitution der Seitengruppen beeinflusst ebenfalls den Reaktionsweg, obwohl diese Seitengruppen nicht direkt an der chemischen Reaktion beteiligt sind. Die Selbstassemblierung dieser Moleküle in geordneten Strukturen wird mittels einer partiellen Dehalogenisierung funktioneller Gruppen und anschließender selbstbegrenzender Rekombination zu Dimeren erklärt. Homolyse und Aktivierung von Kohlenstoff-Brombindungen von bromierten Phenylringen, bevor die Moleküle die Oberfläche erreichen, wird mittels eines heizbaren Driftrohres erreicht. Dadurch werden Halogenmonolagen auf inerten Oberflächen erzeugt.

Die gewonnenen Einblicke erweitern das Wissen über die oberflächenbasierte Polymersynthese und ermöglichen Ansätze zur zuverlässigen Synthese langreichweitiger, geordneter zweidimensionaler Polymere.

Chapter 1

Introduction

The realization of two-dimensional structures through bottom-up synthesis is a major goal in surface science. This process enables the creation of new classes of materials and semiconductors with tailor-made electronic, thermal, and mechanical properties. To also ensure stability and rigidity of these structures under ambient conditions, the covalent interlinking ability of polymers is stringently required.

Groundbreaking experiments regarding Graphene, the most famous and best studied two-dimensional polymer consisting just of one single layer of graphite, were awarded with the Nobel Prize for Geim and Novoselov in 2010 [107, 108]. However, this material with outstanding electric properties is still far away from industrial utilization. Until now super fast integrated circuits based on frequencies up to $100\,GHz$ were realized under research conditions only by IBM [68]. Economic exploitation of the gained knowledge will be delayed to the future, but nevertheless important first steps towards industrial applications are made. A recent publication by Jeon et al. shows solutions for possible large scale production of functionalized graphene nanoplatelets [72].

In research laboratories around the world recent work goes beyond graphene towards new classes of materials with extended properties like higher strain resistance [66] or an opening of an energy band gap through functionalization [42]. As a direct successor to graphene a carbon allotrope with non-zero bandgap was proposed by Brunetto et al. [21].

Hydrogen storage capability of Li doped polyphenylene was theoretically shown by Du et al. [40], while the application of so called porous graphene as a nanofilter was proposed by Blankenburg et al. [18]. More extended graphene nanoribbons based on polyphenylene were synthesized via a bottom-up oxidative cyclodehydrogenation that resulted in long-range ordered structures with defined electric band gaps in the infrared regime [135]. Also new classes of two-dimensional polymers like hexagonal boron-nitride films were synthesized by Ismach et al. [70] and other groups [33, 152]. Moreover, covalent functionalization of boron-nitride films reinforces the polymer and provides additional stress transfer by interactions between hydroxy functional groups [127]. Furthermore, theoretical preliminary work for borene structures equivalent to graphene have also been carried out by Ismail-Beigi and Tang [147, 146]. Another

approach to further alter the physical and chemical properties of graphene is the regular substitution of carbon atoms with nitrogen atoms to form so called carbonitride layers [77]. Computer modeling was done by Alves [2] and Du [39], while experimental work towards the synthesis was performed by Döblinger et al. [37] and Lotsch et al. [88, 87] through a synthesis pathway from triazines to heptazines as templates that could ultimately lead to crystalline carbon nitride C_3N_4 phases. Tailor-made surface-based nanostructures also facilitate nano-masks for lithography [30] or capturing CO Molecules [166]. The synthesis of more complex nanostructures can be achieved by sequential step-by-step interlinking of more elaborate covalent building blocks which could ultimately lead to electronic circuits [80, 27].

Furthermore the class of polyphenylenes, so called porous graphene [117, 128, 54, 84, 15, 86] as well as phenylene-boroxine layers with new electronic and physical properties were studied excessively [67, 35, 34]. This thesis is based on that knowledge and enhances the understanding of the synthesis process of two-dimensional polymers, since realization of all possible applications requires first and foremost profound insights into basic processes. To reach that goal, different approaches and their decisive influence parameters are studied in order to gain knowledge about fundamental mechanisms and their physical as well as chemical properties. Ultimately an overall concept towards tailor-made controlled and fully understood bottom-up synthesis shall be developed. Of course the overall concept is not completed by this work, but basic pieces for a full understanding are delivered. To accomplish this task, a surface science approach is chosen. Towards tailor-made polymers theoretical preliminary work is done by retrosynthetic analysis: A desired polymer structure is split into chemically suitable monomers, which can be used as molecular building blocks. Furthermore, a possible synthesis route based on activation of these monomers with protection groups either *in situ* on-surface or during deposition (*en route*) or storage (*ex situ*) is developed. Different ways of bottom-up synthesis were performed and studied experimentally to gain insights into each separate reaction step and to analyze the important influence parameters. Since experimental synthesis usually yields only short-range ordered two-dimensional structures with high defect densities, an analytic tool for imaging the structures with sub-molecular resolution is required. This analysis was performed in real space by a scanning tunneling microscope. Studies on long-range ordered two-dimensional polymers were supported in reciprocal space by imaging of low energy electron diffraction as a complementary method.

The present thesis is structured as follows: In chapter 2 the theoretical background of surface chemistry, molecule–surface interactions, and density functional theory is delivered. Next, the experimental setup and scanning tunneling microscopy is explained in detail in chapter 3, while the first five sections in chapter 4 concentrate on one important parameter of the synthesis process. In the last section of chapter 4 a new fully conjugated polymer and a related reaction pathway is proposed. A basic conclusion with a schematical classification of synthesis processes is provided in the last chapter.

Chapter 2

Theoretical Background

This chapter mainly focuses on the surface chemistry of larger molecules. Moreover, the chemical properties of molecular building blocks and their corresponding functional groups are highlighted. In the last section an overview of density functional theory is given. The whole chapter provides the foundation for an understanding of the experimental work on bottom-up synthesis of two-dimensional polymers.

2.1 Surface Chemistry

2.1.1 Polymerization

For polymerization chain-growth and step-growth reactions have to be distinguished [46]. In a chain-growth polymerization unsaturated monomers add subsequently to growing polymers:

$$C=C(\text{monomer}) \longrightarrow (-C-C-)(\text{polymer}) \tag{2.1}$$
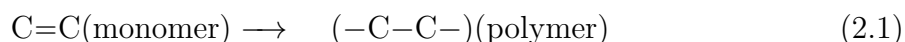
Characteristic for chain-growth polymerization is the requirement of an initiator to start and a termination linker to stop the reaction. For surface-mediated synthesis of polymers into two dimensions step-growth polymerization is important. In order to start and stop the step-growth polymerization, no initiator is required and no termination exists.

In both cases growth of polymers with two-dimensional network topologies can occur, where already existing polymer branches can further grow to larger interconnected polymers. The structure of monomers is an important factor to control and influence the topology of the resulting polymer branches which ultimately lead to two-dimensional polymers.

When referring to reaction mechanisms, one has to distinguish between a polycondensation and a polyaddition reaction, which was firstly classified by Carothers in 1929 [24]. Polycondensation is defined as a reaction where the structural formulas of the monomer and resulting polymers are different, because byproducts with small molecular weight like water molecules are released during the reaction. In this work

cyclo-condensation reactions of boric acids to boroxine rings are investigated:

$$3\,R{-}B(OH)_2 \longrightarrow \quad (RBO)_3 + 3\,H_2O \tag{2.2}$$
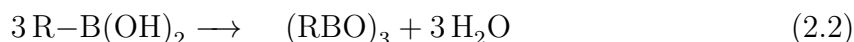
where boroxines emerge after dehydrogenation of boronic acid groups.

In contrast to that, a polyaddition reaction has identical molecular formulas of monomer and polymer as can be seen in equation 2.1.

2.1.2   Homolysis

In the synthesis of two-dimensional polymers protection groups linked to organic backbones are required to inhibit uncontrolled reactions. In order to split off functional protection groups, a homolysis reaction under controlled conditions is needed. Both reaction products, the protection group and the backbone, can undergo further reactions afterwards. By breaking a covalent bond in a homolysis process, a neutral molecule is dissociated into free radicals with one unpaired electron each:

$$A{-}B \longrightarrow \quad A^{\cdot} + B^{\cdot} \tag{2.3}$$

Also di-, tri- or tetraradicals can emerge, if more than one protection groups of the same molecule is split off.

2.1.3   Performed Polymerization Reactions

A polymerization in this work is initiated by a unimolecular reaction where monomer radicals result from the original molecule by a homolysis reaction of their functional groups. These radicals further undergo a polymerization reaction to form polymers in a chain-growth process depending on the topology and functionality of the original molecular backbone. At least two monomer radicals $A^{\cdot}$ polymerize in a radical recombination reaction to form dimers:

$$2\,A^{\cdot}(\text{monomer}) \longrightarrow \quad (A{-}A)(\text{dimer}) \tag{2.4}$$
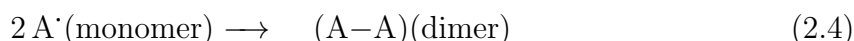
The more general case is the subsequent addition of monomer radicals with more than one active site to the polymer chain:

$$(-A-)_n(\text{polymer}) + A^{\cdot\cdot}(\text{monomer}) \longrightarrow \quad (-A-)_{n+1}(\text{polymer}) \tag{2.5}$$
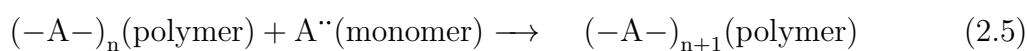
Within the framework of step-growth and chain-growth polymerization, the synthesis of two-dimensional polymers is best stated as *branch-growth polymerization*, since the two-dimensional polymers must not be limited to molecular chains by definition. A special case of the synthesis of dimers is the Ullmann coupling reaction [154, 163], where aryl halides undergo a dehalogenation process with Cu atoms in an intermediate step and ultimately form biphenyls in a second reaction step. The surface mediated Ullmann coupling was described by Blake in 2009 [17], where biphenyls and surface-bonded bromine atoms could be detected with a STM. Special active sites on the

Cu(111) surface enhance dissociative chemisorption of the halides: At first, aromatic halides adsorb on the Cu(111) surface. At elevated temperatures, dissociation of the C−Br bond occurs and bromine adlayers are formed at the surface through chemisorption. In an intermediary step the active sites of phenyl rings bind to the copper surface, while in a last step two phenyl-radicals recombine to biphenyls. Intermediate radical monomers bind to the surface and form so called *surface stabilized radicals (SSR)*. SSRs can be seen as intermediate steps towards polymers [106], before they recombine to two-dimensional polymers [14].

2.2 Molecular Interactions

Appropriate molecules with well defined structures are needed for tailoring two-dimensional polymers. The structure includes the backbone as well as the functional or protection groups. In the pursued synthetic approach, two-dimensional monomers with coplanar functionalization adsorb on the surface before they polymerize into two-dimensional polymers. A main overview of possible bottom-up synthesis strategies of two-dimensional polymers can be found in figure 2.1. The structure and functionality (equals the amount of reaction sites) of the initial monomer building block mainly determine the resulting polymer.

In this work molecules with equal and different types of functional groups were studied. For a desired polyaddition reaction under controlled conditions molecules with equal functional groups have to undergo an on-surface homolysis reaction of the functional groups in a first step, which lead to the formation of SSRs. These monomers then undergo branch-growth polymerization to form dimers, trimers and oligomers. Depending on the structure of the monomers, these reactions can lead to one-dimensional chains or to two-dimensional polymers.

Molecules with two different kind of functional groups can undergo two subsequent independent reactions. In this work experiments with molecules consisting of bromine atoms and boronic acid groups were performed. For this case a polycondensation reaction regarding boronic acid leads to trimers interconnected by boroxines. In a second step remaining bromine functional groups of the newly synthesized trimers can split off and undergo subsequent polymerization reactions resulting in polymers with a more complex topology.

In the present thesis functionality refers to the number of active sites after one single reaction step regarding one kind of functional group only. So each possible subsequent reaction step has its specific functionality.

2.2.1 Molecular Building Blocks

Phenyl rings and Polyphenylene

Up to now extensive studies were performed on polymerized phenyl rings, i.e. polyphenylene [14, 19, 50, 54, 55, 59, 117, 128, 158, 161]. Polyphenylene polymers (also called *porous graphene*) can be viewed as graphene sheets with regularly
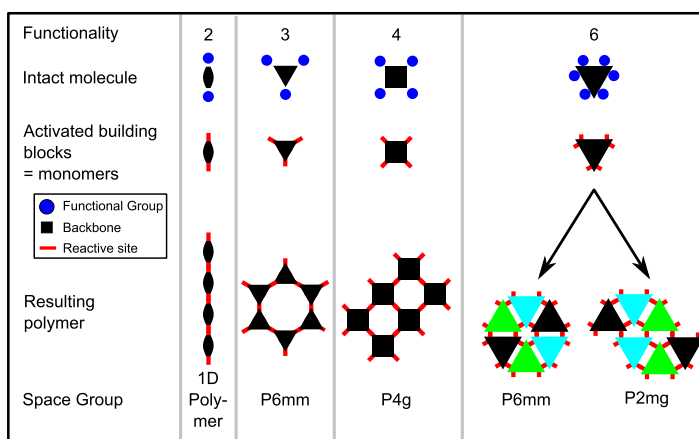
Figure 2.1: Overview of bottom-up synthesis of different monomers into their ideal polymers. The functionality is the important parameter that determines the topology of the polymer. For *two*, *three*, *four* and *six* functional groups examples of two-dimensional polymers with their plane symmetry group are given in the figure, respectively. For the functionality *six* two different stacking orders can occur with a high symmetry 2D space group (*P6mm*) and one with a lower symmetry group (*P2mg*). Different stacking orders of the backbones are highlighted by colored triangles. Functional (protection) groups are indicated by blue colors, the backbones are black and the reactive sites are shown by red color.

removed carbon atoms and hydrogen saturation of the resulting pores (cf. figure 2.2(a)). In the literature also the reverse reaction from polyphenylene to graphene by cyclodehydrogenation of cyclohexaphenylene to tribenzocoronene and corresponding dehydrogenation of polyphenylene to graphene was described [153].

Extended polyphenylene consists of threefold phenyl rings in a hexagonal arrangement interconnected by each two additional phenyl rings on opposite (para) sites serving as spacers (cf. figure 2.2(b)).

According to the polymer structure, different electronic and mechanical properties can be achieved. Graphene is known to be a zero band gap semiconductor [50], while porous graphene has a band gap around 3.3 eV according to DFT calculations [21]. Slight alterations in the topology and atom distribution of the polymers have a huge impact on electronic properties.

Boroxine Rings

Another parameter in the synthesis of two-dimensional polymers is the type of atoms. By exchanging one third of the phenyl rings to boroxine rings in porous graphene, phenylene-boroxine is formed (cf. figure 2.2(c)). Depending on the distribution of boroxine rings in the polymer, two stacking orders with different symmetry groups occur (cf. functionality six in figure 2.1). Yaghi et al. were the first to introduce boroxine chemistry to the synthesis process of covalently bonded molecules in the year 2005 [34] and a lot more related work followed [76, 101, 111, 167, 45]. DFT calculations of the HOMO-LUMO band gap of phenylene-boroxine networks yield an approximate value of 2.8 eV. The whole band structure is different to that of
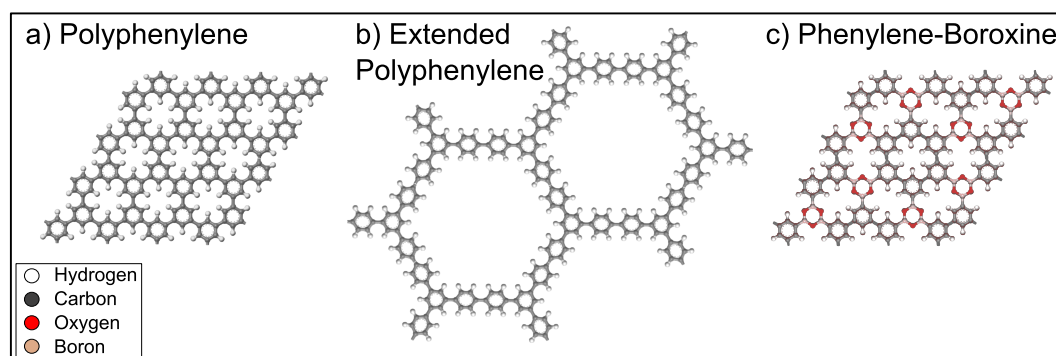
Figure 2.2: (a) Polyphenylene (also called porous Graphene, since one half of all phenyl rings are removed and the pores are saturated with hydrogen). (b) Extended polyphenylene with an additional phenyl ring serves as a linear spacer between phenyl rings with three reactive sites in a threefold symmetry. (c) Phenylene-boroxine consists of polyphenylene with an substitution of one third of phenyl rings with boroxine rings. All structures belong to the plane crystallographic group *P6mm*.

porous graphene [130]. Experiments were performed with a phenyl ring with two bromine functional groups and one boronic acid group. In principle the molecule has a functionality of three, but after the first reaction step a polycondensation reaction of each three molecules occurs. This gives a boroxine ring with three remaining phenyl rings, each with two remaining bromine atoms. So after this first reaction step the functionality of the newly formed molecule is six.

2.2.2   Role of Functional Groups

The number of functional groups classifies the chemical functionality of the monomer, i.e. the number of possible reactive sites of a monomer. *One* functional group limits the reaction to dimer synthesis, while a functionality of *two* already allows the formation of one-dimensional polymer chains. Higher functionalities ultimately lead to crosslinking between different branches and may result in fully crosslinked two-dimensional polymers. Experiments performed with boronic acid groups undergo a polycondensation reaction and are part of the resulting polymer (see section 2.2.1). Other experiments were conducted with functional groups acting as leaving groups and therefore are not part of the final polymer structure. Nevertheless, these functional groups have a huge impact on the on-surface polymerization process: Split-off atoms or molecules can bind strongly to the surface. Through blocking of the surface, the split-off atoms limit the free movement of the monomers and polymers and inhibit further polymerization reactions. Detailed studies were performed regarding this aspect. In the present thesis studies of functional groups and their impact on the polymerization process were performed with halogen substituents like bromine (-Br) (see section 4.1, 4.5) and iodine (-I) (see section 4.2, 4.3). In one example hydrogen atoms were replaced by fluorine (-F) (see section 4.4), so fluorine served as a side- or pendant group.
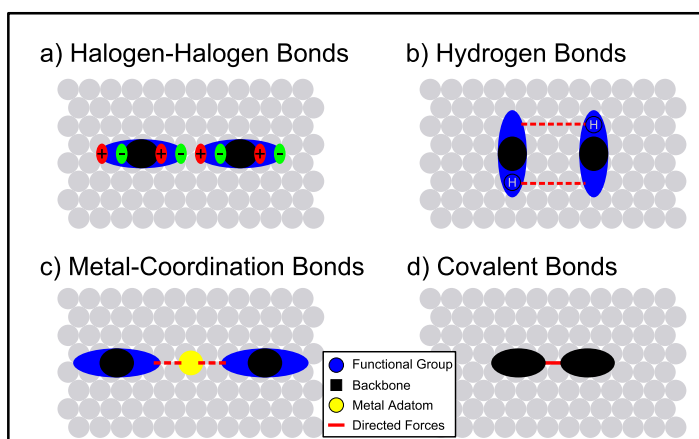
Figure 2.3: Intermolecular interactions of molecules at surfaces: (a) Molecules with polar functional groups (i.e. halogen atoms) can interact via dipole or quadrupole moments. (b) Hydrogen bonds occur between hydrogen atoms and electronegative functional groups or backbones. (c) Metal coordination bonds are formed between organic molecules and metal adatoms staying on top of the crystal surfaces (d). Covalent bonds evolve after overlapping of electron orbitals of different atoms. Binding energies increase from (a) to (d)). The scheme is related to a review article of Bartels [6].

2.2.3 Intermolecular Interactions at Surfaces

In the following section, intermolecular interactions necessary for the synthesis process of two-dimensional polymers are shown in figure 2.3 and will be discussed in more detail. Further considerations can be found in a review of Bartels [6].

Halogen–Halogen Bonds

Halogen bonds can be seen as directional electro-statically driven interactions between two or three halogen atoms [118] or between halogen atoms and hydrogen atoms [110]. The basics of van der Waals and dipole forces have already been described in 1939 by Margenau [92], but only in recent years halogen bonds became directly observable on surfaces. A theoretical description of triangular halogen-halogen-halogen bonds between trihalomesitylene molecules is given by Bosch [20]. The origin of the forces lies in a non-spherical charge distribution at the halogen atoms, where induced dipoles lead to electrostatic forces between positive end caps and negative rings around the halogen atoms. Even fourfold halogen bonds were discovered [29]. In conclusion, halogen atoms interact via specific and directed forces with reported binding energies up to 33 kJ/mol [31].

Hydrogen Bonds

A hydrogen bond is an electrostatic donor-acceptor interaction between hydrogen atoms attached to a chemical group and electronegative atoms such as nitrogen, oxygen or fluorine of other molecules. They have typical binding energies between 5 kJ/mol and 40 kJ/mol [97]. The binding force is effective between hydrogen atoms

with a positive partial charge and the electron pair of the electronegative atom. Therefore, hydrogen bonds are also called polar. In self-assembled monolayers with functional groups containing hydrogen atoms attached to electronegative atoms (such as carboxylic acids [78]), hydrogen bonds play an important role in intermolecular interactions [71].

Metal–Coordination Bonds

Metal coordination bonds are classified as interactions between an organic adsorbate, a metal adatom at a surface and another organic adsorbate and have binding energies up to 100 kJ/mol [95, 131]. The organic substrates are coupled via the metal adatoms to each other. The bond can be separately controlled and induced by the varying amount of the adatom gas through controlling the temperature [6]. Typical metal–coordination bonds occur between carboxylic acids and Cu-adatoms at a Cu(100) surface [85] or between cyano groups and Co-adatoms at Ag(111) [131]. Other examples are hydroxyl groups binding to Fe- [82] or Ni-adatoms [143].

Covalent Bonds

Covalent bonds were first classified by Langmuir in 1919 [81], where the term covalent arises from the sharing of (mostly delocalized) electrons. Covalent bonds are also named after the overlapping of different electron orbitals like $\sigma-$ or $\pi-$bonding. Covalent bonds are directed, rigid, and stable (binding energies higher than 200 kJ/mol) and play the most important role in the bottom-up synthesis of two-dimensional polymers through polymerization reactions of monomers. Their strong bonding can facilitate strong electron interactions leading to (semi-)conducting behavior [54, 128, 79, 93]. Unfortunately, no controllable cleaving and recombination process of specific bonds in a 2D polymer exists to heal defects.

Adlayer Formation

The split-off of halogen functional groups, i.e. leaving groups, can lead to adlayer structures. In the literature numerous examples of halogen adlayer structures, mainly bromine and iodine on metal surfaces like Ag(111) or Cu(111), can be found [62, 69, 134, 41, 110]. These adlayers form strong bonds to the metal surface and often a harsh treatment with annealing to high temperatures or even gas ion sputtering is needed to remove the halogen atoms from the surface [102]. As described in subsection 2.2.2, smaller adlayer coverages of the surface can hamper the polymerization reaction, while high adlayer coverages completely inhibit network growth.

2.3   Density Functional Theory

DFT calculations were performed to deepen the understanding of reaction processes. Geometry and energy optimizations of molecules and polymers were used to calculate

electronic and structural properties of polymers (see section 4.1), to calculate defect probabilities (section 4.2) and to reveal intermediate reaction steps (section 4.3).

2.3.1   Historical Evolution of DFT

Following the perspective of Mattsson [94], the development of DFT can be summarized following its historical evolution.

The Hohenberg-Kohn theorem is a simplification of Schrödinger's equation, where a non-interacting many electron system generates the same electron density as an interacting system. This equivalence of the electron density is facilitated by converting the problem of interacting electrons moving in an external ion potential into a problem of non-interacting electrons moving in an effective potential [65].

Derived from Hohenberg-Kohn theorem, the Kohn-Sham equations describe how N independent electrons move in an effective potential v_{eff} [75]:

$$\left(-\frac{1}{2} \cdot \nabla^2 + v_{eff}\left(\vec{r}\right) - \epsilon_j\right) \phi\left(\vec{r}\right) = 0 \tag{2.6}$$

with the orbital energy ϵ_j of the Kohn-Sham orbital. The sum of all single independent electron densities leads to the total electron density:

$$n\left(\vec{r}\right) = \sum_{j=1}^{N} \|\phi_j\left(\vec{r}\right)\|^2 \tag{2.7}$$

The total energy of the system is a unique function of the electron density with an equivalence of the ground state energy to the variational energy minimum, which can be calculated by computational methods. So there is no need to compute the complex many-body wave functions, because the ground state energy can be also derived from the electron density [137]. Since v_{eff} is dependent on the density, a self-consistent approach is required, where the effective potential is separated into an external potential $v_{ext}\left(\vec{r}\right)$, the electrostatic Hartree term $\int \frac{n(\vec{r})}{\|r-r_j\|} d^3\vec{r}$ and the exchange correlation term $v_{xc}\left(\vec{r}\right)$ for the many electron system. The first two parts are classical terms that can be exactly computed, while the last part, the exchange correlation term, incorporates many particle interactions and quantum effects, where up to now no exact solution can be calculated. To find this *divine* exchange-correlation functional is the ultimate goal in computational chemistry [74, 165].

2.3.2   Jacob's Ladder

To classify the development of density functional theory, Perdew suggested to apply Jacob's Ladder to the hierarchy of DFT approximations in finding the *divine* exchange-correlation functional [115, 94]. All subsequent steps include the main aspects of the former ones, but expand the system by adding capabilities.

1. The first rung of the ladder is the local density approximation (LDA) where only the local density is important. This simplification is sufficient for systems, where

the density is everywhere the same (like for metals), but leads to overbinding in molecules. Example functionals are Ceperlay-Alder (CA) [25] or Perdew-Zunger (PZ) [116].

2. As an extension to include not only the local density, but also the gradient, the general gradient approximation (GGA) was introduced. Some examples of GGA functionals are BLYP [8], Perdew-Burke-Ernzerhof (PBE) [112] or Perdew-Wang PW92 [112, 113].

3. The third rung are metaGGAs, which include also the Laplacian ∇^2 of the density (derivative of the derivative term of LDA), like the TPSS functional [148], which is not widely used, or the PKZB functional [114]. All three rungs are multiplicative and local, since only different orders of derivatives of the local density are used.

4. The fourth rung introduces non-locality by using the exact Hartree-Fock exchange energy, which leads to so called hyperGGAs like the B3LYP functional [9, 10]. These hybrid functionals are superior in terms of accuracy for small covalent systems (like single molecules) [109], but give poor predictions for weaker non-covalent bonds (like van der Waals forces) or systems with free electrons (like metals). Moreover hybrid functionals are slow in computation for large systems with many atoms [165].

5. The final fifth rung is unreached up to now, but it provides absolute accuracy by exact exchange and correlation functionals, where (un)occupied states in the Kohn-Sham equations can be completely described [94]. Until now there are only semi-empirical suggestions (like XYG3) for the fifth rung functionals [165].

2.3.3   Basis Sets

The basis set is a set of functions which are linearly combined to create wave functions as solutions for molecular orbitals and to solve the Kohn-Sham equations in an iterative self-consistent procedure. The basis sets play an indirect role in the Kohn-Sham equations 2.6 only. They are used to calculate the electron density, from which the ground state energy of the system can be computed.
In principle, three different types of basis sets exist: Gaussian type orbitals (GTO), Slater type orbitals (STO) and plane waves. The latter ones are not in compliance with the linear combination of atomic orbitals, instead plane waves are a solution to the Schrödinger equation of the free particle:

$$\eta^{PW} = e^{i\vec{k}\vec{r}} \tag{2.8}$$

This is the simplest and most general form to describe atomic orbitals, where the plane waves extend throughout the space. Therefore one needs periodic boundary conditions to use a plane wave basis set.

The STOs are exact wave functions as a complete set of orthogonal eigenfunctions with an exponential decay $e^{-\zeta r}$ of the radial part and spherical harmonics Y_{lm} for the angular parts:

$$\eta^{STO} = N \cdot r^{n-1} \cdot e^{-\zeta r} \cdot Y_{lm}(\Theta, \phi). \tag{2.9}$$

Unfortunately STOs are hard to implement and require much computational effort. As a rule of thumb one needs three times as many GTOs than STOs to reach the same accuracy, but GTOs are much simpler to implement. Cartesian GTOs are approximate wave functions with separated terms for the three dimensions x, y, z with the spin quantum numbers $L = l + m + n$, the Gaussian term $e^{-\alpha r^2}$ and a normalization factor N:

$$\eta^{GTO} = N \cdot x^l \cdot y^m \cdot z^n \cdot e^{-\alpha r^2}. \tag{2.10}$$

One can influence the spatial extension (i.e. compactness or diffusiveness) of the radial part with the parameter α and therefore change the computational effort, where efficient algorithms exist. The main choice are so called contracted Gaussian functions (CGF), which are a linear combination of GTOs.

The easiest, but least accurate basis set is the $STO - 3G$ with one basis function for each atomic orbital. Moderate accuracy results from the use of Pople or double-ζ basis sets with two functions per orbital, which are limited to the valence electrons. Examples are the split valence sets of $3 - 21G$ or $6 - 31G$ with 6 Gaussian cores for the X dimension and 3 for Y and 1 valence orbitals for the Z dimension. More sophisticated basis sets like cc-pVTZ include up to 91 CGFs and stand for *correlation-consistent polarized valence quadruple zeta* [74].

2.3.4 Computational Realization of DFT

Energy calculation and geometry optimization of molecules is done with different codes, which implement the ideas of DFT and provide a comfortable framework for performing calculations with specific basis sets and functionals. In the present work the CASTEP code implemented in the software *Accelrys Materials Studio 5.0* was utilized to perform calculations regarding polymer structures with periodic boundary conditions, while the GAUSSIAN code was applied to reveal intermolecular distances of single molecules.

CASTEP Code

The CASTEP code uses plane waves and pseudopotentials. Therefor periodic boundary conditions are obligatory, making the code very suitable for band structure calculations of two-dimensional systems of crystalline structures in x- and y- dimension. The extension into the third dimension necessary for periodic boundary conditions is done by creating a vacuum slab via stacking of layers into z-direction fulfilling the condition $c \ggg a \lor b$ (a, b, c are lattice parameters in x-,y-,z-direction).

Functionals like PW92 or CA implemented in LDA or GGA can be used with plane wave basis sets [137].

GAUSSIAN Code

GAUSSIAN is a chemical computation software that uses Gaussian type orbitals to speed up the calculation. It implements many functionals and basis sets and is in this work solely used for geometry optimization and total energy calculations of isolated molecules without periodic boundary conditions. Code versions GAUSSIAN03 [47] and GAUSSIAN09 [47] were utilized.

2.3.5 Basis Set Superposition Error and Counterpoise correction

The basis set superposition error is a binding energy miscalculation in quantum chemistry. An artificial strengthening of the bonds between two monomers can occur if each monomer utilizes the electron wave functions of one another, although the overlap integrals are in fact too small. So the binding energy is too large and has to be corrected by a so called counterpoise correction (CC). For more information notice a review article by Sherril [139]. The CC was used in the literature to approximate the real binding energies in hydrogen bonded dimers [141], but also intramolecular interaction corrections were performed for benzene molecules [4, 155]. In this work the CC is utilized to calculate the differences in binding energies for the C−Br bond of 1,3,5-tribromo-2,4,6-trifluoro-benzene (TBrTFB) for the intact molecule and after bromine removal. Thereby a possible electron withdrawing effect (*minus inductive effect*) of fluorine will be excluded. Further information is provided in section 4.4.

Chapter 3

Experimental Methods

In order to study the physics and chemistry of the synthesis of two-dimensional materials, one follows best a so called surface science approach defined by Nobel laureate Irving Langmuir in 1936 [43]. If a problem is too complex to understand in full, it has to be reduced to smaller problems under some constraints. In this case the polymer synthesis is restricted to well defined metal surfaces under ultra-high vacuum conditions and analyzed by sensitive scanning tunneling microscopy measurements on the nanoscale. After introducing the basic principles of the scanning tunneling microscope, the experimental setup including an ultra-high vacuum chamber is presented.

3.1 Scanning Tunneling Microscopy

3.1.1 Basic principles of vacuum tunneling

Electronic tunneling between two separated conductors is based on quantum mechanics and was reviewed and discussed from a many particle view by Bardeen [5]. Although vacuum tunneling is a general theory which can be applied to many systems consisting of at least two separated materials, the theory in the present thesis shall be described in the context of a scanning tunneling microscope. A simple one-dimensional model describing the STM uses a tunnel barrier with sample and tip separated by a vacuum barrier of width d. Both sample and tip have the same work function φ. The Fermi-levels are shifted by an energy eV where a voltage V is applied either to the tip or to the sample. An exponential decay lowers the amplitude of the incident wave ψ_{in}, but the energy of the outgoing wave ψ_{out} stays the same (see figure 3.1). Tersoff and Hamann [150] were the first to provide a quantitative theory for the tunneling current between the tip and the sample in the context of a STM. One can apply first-order perturbation theory to describe the tunneling current

$$I_{tunnel} = \frac{2\pi e}{\hbar} \sum_{\mu,\nu} f(E_\nu) \left[1 - (E_\nu + eV)\right] \times |M_{\mu\nu}|^2 \delta(E_\mu - E_\nu) \tag{3.1}$$

with the Fermi function $f(E)$ and the transition tunneling matrix elements $M_{\mu\nu}$.
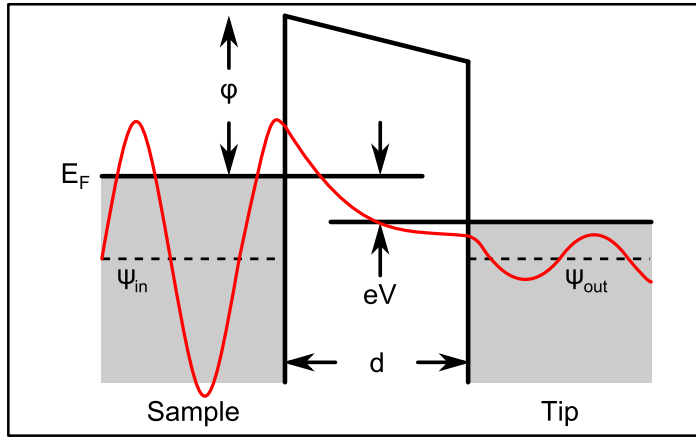
Figure 3.1: One-dimensional tunnel barrier with sample and tip separated by a vacuum barrier of width d. Both sample and tip have the same work function φ. The Fermi-levels were shifted by a voltage V. An exponential decay lowers the amplitude of the incident wave ψ_{in}, but the energy of the outgoing wave ψ_{out} stays the same.

This equation can be simplified by accounting only small applied voltages and low temperatures to

$$I_{tunnel} = \frac{2\pi e^2 V}{\hbar} \sum_{\mu,\nu} |M_{\mu\nu}|^2 \, \delta \left(E_\mu - E_F \right) \delta \left(E_\nu - E_F \right) \qquad (3.2)$$

The significant term in the equation is the tunnel matrix $(M_{\mu\nu})$. Bardeen [5] gives the following surface integral for the single matrix elements:

$$M_{\mu\nu} = \frac{\hbar^2}{2m} \int d\vec{S} \cdot \left(\psi_\mu^\star \nabla \psi_\nu - \psi_\nu \nabla \psi_\mu^\star \right) \qquad (3.3)$$

where the integral goes over an arbitrary separation surface lying in the vacuum barrier between tip and sample. To insert an appropriate wave function one needs to know the tip geometry. The Tersoff and Hamann model [150] uses a locally spherical shape of the tip, which is illustrated in figure 3.2. Another derivation of this simplified model was done by Chen in 1990 [28]. There he confirms the Tersoff-Hamann model and shows that in a first approximation it is sufficient to use s-wave functions only to describe the spherical shape of the tip. Using wave functions with higher order quantum numbers just bring a marginally improved description of the tunneling process and can be neglected for a basic model.

If one inserts equation 3.3 in equation 3.2 and one follows the calculations of Tersoff and Hamann [150] and uses typical values in the range $0.3 - 0.9\,\text{nm}$ for the tip-sample distance and the radius of the tip atom, the tunneling current is proportional to

$$I \propto V \rho_{tip} \left(E_F \right) e^{2kd} \rho_{sample} \left(E_\nu - E_F \right) \qquad (3.4)$$
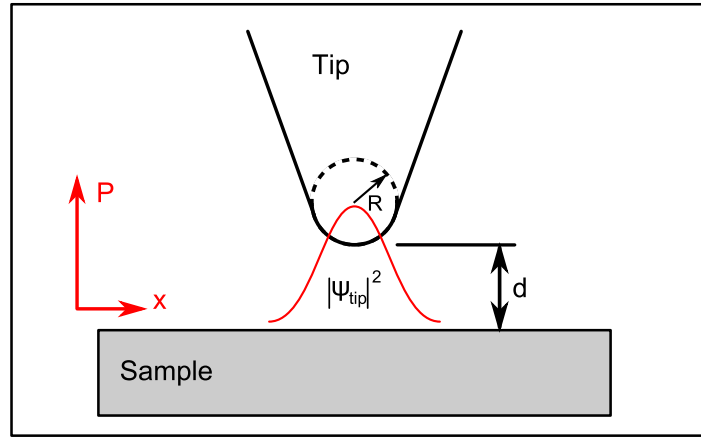
Figure 3.2: Tersoff-Hamann approximation: only s-wave functions of a spherical tip apex are accounted for the tunnel matrix elements. An ideal tip with a sphere of radius R and distance d from the sample is assumed. Red: Probability density function of electrons around the tip.

with the local density of sample states near the Fermi level

$$\rho_{sample}\left(E_\nu - E_F\right) = \sum |\psi_\nu(r_0)|^2\, \delta\left(E_\nu - E_F\right). \tag{3.5}$$

Because of the exponential decay $I \propto e^{2kd}$ the current is very sensitive to the tunneling distance d. For typical values a vertical resolution of $\sim 0.01\,\mathrm{nm}$ can be achieved. The lateral resolution is around $0.1\,\mathrm{nm}$, so individual atoms can be imaged by the STM. Within this Tersoff-Hamann model the conductance of a STM at low temperature and low applied voltages is proportional to the local density of sample states in a region at the center of the tip [28].

A more elaborate discussion of the basics can be found in a review of Gottlieb [52].

3.1.2   Experimental Setup

In this subsection the practical realization of the utilized STM setup is shown. The first practical realization of a STM was done by Nobel laureates Binning and Rohrer in 1982 [16]. The experimental setup can be divided into three different units: image processing, feedback loop, and tunneling (see figure 3.3 for more details).

All relevant components like the coarse approach of the tip, the specific STM unit, the housing setup implemented in a vacuum chamber and the feedback loop controller are described in more detail in the following paragraphs.

Piezoelectric Effect

In order to map the nano regime, an important component is a reliable nano positioner with sub-nanometer resolution. Piezoelectric ceramics are the ideal candidates to fulfill these requirements. The piezoelectric effect is the capability of certain piezoelectric ceramic crystals to change physical dimensions in an electric field. Also
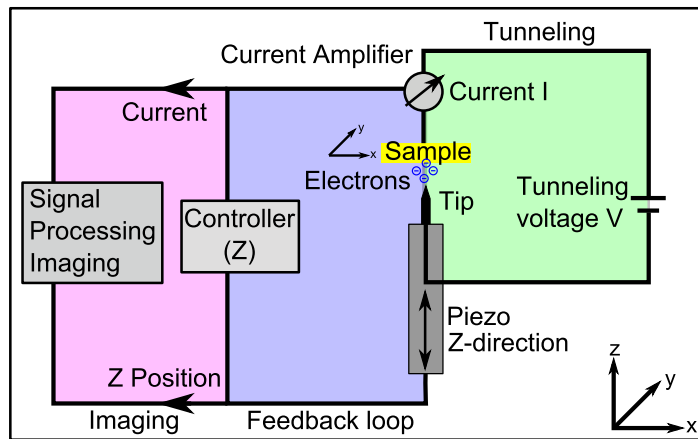
Figure 3.3: Experimental STM Setup: A voltage is applied to the tip. At tip-sample distances in the range of less than one nanometer a tunneling current is measured and amplified (green area). Deviations in the tunneling current are used in a feedback controller to keep the tip-sample distance or the current constant. Therefore a voltage is applied which expands or compresses the piezo along the z-axis to follow the sample topology and keep the tunneling current constant, while additionally applied voltages move the tip in x- and y-direction above the surface (blue area). Information about the current and the z-position are recorded and processed by a computer, which compiles the actual topography of the sample (pink area).

the reverse effect is possible to induce an electric field by mechanically changing the size (i.e. to impose stress on the ceramic). Electricity is induced by stress *et vice versa* [61]. In a STM setup a voltage is applied to a piezoelectric ceramic to induce a change in length and to move the tip.

This piezoelectric ceramic has the shape of a cylinder with a hole along the z-axis. By applying inverted voltages to electrodes, the electric field between each two electrodes induces a bending of the crystal into the desired direction. To bend the cylinder in x- and y-direction or to induce a length expansion or contraction in z-direction, in total five electrodes are needed. One inner electrode is responsible for the movement in z-direction, while each two electrodes on opposite sides of the outer cylinder surface account for bending in x- and y-direction.

Mostly ceramics with perovskite ABX_3 structures like lead titanate $PbTiO_3$ are used for piezos. The piezos have a dipole moment below a certain Curie temperature T_C in a tetragonal structure. Above the Curie temperature a phase transition to a cubic structure occurs. The dipole moment of the tetragonal structure is necessary for a permanent polarization and the piezoelectric effect.

To induce a permanent large dipole of the whole crystal, one has to increase the temperature of the crystal just below T_C and apply a strong electric field to align all Weiß domains for maximum total polarization. After cooling down the piezo, the Weiß domains stay aligned and the dipole moment persists. Note figure 3.4 for a schematic overview of the piezoelectric effect:

Applying a force along the z-axis of $PbTiO_3$ leads to a displacement of the ions which changes the dipole moment $\vec{p}$ (direct piezoelectric effect $\vec{F} \rightarrow V$). Applying an electric field along the z-axis the displacement of the ions causes a permanent change
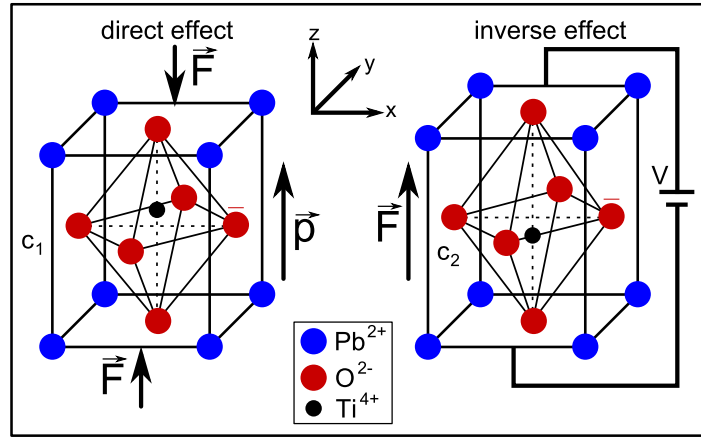
Figure 3.4: Schematic overview of the direct and inverse piezoelectric effect: applying a force along the z-axis leads to a displacement of the Pb^{2+} and Ti^{4+} cations with respect to the O^{2-} anions. This changes the dipole moment $\vec{p}$ and induces surface charges (direct effect $\vec{F} \to V$), while by applying an electric field along the z-axis the displacement of the ions causes a change in the lattice parameter c and therefore induces a force $\vec{F}$ (inverse effect $V \to \vec{F}$).

in the structure parameter c and therefore induces a force $\vec{F}$ (inverse piezoelectric effect $V \to \vec{F}$).

Practical realization of nano positioning is done via voltage signal amplification of a digital-analog converter. Typical values for movements of piezo ceramics are in the order of $\approx 2\,\mu$m. To induce that movement, voltages of $300\,$V have to be applied to the piezo electrodes. With a resolution of $16\,$bit of the digital-analogue converter the piezo movement can be controlled in steps of $0.05\,$nm (this equals voltage changes after amplification of $5\,$mV), which is sufficient to have a precise nano positioning for STM measurements.

Beetle-Type STM Unit

A basic STM unit capable of an automatic approach consists of at least a tip mounted on a piezo ceramic for scanning and a second piezo for coarse approach of the piezo containing the tip. The tip can be carefully moved towards (approached to) the sample until a tunneling current flows. To have a reliable coarse approach system, more elaborate systems have to be utilized. In our setup a beetle-type STM was used following the conceptual design of Besocke [13] and is based on the stick-slip approach system, which can be seen as an interplay between static and dynamic friction. For a schematic overview of the piezo and sample arrangement see figure 3.5.

The sample holder serves as the inertial mass, while the outer piezo ceramics with tungsten balls mounted on top are in contact with the inertial mass and can be oscillated forth and back. A so called stick-slip motion system is used to oscillate the balls and to move the inertial mass by an absolute value. During a fast gliding movement of the tungsten balls the inertial mass stands still, while the balls change their position relative to the inertial mass. The next slow movement moves both
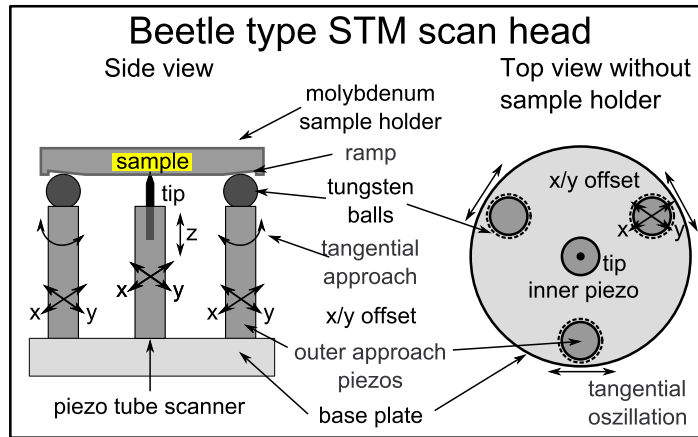
Figure 3.5: Schematic side and top view of the beetle-type STM setup: Three outer piezos are used for the stick-slip motion of the sample holder and are arranged on a base plate. The inner piezo is centered on the base plate and carries the tungsten tip, while tungsten balls are mounted on top of the outer piezos.

masses back to the original position of the balls because of friction induced forces. After the two movements the inertial mass changed its position by an absolute value, while the second oscillating mass resides on the original position. By adding up several oscillating movements, the inertial mass can be moved relative to the balls into certain directions. If one assumes a flat surface of the inertial mass, the stick-slip motion can move the inertial mass in lateral directions only. But if one assumes a built-in slope by three helical ramps of the inertial mass, the stick-slip oscillatory movement of the balls can move the inertial mass along the ramp downwards and upwards changing the height of the sample with respect to the tip. This principle is used in the beetle-type STM to approach and retract the sample holder relative to the tip.

The sampleholder containing the sample crystals has three helical ramps with a slope in z-direction following the round edge of the cylindrical shape. In the beetle-type STM setup the gravitational force acts upon the sample holder facilitating friction between the inertial mass and the three tungsten balls. These balls are mounted on three equally spaced outer piezo ceramic tubes (see top view in figure 3.5). The movements of the outer piezos are effective in directions tangential to the sample holder. The first gliding movement slides the tungsten balls along the ramp of the sample holder. The second slow tangential movement back to the original position turns the sample holder to a new position with lowered tip-sample distances. Tungsten balls are used, because they provide a low coefficient for dynamic friction and a sticking of the sample holder to the balls during the slow movement.

This stick-slip motion can be combined to a total approach of the sample relative to the tip. This coarse approach principle was first introduced by Frohn [49]. The whole approach can be divided into two repeating stages:

- At first the center piezo tube with the tip expands fully trying to obtain tunneling current with the sample surface. Therefore a voltage is applied to
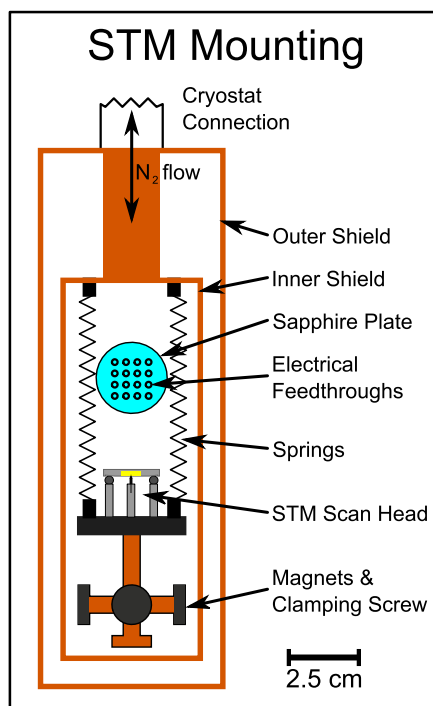
Figure 3.6: Schematic overview of the STM housing: the STM piezo scan head is suspended on three springs and can be clamped to the inner shield for transport and heat flow during cooling down for low temperature measurements. The whole system is electrically connected via feedthroughs inserted in a sapphire plate and thermally shielded by gold coated copper plates surrounding the whole STM system. On the bottom of the pendulum magnets inhibit vibrations through Eddy current damping.

the tip and the tunneling current is measured. If the current exceeds a certain value, the tip can be assumed to be in contact and the approach is terminated. If no current is detected, the inner piezo fully retracts to enable a safe (that means without crashing the tungsten tip) coarse approach movement.

- Therefore the previously described stick-slip motion is performed, where the fast tangential motion of the outer piezos let the tungsten balls slip along the ramp. The slower movement of the balls back into their initial position turns the sample holder, lowers the tip-sample distance and prepares the piezo for another fast movement. Up to 15 steps are carried out thereby decreasing the tip-sample distance by about a micrometer.

This two stages are repeated in a loop until a tunneling current is measured.

STM Mounting

The beetle-type STM scan head was mounted and connected inside a metal housing designed by Stipe et al. [144]. The STM is suspended on three springs from vibrations and is thermally and electronically protected by two gold coated copper heat shields surrounding the STM scan head (see figure 3.6 for details).

STM Operation

In order to keep the tip-sample distance constant, a fast and reliable feedback loop is required. Therefore the actual tunneling current as a function of molecule topology and local density of states is measured and compared with a specific value (the setpoint).

Deviations of the tunneling current from the setpoint are processed in a feedback controller to keep the tip-sample distance and thus the current constant. A precalculated voltage (feedback response) is then applied which expands or retracts the piezo tube for z-movement of the tip. Continuous feedback controlling of the tunneling current is used to maintain a constant tip-sample distance during lateral scanning in x- and y-direction.

If the lateral scanning is slow and the feedback controller has enough time to respond to changes in the sample topology, the current can be hold constant (constant current mode). During fast scanning the tip is held at a constant height, and during lateral scanning according to the topology the current deviates (constant height mode). All topology information is then kept in the current image, while in constant current mode all topology information is kept in the topography image.

The continuous feedback loop uses a proportional and integral (PI) controller in order to process the actual information and to calculate the response of the tip. By changing the values for the proportional and integral part, the setpoint and the tunneling voltage, the feedback loop can be adjusted to the topology of the sample and to scanning conditions [151, 64].

For all UHV STM experiments a RHK Technology Model SPM 100$^{\copyright}$ PI controller and the corresponding XPMPro 2.0.1.6 software was used. Image processing was performed with the free SPM data analysis software *Gwyddion 2.30* [103]. STM images were processed with plane leveling unless stated otherwise.

Vacuum Metal Chamber

The whole system is installed in an ultra-high vacuum chamber with facilities for sample and tip preparation by sputtering and annealing. The chamber is mounted on a vibration controlled optical table in order to decouple the system from external vibrations. For detailed images of the whole setup see figure 3.7.

3.1.3 Tip and Sample Preparation

STM tips were prepared in a two-step process. First they were treated by electrochemical alternating current etching of a polycrystalline tungsten wire (diameter 0.5 mm) in aqueous 2 M KOH solution at currents around 20 mA. In a second step, these tips were sharpened by electropolishing under optical control in a light microscope [164]. The beetle-type setup of the STM made it necessary to cut the polished tips to a certain length of 9.50 mm (with a narrow tolerance of 50 μm) under optical control. For sample preparation of the crystals, cycles of sputtering and subsequent annealing were applied (HOPG was annealed only). Typical sputtering parameters for the
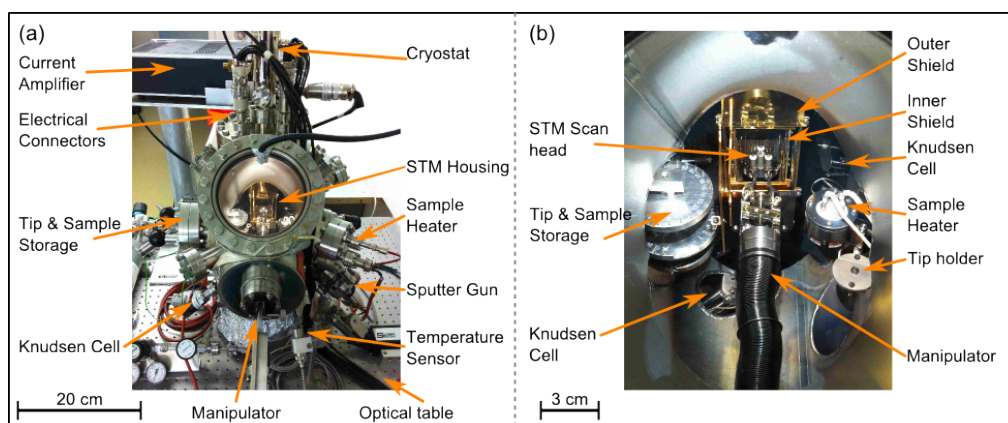
Figure 3.7: Photographs of the experimental setup: An UHV metal chamber is mounted on a vibration controlled optical table. (a) A manipulator allows inserting the tip and sample from storage into the STM scan head as well as into the heater. (b) Detailed view of the tip and sample storage and preparation facilities. The STM scan head can also be seen.

metal crystals like Ag(111), Au(111) and Cu(111) are a neon ion current of $10\,\mu A$ with energies between $0.5 - 1\,keV$ for 5 minutes. Afterwards all samples were annealed at temperatures of $773\,K$ (Au(111)) or $823\,K$ (Ag(111) and Cu(111)). To prevent contamination of the crystal surface, the crystals were heated from the back side by an electron beam with energies of $1\,keV$ and currents of $5\,mA$. The temperature was monitored by an infrared pyrometer pointing directly onto the crystal surface.

3.2 Ultra-High Vacuum

3.2.1 Background

In order to minimize influences and adverse effects from interactions of molecules from the environment with the sample, one has to conduct experiments in ultra-high vacuum (UHV). UHV is defined as a base pressure below $1 \times 10^{-8}\,mbar$. Typical pressures in an UHV chamber are below $3 \times 10^{-10}\,mbar$. To estimate the interaction of the remaining particles in an UHV chamber with the substrate, one can utilize the surface science unit *Langmuir*. One Langmuir has the dimension pressure times time and is defined as $1\,L = 1.33 \times 10^{-6}\,mbar\,s$. Under the assumption of a sticking coefficient of $100\,\%$, one gets one monolayer of adsorbed gas molecules on the sample at a pressure of $1.33 \times 10^{-6}\,mbar$ in $1\,s$ [99]. Accordingly, the impact probability of the remaining gas atoms on a substrate at a base pressure of $1.33 \times 10^{-10}\,mbar$ is 1×10^{-4} monolayers per second. So in one hour each atom or molecule of the sample surface is approximately hit once by a gas atom. Normally, sticking coefficient of remaining gas atoms are less than $100\,\%$, so this base pressure is sufficient to exclude contamination effects over a reasonable amount of time.
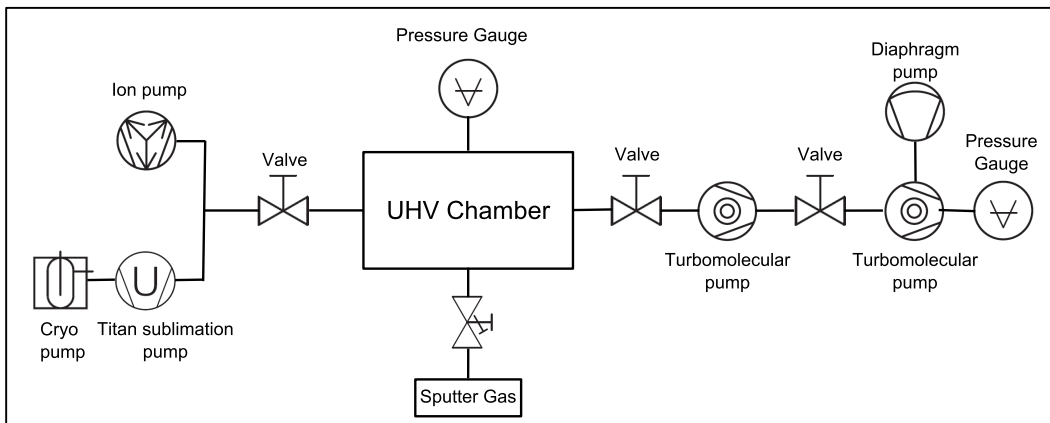
Figure 3.8: Vacuum scheme of the UHV chamber

3.2.2 UHV Chamber

All experiments were carried out in an UHV chamber. It is necessary to use a combination of different vacuum pumps to achieve UHV. The vacuum scheme is shown in figure 3.8. For the fore-vacuum of the turbomolecular pump a small unit consisting of a diaphragm and a small turbomolecular pump is used. This setup can pump down the whole chamber to a base pressure below 1×10^{-10} mbar, but in order to eliminate unwanted vibrations of the turbo pumps during STM measurements, an ion pump is used to maintain UHV in the chamber while the turbomolecular pumps are turned off. A titan sublimation pump mounted inside a cryo shroud can be used additionally to enhance pump rates.

Chapter 4

Realization of different Concepts towards the Synthesis of Two-dimensional Polymers

This chapter contains experimental and calculational results and interpretation of the data. The presentation follows possible reaction pathways of the synthesis of two-dimensional polymers. Each section focuses on one specific set of parameters that are important for the understanding of the reaction mechanism towards the synthesis of 2D polymers. In section 4.1 the influence of bond topology and chemical reaction mechanism is examined, while in section 4.2 the influence of monomer size and remaining functional groups on bottom-up on-surface reactions is presented. This concept is extended with a model for the branched growth of one-dimensional polymers in section 4.3. In order to study the influence of pendant groups, the surface chemistry of two molecules, one hydrogenated and one fluorinated, is compared in section 4.4. The experimental work is concluded with an *en route* dehalogenation method induced by a heatable drift tube in section 4.5. In the last section 4.6 a new class of fully conjugated 2D polymers with excellent electronic properties is proposed and underlined by theoretical calculations.

4.1 Synthesis of Two-Dimensional Phenylene–Boroxine Networks through in vacuo Condensation and On-Surface Radical Addition

Schlögl, Stefan ; Sirtl, Thomas ; Eichhorn, Johanna ; Heckl, Wolfgang M. ; Lackinger, Markus. Synthesis of two-dimensional phenylene-boroxine networks through in vacuo condensation and on-surface radical addition. *Chem.Commun.* **47** (2011), 12355-12357. http://dx.doi.org/10.1039/C1CC13896K. - Reproduced by permission of The Royal Society of Chemistry.

4.1.1 Abstract

We report on covalent two-dimensional phenylene–boroxine hybrid-networks that were synthesized under ultra-high vacuum conditions from doubly functionalized monomers through thermally activated condensation prior to deposition and successive heterogeneously catalyzed radical addition on Ag(111). Structural properties were characterized in situ by high resolution Scanning-Tunneling-Microscopy (STM).

4.1.2 Introduction

The synthesis of covalent two-dimensional organic materials is a challenging but promising goal in material science. Single layer graphene is the most abundant and best studied 2D organic material [50]. The inherent absence of an electronic band-gap gives rise to intriguing physics, yet, other envisaged applications require a band-gap that needs to be introduced by dopant side groups [161]. While graphene can meanwhile routinely be prepared by exfoliation of graphite or graphite oxide [133], a bottom-up synthetic approach through polymerization of organic monomers offers structural and chemical versatility [54, 117, 128]. On-surface synthesis of 2D covalent networks was accomplished through various types of polymerization reactions [54], predominantly condensation [132, 158, 167] and radical addition of halogenated precursors [14, 55, 59]. Herein we demonstrate the synthesis of covalent hybrid-networks comprised of both phenyl and boroxine rings arranged on a hexagonal lattice. Boroxine rings (B_3O_3) are hexagonal, planar, and similar in size to phenyl rings [34]. In this respect it is interesting to study their interchangeability in covalent networks and the impact on structural properties [44, 111]. Substitution of phenyl with boroxine rings is also known to modify material properties, e.g. renders polymeric materials flame retardant [76, 101].

4.1.3 Experimental Methods and Materials

All experiments were conducted with the home-built beetle type Scanning-Tunneling-Microscope at room temperature under ultra-high vacuum (UHV) conditions with a base pressure below 1×10^{-10} mbar (see section 3.1.2 for details). Lattice parameters and intermolecular distances were derived from STM topographs with an accuracy of

5% after calibration with atomically resolved topographs of highly oriented pyrolytic graphite(001) (HOPG) and Ag(111) surfaces. Figure 4.2 was processed by a Gaussian 2×2 filter and correlation averaging. Single crystal Ag(111) surfaces were prepared by cycles of Ne^+-ion-sputtering at 1 keV and electron-beam annealing at $550\,°C$ for 50 minutes (for details see section 3.1.3). The HOPG sample was cleaned by electron beam annealing up to $500\,°C$ for 45 minutes . The cleanliness of the substrates was verified by STM imaging prior to deposition. All STM images were recorded using a RHK electronics and XPM Pro 2.0.1.3 software.

The monomer 3,5-dibromophenylboronic acid (DBPBA) (CAS $117695-55-3$, purity not specified) with the chemical formula $Br_2C_6H_3B(OH)_2$ and a molecular weight of 279.72 amu was obtained from Sigma Aldrich Germany. DBPBA was introduced into a home-built Knudsen cell and heated up to $190\,°C$ for at least 1 h. During all deposition procedures the substrates were held at room temperature. The DBPBA sublimation temperature of $190\,°C$ was determined by means of a Quartz Crystal Microbalance.

4.1.4   Results and Discussion

Synthesis of the proposed covalent hybrid-networks is based on 3,5-dibromophenylboronic acid (DBPBA). First, heating of DBPBA thermally activates condensation which yields less reactive TDBPB monomers that are then deposited onto Ag(111). Subsequent thermal annealing initiates the on-surface polymerization via radical addition (see figure 4.1 for a reaction scheme).

To this end, the aromatic DBPBA monomer is doubly functionalized with two different functional groups: one boronic acid group for condensation and two bromine substituents for surface-mediated radical addition. On Ag(111) radical addition of brominated precursor molecules is kinetically suppressed at room temperature and thermal annealing is required to initiate the polymerization through homolysis of the bromine substituents [59]. On the other hand, the condensation of boronic acids can be thermally activated in vacuo without the need for a catalyst [158]. In the proposed reaction scheme, the cyclo-condensation of DBPBA molecules into TDBPB is the last synthesis step prior to deposition and carried out in vacuo by a mere thermal treatment at $190\,°C$. Boronic acids preferably react into boroxine rings through cyclo-condensation of three entities, whereby three H_2O molecules are released. Because DBPBA is only monofunctionalized for condensation, the reaction does not yield interconnected networks as for diboronic acids [34], but larger 1,3,5-tris(3',5'-dibromophenyl)-boroxine molecules (TDBPB, see figure 4.1(b)). This "in-crucible synthesis" is feasible, because cyclo-condensation of the boronic acid functionality is preferred over sublimation, whereby thermal sublimation of the free boronic acid DBPBA is essentially not possible. Instead a relatively high experimentally determined sublimation temperature of $190\,°C$ indicates thermal sublimation of the larger threefold-symmetric TDBPB monomer that already features both phenyl and boroxine rings. Since bromine functionalities are not known to react at these relatively low temperatures without the presence of a catalyst, further polymerization
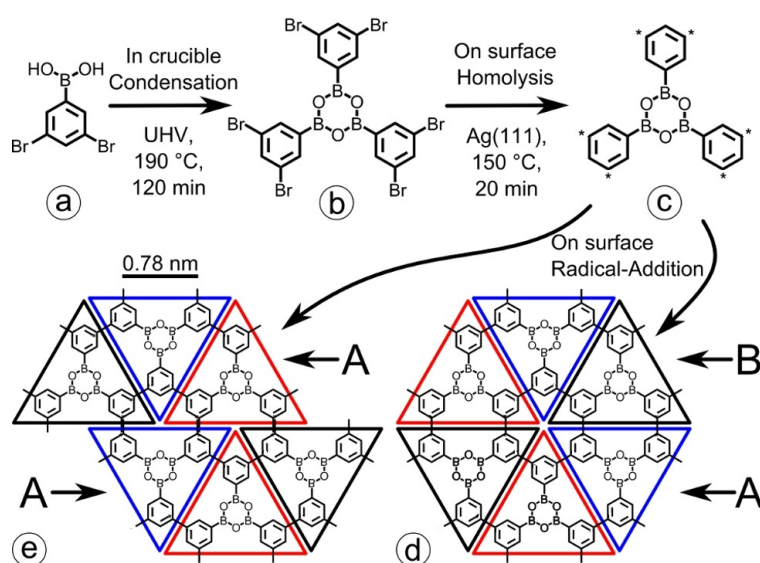
Figure 4.1: Reaction scheme for synthesis of covalent phenylene-boroxine hybrid-networks from 3,5-dibromophenylboronic acid (DBPBA) monomers. First thermally activated condensation of (a) DBPBA in the crucible of a Knudsen cell results in (b) 1,3,5-tris(3',5'-dibromophenyl)-boroxine (TDBPB). Deposition of TDBPB on Ag(111) and further thermal activation yield (c) surface-stabilized triphenylene-boroxine hexaradicals (TPBHR) that subsequently polymerize into covalent phenylene–boroxine networks through radical addition. Hereby the bromine substitution pattern of TDBPB allows for two different stackings: (d) ABAB and (e) AA.

reactions in the crucible are not expected, but thermal sublimation of intact molecules. The thermal "in-crucible synthesis" of TDBPB was verified by comparative Raman spectroscopy and NMR of the initial and thermally treated DBPBA compound (see sections 4.1.5 and 4.1.6 for spectra and details). In additional experiments a DBPBA filled crucible was used to deposit organic molecules onto graphite(001) as well as onto Ag(111), with both substrates held at room temperature. These experiments further substantiate the thermally activated condensation of DBPBA into TDBPB and its subsequent deposition. On inert graphite(001) substrates well-ordered self-assembled trigonal monolayers with a lattice parameter of (1.50 ± 0.10) nm were observed.

In the STM topograph shown in figure 4.2(a) threefold symmetric molecular entities can be identified, whose size and symmetry are consistent with intact TDBPB molecules. Moreover, six peripheral protruding spherical features can be discerned and are assigned to the bromine substituents of intact TDBPB. In the proposed structural model, cyclic halogen-halogen-halogen bonds between three bromine substituents with experimental bromine-bromine distances of (0.45 ± 0.10) nm stabilize the self-assembled monolayer (figure 4.2(b)). Halogen bonds are attractive anisotropic electrostatic interactions between Cl, Br, or I substituents that originate from a non-spherical charge distribution at the halogen with a negative ring and a positive end cap [20, 121]. Trigonal cyclic arrangements optimize electrostatic interactions and were similarly found in both 3D and 2D structures [20, 156]. Experimental Br-Br distances here are larger than those found in bulk crystals (0.36 nm) and hint
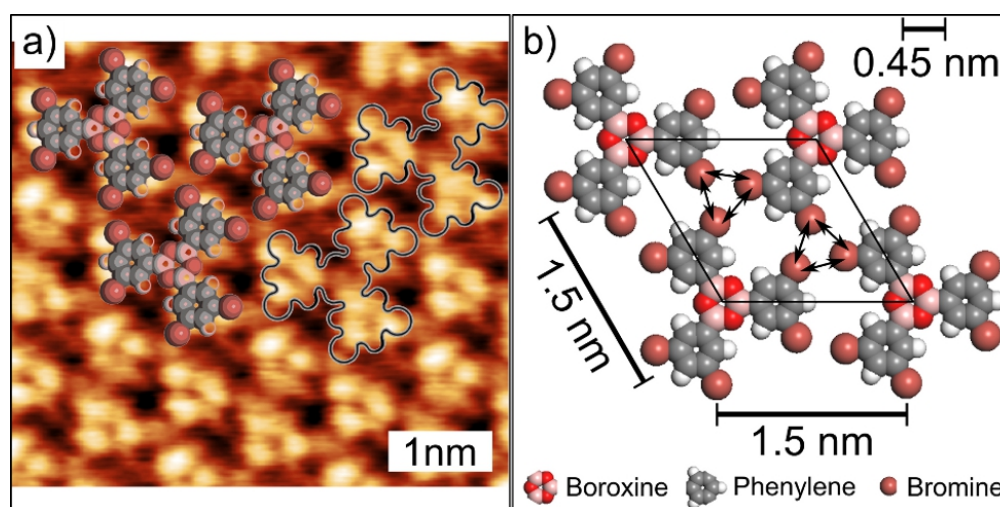
Figure 4.2: Self-assembled TDPBP monolayer on graphite(001). (a) STM topograph (+0.60 V, 40 pA, correlation-averaged); as evident from the scaled overlay, size and symmetry of the molecular entities are consistent with threefold-symmetric TDBPB molecules and six peripheral bromines of one molecule are highlighted by black arrows. (b) Tentative model of the TDBPB monolayer, where molecules interact through cyclic halogen-halogen-halogen bonds (indicated by black arrows).

towards a surface influence. STM measurements of TDBPB deposited onto Ag(111) reveal a less well ordered arrangement of threefold symmetric molecules (figure 4.8 in section 4.1.8). Again, size and symmetry of the molecules and the discernible bromine substituents suggest deposition of TDBPB rather than the precursor material DBPBA. Albeit some monomers are already interconnected and some contrast features point toward deposition of a low fraction of unreacted DBPBA monomers, the great majority of TDBPB molecules remains intact upon deposition onto Ag(111) held at room temperature and the bromine substituents are not cleaved off. Although the intermolecular arrangements exhibit only short-range order, molecular aggregates are likewise stabilized by halogen-bonds similar to the monolayers on graphite. LEED measurements of similarly prepared samples show a hexagonal pattern of rather broad reflections. The LEED pattern is consistent with two orientational domains of $\left(2\sqrt{7} \times 2\sqrt{7}\right) R \pm 19°$ that corresponds to a lattice parameter of $a = 1.53$ nm (see figure 4.7 in section 4.1.7 for details). Yet, the diffraction pattern most likely does not arise from long-range ordered monolayers, but from short range order, where TDBPB dimers adopt a preferred intermolecular distance of 1.50 nm and a preferred orientation with respect to the substrate. The LEED lattice parameter is consistent with the nearest-neighbor distance in STM measurements of less-well ordered samples. Although in the STM experiments, the deposition rate was varied from $(0.02 – 0.1)$ monolayers per minute, no long-range ordered monolayers were obtained on Ag(111), maybe because of DBPBA impurities and first covalent interlinking reactions. Because of its bromine substitution pattern and its planar structure, TDBPB is a well suited monomer for the synthesis of hexagonal phenylene–boroxine hybrid-networks through surface-mediated polymerization. While annealing of TDBPB monolayers up to
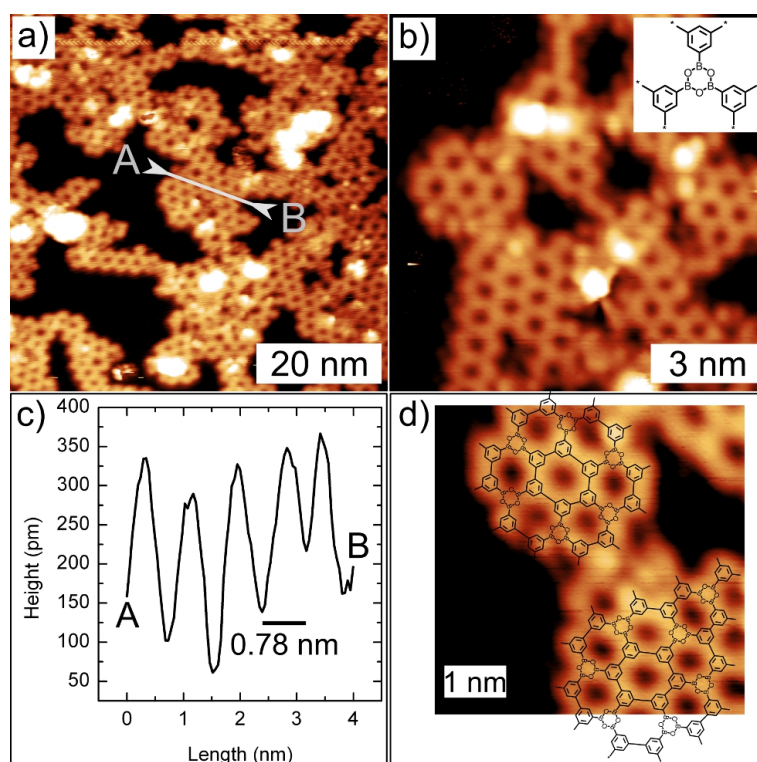
Figure 4.3: (a) Overview and (b) close-up STM topographs (+0.70 V, 50 pA) of annealed TDPBP monolayers on Ag(111). Thermally activated dehalogenation and radical addition yield covalent networks. (c) Line-profile along A–B in image (a); it indicates a lattice parameter, i.e. interpore distance, of (0.78 ± 0.10) nm (d) Close-up of covalent networks with molecular overlay. The aggregate is formed by exclusive AB stacking.

200 °C for 10 min on graphite(001) only leads to thermally induced desorption, annealing on Ag(111) (10 min at 130 °C) activates the dehalogenation reaction aided by the catalytic properties of the surface [14, 59, 19], whereby triphenylene–boroxine hexaradicals (TPBHR) are generated (figure 4.1(c)). Subsequently, these radicals polymerize through radical addition into covalent networks directly on the surface (figure 4.3(a) and (b)).

As illustrated in the reaction scheme the polymerization of hexaradicals can proceed in two different stereochemical arrangements (figure 4.1(d) and (e)). Two adjacent monomers can interlink via two covalent intermolecular bonds. Since the monomers possess a triangular footprint this means they adjoin at their bases. Exclusive formation of these two-fold covalent interconnects would result in a periodic covalent network with ABAB stacking and *P6mm* symmetry as depicted in figure 4.1(d). However, radical addition is also possible in a way that one monomer forms two covalent bonds with two different monomers on one side of its triangular footprint. Continuation of this binding motif into extended two dimensional networks yields AA stacking (figure 4.1(e)), where the tips of the triangles are aligned with the center of the baseline in the row above. The resulting periodic network would still exhibit a hexagonal arrangement of boroxine and phenyl rings, but would possess considerably

lower symmetry (*P2mg*). In the experiment random stacking is expected, since the polymerization cannot be controlled, and consequently a less regular distribution of boroxine rings within the hexagonal network. Polymerization, i.e. the formation of covalent networks upon thermal treatment is unambiguously verified by comparison of precise experimental STM derived structure parameters with theoretical values. The line-profile in figure 4.3(c) indicates a spacing between adjacent six-membered rings of (0.78 ± 0.10) nm. This value is in perfect agreement with the (0.78 ± 0.10) nm as obtained from geometry optimized DFT calculations of the *P6mm* structure (cf. 4.1.9). The DFT calculations also yield an approximative value of 2.8 eV for the HOMO–LUMO energy gap. The electronic states do not exhibit a significant dispersion in k-space. This means that electrons are localized with low mobility and almost infinite effective mass. Similar hexagonal networks that only consist of phenylene rings show a less flat dispersion relation. Comparison of those structurally similar networks denotes effective electronic decoupling through boroxine rings [3] (details can be found in 4.1.9). The covalent phenylene–boroxine networks do not exhibit long-range order. Yet, in covalent networks that were synthesized from structurally much simpler tritopic monomers as for instance tribromophenylbenzene [59, 19] non-ideal strained covalent rings composed of more or less than six monomers occur with densities comparable to those of ideal rings. In polymerized TDBPB networks strained rings are only observed occasionally (cf. 4.1.8). Apparently, their formation becomes less likely due to the complex bond topology of the six-fold bromine-substituted monomer. Although the polymerized TDBPB networks exhibit mostly regular rings, the resulting domain size is comparatively small. Different azimuthal orientations to the substrate impair coherent interconnection into long-range ordered networks. In contrast to covalent networks from simple tritopic monomers, now vacancies can be observed (see figure 4.10 in section 4.1.8). Around these vacancies, the hexagonal lattice is preserved and just one monomer is missing, leading to AA stacking.

4.1.5 Raman Spectra of DBPBA

Raman spectra (see figure 4.4) were acquired from both a powder sample of thermally treated DBPBA and also a thin film of vacuum sublimed material with a confocal Raman microscope (*alpha*300*R*, WITec GmbH, Ulm, Germany). All spectra were accumulated 10 times with an integration time of 1 s. An excitation laser power of 580 μW was used at a wavelength of $\lambda = 532$ nm. Using a 1800 mm^{-1} diffraction grating, the nominal resolution was 1.3 cm^{-1} per CCD-pixel. A $\times 100$ microscope objective with a numerical aperture of 0.9 was used to efficiently collect the scattered photons. Since in the confocal geometry the signal arises from a spatially restricted volume of the sample (~ 400 nm lateral, ~ 1 μm vertical), probed volumes of powder sample and thin film are comparable.
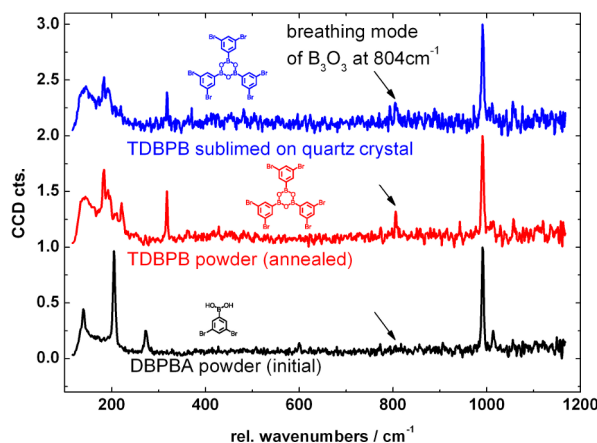
Figure 4.4: Raman spectra of untreated DBPBA (black), after thermal annealing at 190 °C for 120 minutes under vacuum conditions (red), and from a thin film deposited onto a quartz crystal microbalance located $\sim$ 5 mm above the aperture of the Knudsen cell (blue). Both thermally treated and deposited materials exhibit new modes at $\sim$317 cm^{-1} and $\sim$804 cm^{-1} that are not present in the untreated DBPBA material. Also the bands around $\sim$200 cm^{-1} are comparable for the thermally treated material and the thin film, but distinctly different from the unreacted starting material. The mode at $\sim$317 cm^{-1} cannot be assigned, but the weak mode at $\sim$804 cm^{-1} corresponds to the breathing mode of boroxine rings [53]. Its presence indicates the cyclocondensation of three DBPBA molecules into TDBPB.

4.1.6   Nuclear Magnetic Resonance (NMR) Data of Untreated and Thermally Treated DBPBA

Proton 1H-NMR spectra were acquired with a JEOL ECP-270 spectrometer at frequencies of 270 MHz and a sample temperature of 298 K. The molecules were dissolved in Methanol-D4 and no additional standard was used. The data was processed using the Delta 5.0.1 Software from JEOL and standard FFT settings. The proton peak of the free boronic acid group is observed for the initial DBPBA molecules (figure 4.5), but is absent in the NMR spectra of the thermally treated TDBPB molecules (figure 4.6) indicating thermally activated condensation. A comparison of the proton peaks for unreacted and treated molecules suggests a high yield of the thermally activated reaction.

4.1.7   LEED Measurements of DBPBA

LEED experiments were carried out in an additional UHV system at a base pressure of 1×10^{-10} mbar. A LEED optics from Omicron NanoTechnology GmbH and control electronics from SPECS Surface Nano Analysis GmbH was used. Ag(111) single crystal surfaces were prepared by subsequent Ar$^+$-ion-sputtering and electron-beam annealing up to 550 °C for $\sim$10 min. The thermal treatment of DBPBA and deposition parameters were similar to the STM experiments. LEED diffraction patterns were recorded with the sample at room temperature. LEED experiments after room temperature deposition show rather broad reflections arranged in two
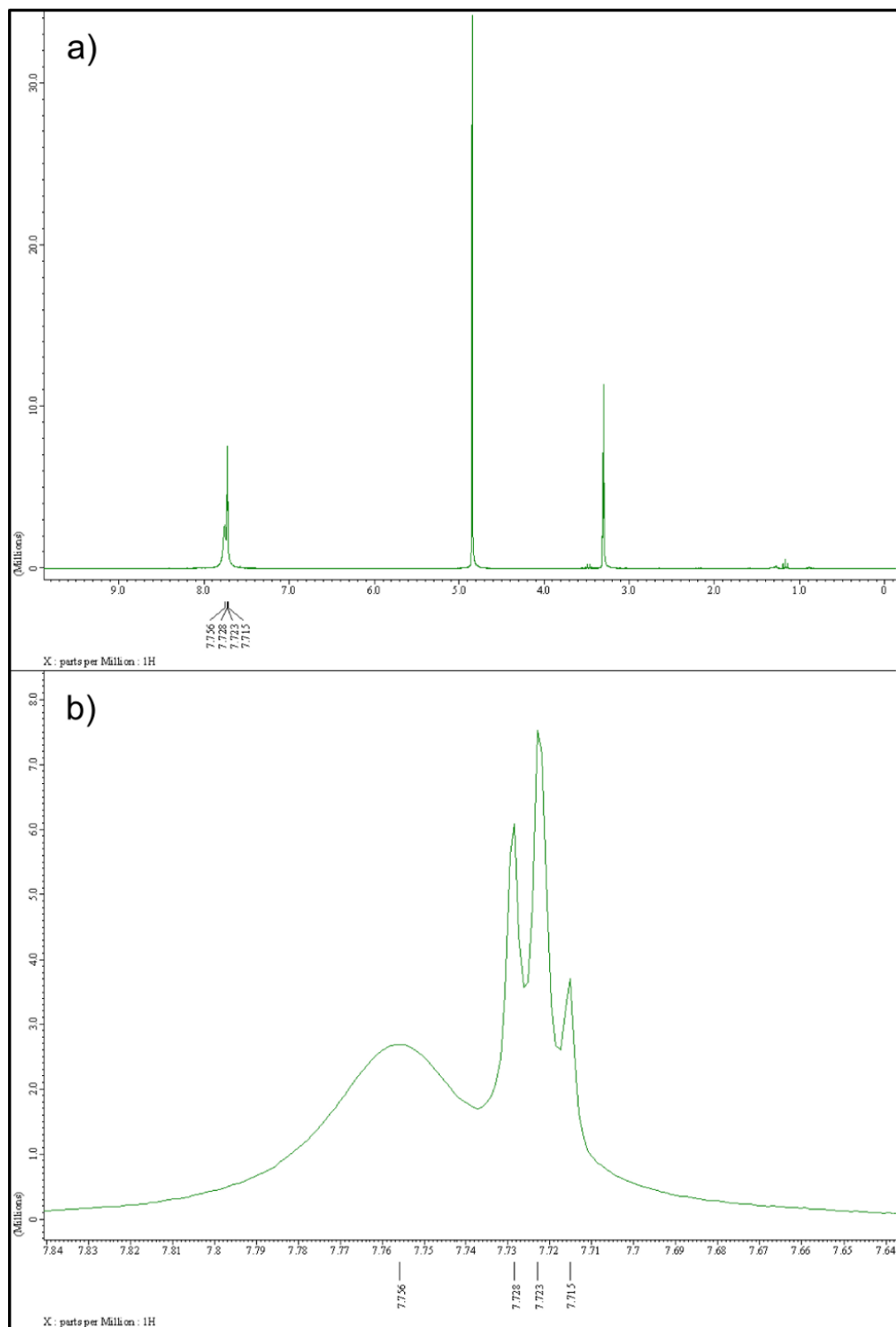
Figure 4.5: (a) NMR spectra of untreated DBPBA (^{1}H NMR, 270 MHz, CD$_4$O): δ_H 7.756 (OH), 7.728 (CH), 7.723 (CH), 7.715 (CH), 7.756 (OH). Small residues of undeuterated solvent molecules account for the peaks at 4.8 ppm and 3.3 ppm. (b) Close-up of (a). The broad peak centered at δ_H =7.756 (OH) can be assigned to the protons of the free boronic acid group, while the remaining multiplet originates from the aromatic protons.
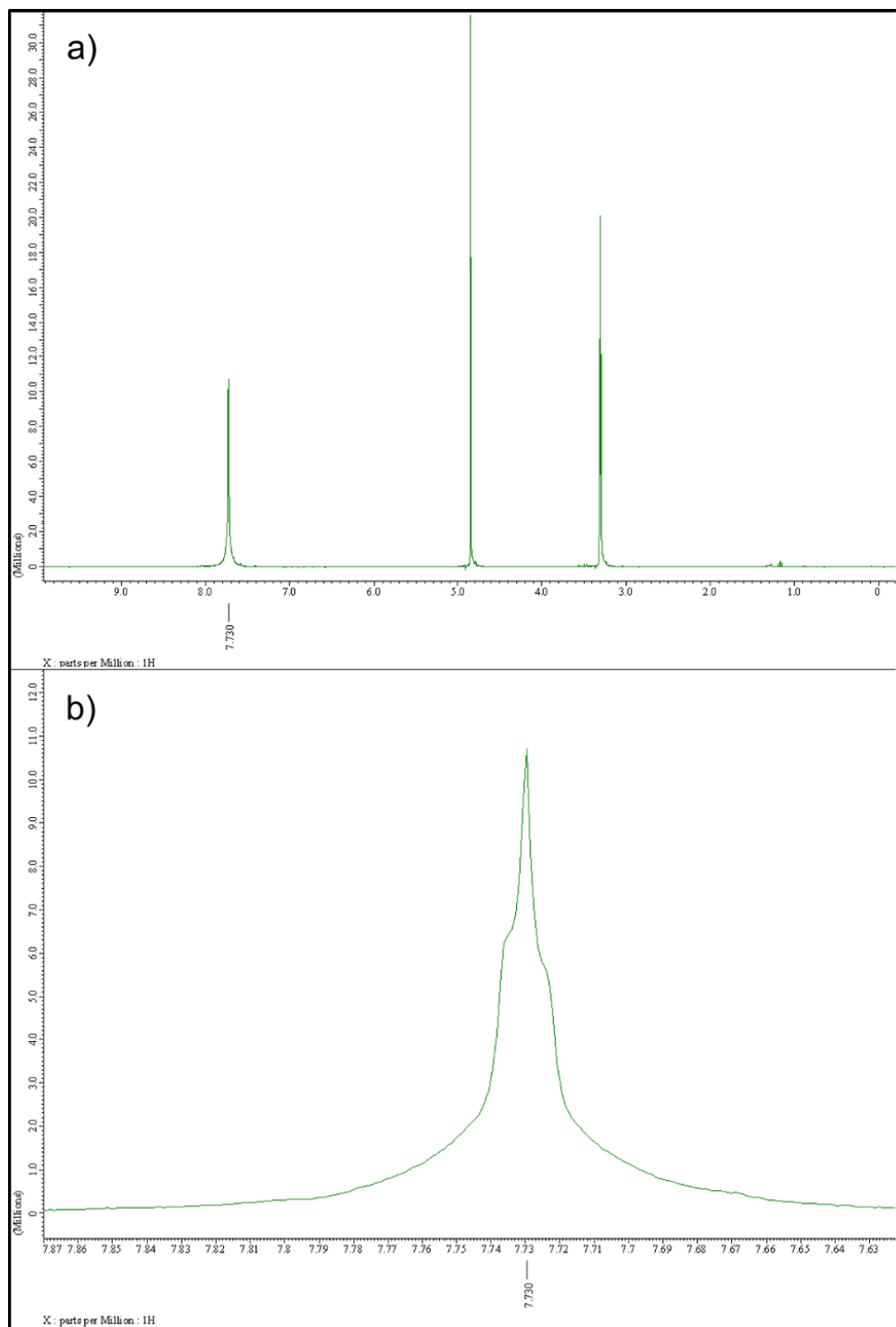
Figure 4.6: (a) NMR spectra of thermally treated DBPBA (190 °C, 120 minutes) (^{1}H NMR, 270 MHz, CD$_4$O): δ_H 7.730 (CH), 7.756 (OH)). Again, undeuterated solvent molecules account for the peaks at 4.8 ppm and 3.3 ppm. (b) Close-up of (a). The broad peak at δ_H =7.756 (OH) is absent after thermal treatment, indicating the condensation of DBPBA into TDBPB.
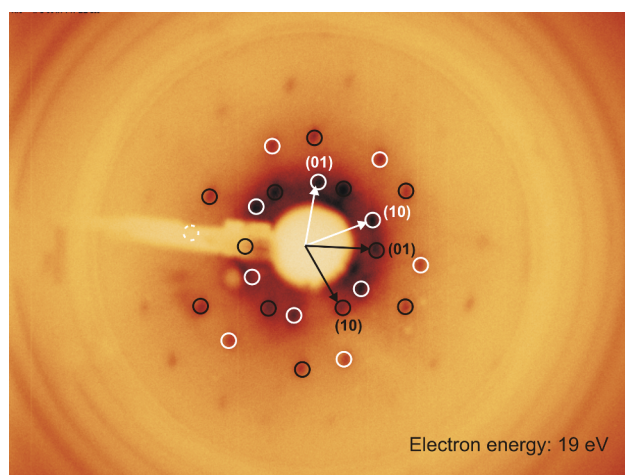
Figure 4.7: LEED diffraction pattern of an ordered TDBPB monolayer on Ag(111) acquired at an electron energy of 19.0 eV at room temperature. White and black circles in the inset assign the first and second order reflections to one of the two rotational domains. Numbers in parenthesis are the (hk) values of the respective reflections.

rotational domains of a hexagonal lattice. Within the experimental error, the results are consistent with a commensurate $\left(2\sqrt{7} \times 2\sqrt{7}\right) R \pm 19°$ structure that corresponds to a lattice parameter of $a = 1.53$ nm.

4.1.8 Additional STM topographs of DBPBA and Phenylene–Boroxine Networks

TDBPB deposited onto Ag(111) without further thermal treatment

Deposition onto Ag(111) leads to non-covalent less well ordered TDBPB arrangements. The outer shape of the adsorbates and the six bright peripheral protrusions indicate adsorption of intact molecules, i.e. homolysis of all molecules does not occur for room temperature deposition onto Ag(111) without further thermal activation. Yet, occasionally observed dimers may already be covalently interconnected, as suggested by their relative spacing (see red arrow in figure 4.8). Also low concentrations of smaller impurities can also be discerned in the STM topographs. Their size and less symmetric appearance suggest that those impurities may be unreacted DBPBA monomers (see green arrow in figure 4.8).

TDBPB deposited onto HOPG without further Thermal Treatment

A close-up STM topograph of TDBPB deposited onto HOPG shows submolecular features, where the three-fold symmetry and six peripheral features can clearly be discerned. The 2×2 unit cell image was processed by correlation averaging from an original 5×5 unit cell image using the software Image Metrology SPIP 5.1.2.
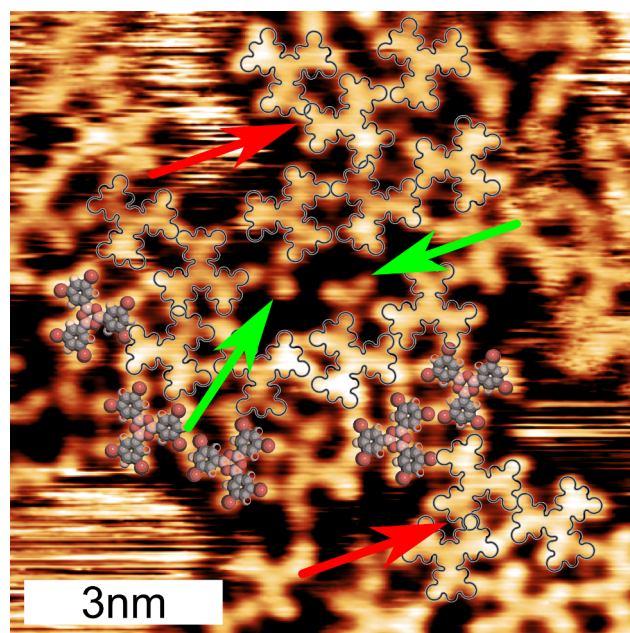
Figure 4.8: STM topograph of 1,3,5-tris(3,5-dibromophenyl)-boroxine TDBPB after deposition onto Ag(111) held at room temperature (+0.60 V, 60 pA). The apparent height of the molecules with respect to the substrate amounts to ∼100 pm.
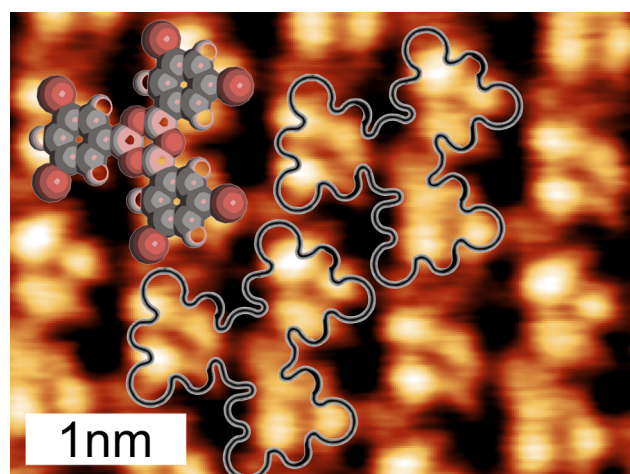

Figure 4.9: STM topograph of TDBPB deposited on HOPG showing the molecules in a hexagonal array with lattice constants of (1.5 ± 0.1) nm and submolecular resolution.
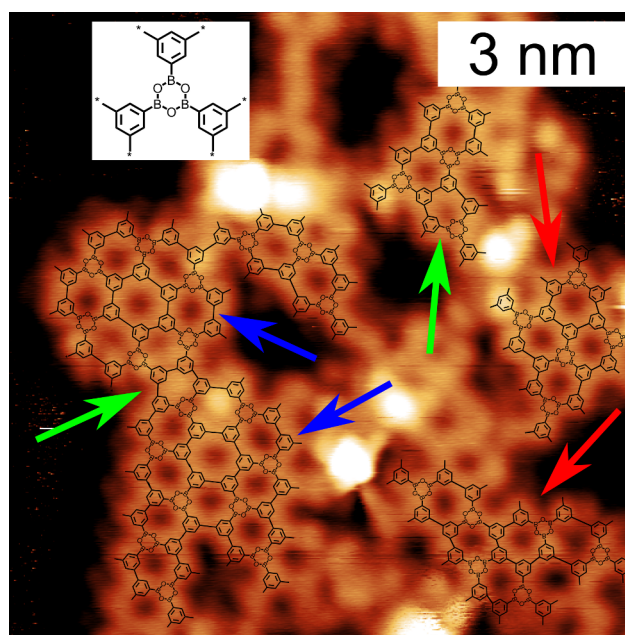
Figure 4.10: STM topograph of TDBPB deposited on HOPG showing the molecules in a hexagonal array with lattice constants of (1.5 ± 0.1) nm and submolecular resolution.

TDBPB deposited on Ag(111) after Thermal Treatment

Figure 4.10 provides additional features of the polymerized phenylene–boroxine network:

- The blue arrows indicate a closed circle consisting of six combined phenylene–boroxine rings arranged around a centered hexaphenylene ring and arises from exclusive AB-stacking.

- The red arrows mark examples for AA-stacking, which consist of rings with five phenylene and one boroxine.

- Only two out of shown 30 rings are five-membered rings occasionally observed as linkers between smaller covalent aggregates (denoted by green arrows).

4.1.9 DFT Calculations of Phenylene–Boroxine Networks

Lattice parameter and electronic structure of p6mm phenylene-boroxine networks

DFT simulations were conducted of regular phenylene-boroxine networks with *P6mm* symmetry that would result from exclusive ABAB stacking. The simulations employ a gradient corrected (GGA) functional PW91 [113] with plane wave basis set as implemented in the CASTEP code [137]. The substrate influence could be neglected, because for covalent networks molecule-molecule interactions are significantly stronger than molecule-substrate interactions. Total energies per unit cell were calculated as a function of lattice parameter for a hexagonal unit cell with periodic boundary
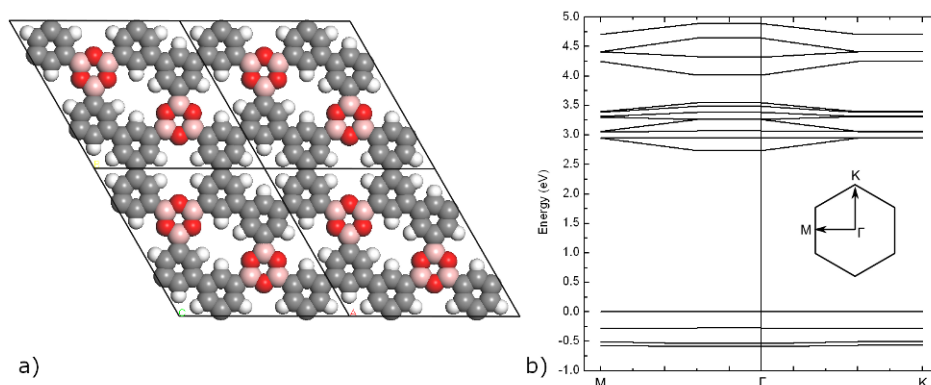
Figure 4.11: (a) Model of the covalent network with optimized lattice parameter: hexagonal lattice parameters $a = b = 1.55$ nm and periodic boundary conditions. (b) DFT CASTEP calculations of the electronic structure yield a HOMO–LUMO energy gap of 2.8 eV and the absence of dispersion in k-space.

conditions. The minimum total energy per unit cell was found for a lattice parameter of 1.55 nm (as shown in figure 4.11(a)). This lattice parameter of the *P6mm* unit cell corresponds to a distance of 0.775 nm between adjacent pores. The electronic structure (cf. figure 4.11(b)) of the *P6mm* network exhibits a HOMO–LUMO energy gap of ~2.8 eV and negligible dispersion in k-space, indicating localized immobile electrons. Yet, since DFT is known to underestimate band gaps [32], the actual HOMO–LUMO gap might be larger.

Structural Properties of a Single TDBPB Molecule

Thermal treatment of DBPBA results in cyclo-condensation of three molecules into 1,3,5-tris(3,5-dibromophenyl)-boroxine (TDBPB) molecules. An experimental proof of this hypothesis was accomplished by deposition of the product molecule onto unreactive substrates and subsequent STM imaging. In order to obtain precise theoretical dimensions of TDBPB molecules for overlaying them to the STM topographs, geometry optimized DFT calculations of isolated molecules were conducted using Gaussian03 with a B3LYP functional and a 6-31G* basis set applying standard convergence criteria [47]. The geometry optimized TDBPB molecule is essentially planar, although the substrate was neglected and no additional constraints were applied. The results are depicted in figure 4.12 and show that boroxine and phenyl rings in this compound are almost similar in size, with deviations below 1%.

4.1.10   Conclusion

In summary, we show that a covalent hybrid-network consisting of both phenyl and boroxine rings can be synthesized entirely in UHV from a comparatively simple monomer. The employed monomer was doubly functionalized with both boronic acid groups and bromine substituents for condensation and radical addition reactions, respectively. Two main conclusions can be derived: At first, vacuum sublimation of
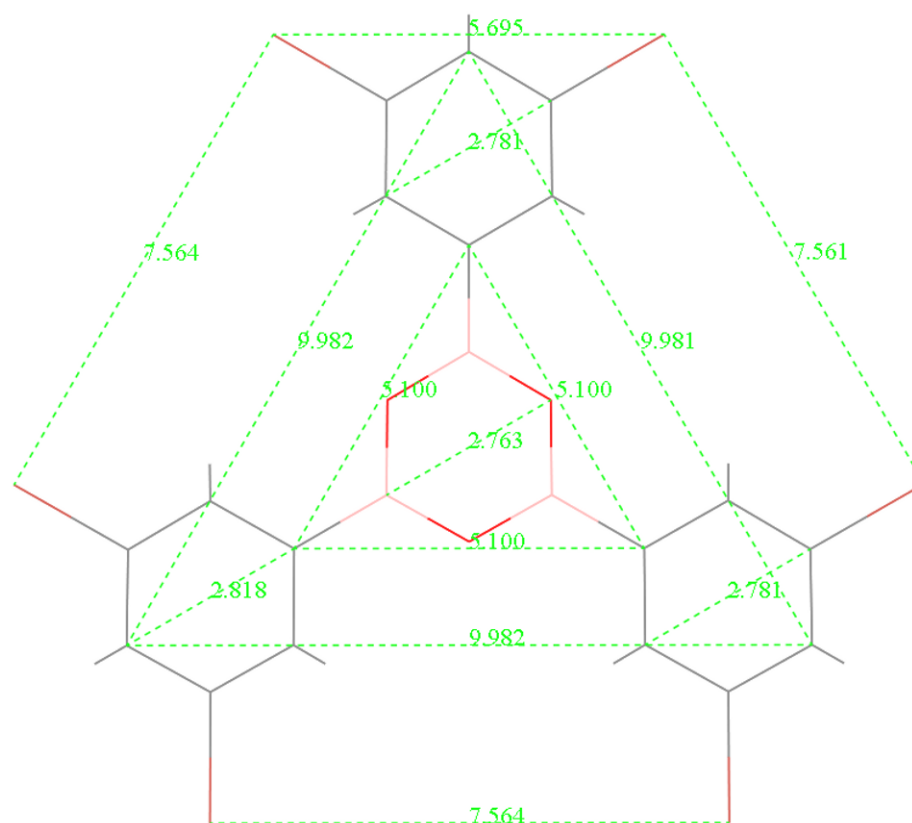
Figure 4.12: DFT geometry optimized structure of TDBPB molecules in the gas phase. All distances are given in Å and indicate nearly equal diameters of ∼2.8Å for phenyl and boroxine rings, respectively. Based on these calculations, we anticipate that size differences between boroxine and phenyl rings are indistinguishable in STM measurements.

even comparatively small boronic acids is not possible, because increasing the crucible temperature up to the sublimation point already thermally activates selfcondensation. Then again, the preferred and reliable selfcondensation of boronic acids into boroxine rings can also serve as a design principle for carrying out the last synthesis step in the crucible of the Knudsen cell and deposit more complex monomers from abundantly available, structurally simpler precursor molecules. Secondly, a more complex bond topology consisting of six functional groups leads to less network defects and is a key element in polymerizing long range ordered regular networks with predefined properties.

4.2 On-Surface Radical Addition of Triply Iodinated Monomers on Au(111) – the Influence of Monomer Size and Thermal Post-Processing

4.2.1 Abstract

In the present study on-surface polymerization of aromatic iodinated precursor molecules through radical addition is studied by scanning tunneling microscopy (STM) on Au(111) under ultra-high vacuum (UHV) conditions. Comparison of the two analogous monomers s-triiodobenzene and s-triiodophenylbenzene with similar symmetry and functionalization but differently sized organic backbones aimed to study the influence of monomer size on the morphology of resulting covalent networks. In contrast to previous studies on brominated monomers, here the reaction by-product, i.e., the split-off iodine atoms, was found to adsorb stably on Au(111) in ordered structures. The influence of post-processing by thermal annealing on both the covalent networks and the iodine structures was studied for different temperatures. DFT calculations were applied to evaluate formation energies of commonly observed topological defects and related to their experimental probability of occurrence.

4.2.2 Introduction

The synthesis of regular 2D polymers and covalent organic frameworks (COF) has revealed itself as a challenging goal of material science [128], yet with interesting and rewarding perspectives [54, 117]. The prospect of unprecedented chemical, mechanical, and thermal stability, promising electronic and optical properties, in combination with chemical tunability, has triggered worldwide efforts. For the synthesis of surface supported COFs, a common reaction scheme is the on-surface polymerization of multiply halogenated organic monomers through a three-step reaction: The first step is the heterogeneously catalyzed homolysis of all halogen substituents, followed by the second step, surface diffusion of surface-stabilized radicals, where the lone pair electrons form bonds with the substrate, and completed by the third step, addition of the resulting (poly)radicals into covalently cross-linked networks. Homolysis and radical diffusion were found to depend on material and crystallographic orientation of the substrate [14, 156]. Radical addition – the third reaction step – is kinetically controlled and irreversible, due to the high reactivity of the radicals and the strength of the newly formed C-C bond; consequently, without special precautions or a sophisticated monomer design, the covalent networks are generally irregular. While the pioneering polymerization studies relied on bromine

substitution [96], iodine substitution was employed subsequently [15]. The type of halogen atom is an important reaction parameter with tremendous impact on the reaction kinetics. The C−I bond (2.84 eV in iodobenzene) is significantly weaker than the C−Br bond (3.49 eV in bromobenzene) [96]; thus, bond breaking is easier for iodine substituents. Temperature programmed desorption (TPD) experiments suggest that the adsorption energies of Br and I on Au(100) are comparable [12, 105], while the I−Au bond is less ionic than the Br−Au bond as anticipated from the lower electronegativity of iodine. Bieri et al. were the first to report on synthesis of extended and well-ordered 2D covalent networks that were synthesized from a rather large iodinated cyclohexa-m-phenylene monomer [14, 15]. This monomer already represents a significant part of the targeted "porous graphene" structure, and the resulting covalent networks feature larger domains with low defect density. Moreover, the authors demonstrated that the (111) surfaces of the coinage metals Cu, Ag, and Au are sufficiently reactive to catalyze the initial dehalogenation reaction at room temperature. Yet, at room temperature the resulting large-hexaradicals are immobile on the surface and the third reaction step still requires thermal annealing on either surface. The motivation of the present study is to explore possibilities for complete polymerization of monomers through radical addition into covalent networks at room temperature. To this end comparatively simple and small iodinated monomers were chosen, because the iodine functionalization features homolysis at room temperature and smaller surface-stabilized radicals may still be mobile at room temperature. The main focus is to compare covalent structures and networks obtained from two triply iodinated aromatic molecules, namely, 1,3,5-triiodobenzene (TIB) and 1,3,5- tris(4'-iodophenyl)benzene (TIPB) (cf. insets in Figs. 4.13a and 4.14a for structures). Both molecules are similar in symmetry and functionalization, but differ in the size of the organic backbone. The Au(111) surface was chosen, because it is known to catalyze the iodine homolysis at room temperature and was the best candidate for a high mobility of the resulting tri-radicals. After a brief description of the experimental details, the room temperature reactions of both monomers are compared. In the next section the impact of post-processing by thermal annealing is studied. In the last section, DFT calculations are applied to study the energetics of commonly observed topological defects. DFT derived formation energies of these defects are then compared to experimental occurrence probabilities.

4.2.3   Experimental Methods and Materials

All experiments were conducted with a home-built beetle type scanning tunneling microscope (STM) at room temperature under ultra-high vacuum (UHV) conditions at a base pressure below 3×10^{-10} mbar. The STM was carefully calibrated and lattice parameters and distances were derived from topographs with an accuracy of 0.05 nm. Single crystal metal surfaces were prepared by cycles of Ne$^+$-ion-sputtering and electron-beam annealing at 500 eV and 570 °C for Au(111), 1000 eV and 550 °C for Ag(111), and 1000 eV and 500 °C for Cu(111). The cleanliness of all substrates was verified by STM imaging prior to deposition. Both monomers, 1,3,5-triiodobenzene
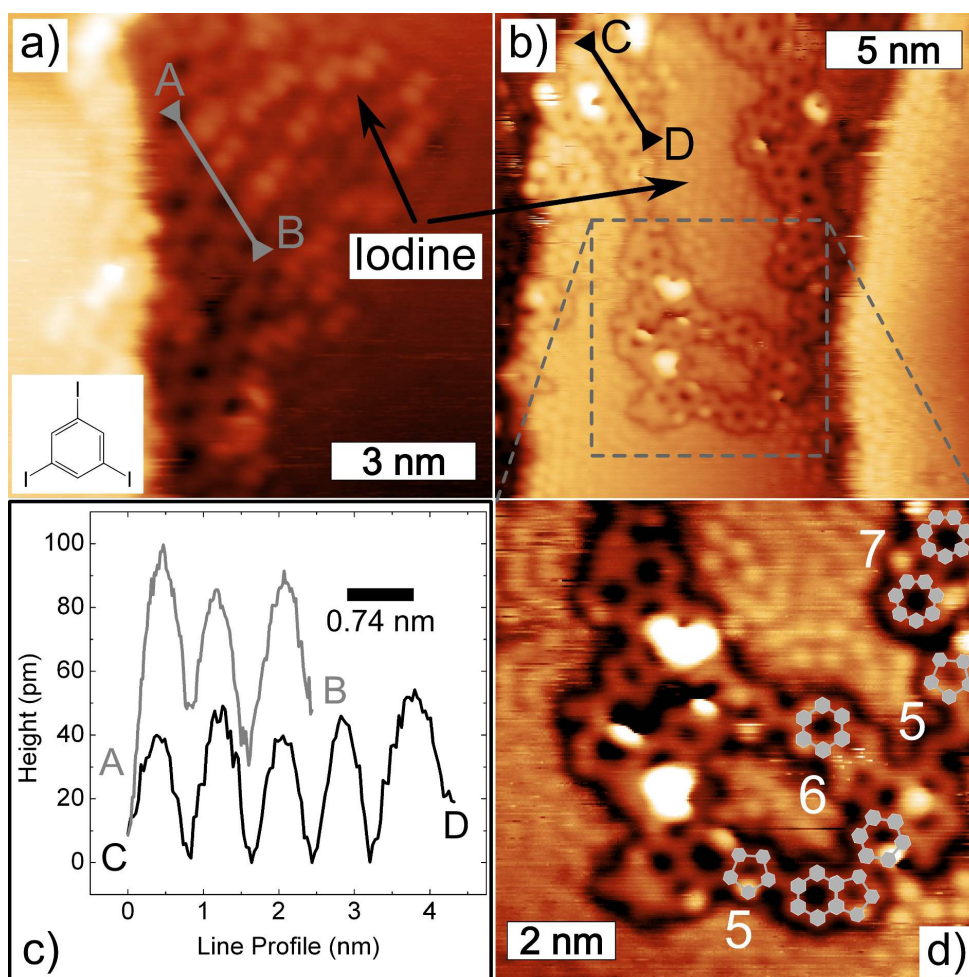
Figure 4.13: STM topographs of TIB on Au(111): (a) as deposited ($V = -0.60$ V and $I = 40$ pA); iodine atoms and fused phenyl rings are found close to step-edges; covalent networks are partly covered by split-off iodine atoms impairing STM resolution. The inset shows the structure of unreacted TIB (b) after annealing to $450\,°$C for 8 min ($V = 0.70$ V and $I = 50$ pA); the networks grow larger, while the iodine atoms still remain adsorbed on the surface, yet with improved order. Lattice parameters amount to $((0.74 \pm 0.05)$ nm for the covalent networks and (0.50 ± 0.05) nm for the iodine superstructure. (c) Extracted line-profiles (vertically offset for clarity): profile A–B extends over three adjacent six-membered rings resulting from TIB room temperature deposition, while profile C–D extends over a series of fused six-membered rings after annealing. The lattice parameters for both preparation procedures are equally 0.74 nm in full agreement with theoretical values. (d) Enlarged scan of (b) showing 5-, 6- and 7-membered rings. The figures indicate the number of monomers that constitute the respective ring.
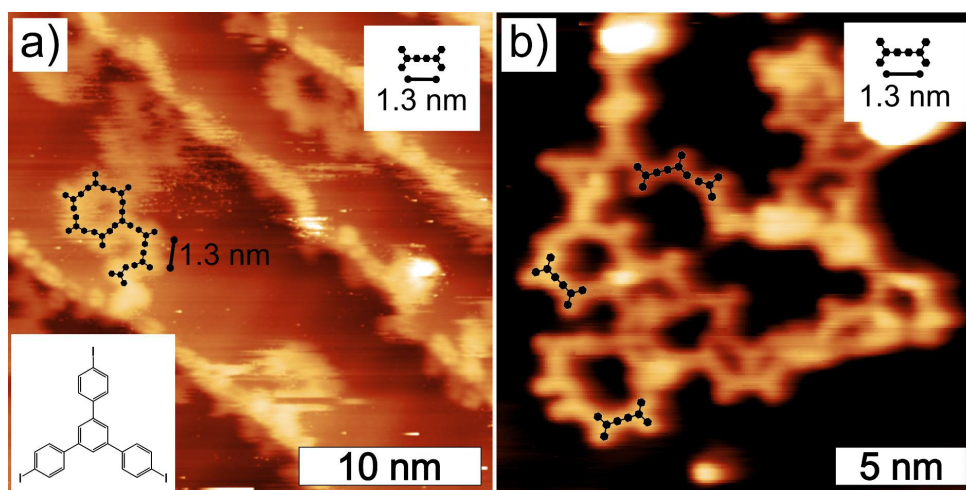
Figure 4.14: STM topographs of TIPB on Au(111) (a) as deposited ($V = -1.60\,\mathrm{V}$ and $I = 40\,\mathrm{pA}$); covalently interlinked oligomers, mostly dimers and trimers are observed near step-edges. The center-to-center distances of dimers account to $(1.3 \pm 0.05)\,\mathrm{nm}$, indicating covalent interlinks. The inset shows the structure of unreacted TIPB (b) after annealing to $450\,^{\circ}\mathrm{C}$ for 10 min ($V = -3.30\,\mathrm{V}$ and $I = 40\,\mathrm{pA}$); annealing was found to promote the growth into larger networks, whereby the center-to-center distance of interlinked monomers remains unchanged at $1.3\,\mathrm{nm}$. Models of covalently interlinked aggregates are overlaid.

(TIB, CAS 626-44-8, purity not specified) and 1,3,5-tris(4'-iodophenyl)benzene (TIPB, CAS 151417-38-8, purity 90%), were obtained from Sigma Aldrich, Germany. TIB was deposited through a high precision sapphire leak valve equipped with a drift tube directly aiming at the sample. In order to obtain a high enough vapour pressure, TIB was preheated to $120\,^{\circ}\mathrm{C}$. TIPB was evaporated from a home-built Knudsen cell with integrated quartz crystal microbalance at crucible temperatures between $150\,^{\circ}\mathrm{C}$ and $155\,^{\circ}\mathrm{C}$ [57]. Prior to deposition both molecules were thoroughly outgassed and no impurities could be detected in the STM measurements. During all deposition procedures, the substrates were held at room temperature.

4.2.4   Results and Discussion

Room temperature deposition

already results in polymerized covalent aggregates. STM topographs are depicted in figure 4.13a for TIB and figure 4.14a for TIPB. The covalent nature of intermolecular bonds is verified by a thorough analysis of center-to-center distances between interlinked monomers or adjacent rings for larger networks and comparison to theoretical values. Assuming formation of ideal structures with unstrained intermolecular bonds, both molecules should polymerize into regular porous hexagonal covalent networks with lattice parameters (center-to-center distance of interlinked dimers) of $0.74\,\mathrm{nm}$ ($0.43\,\mathrm{nm}$) and $2.20\,\mathrm{nm}$ ($1.30\,\mathrm{nm}$), respectively. These theoretical values originate from DFT calculations (cf. 4.2.5) and were confirmed by recent STM experiments on similar covalent networks, synthesized from alternative monomers [15, 19]. The experimental values for both iodinated monomers are found in perfect agreement
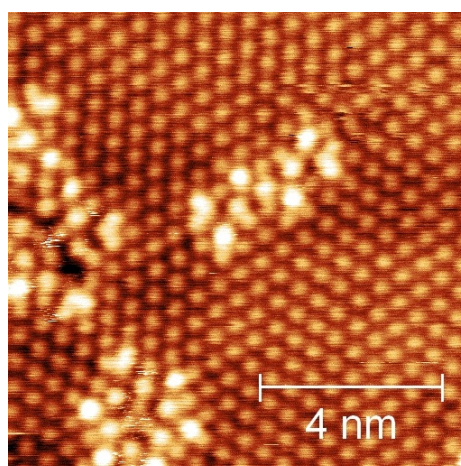
Figure 4.15: STM topograph of an iodine adlayer on Ag(111) observed after TIB deposition ($V = -0.85$ V, $I = 50$ pA). The lattice parameter of this hexagonal superstructure amounts to (0.48 ± 0.05) nm in perfect agreement with literature values of pure iodine monolayers. Similar iodine superstructures were also observed on Cu(111).

with the theoretical predictions, for instance adjacent six-membered rings resulting from TIB polymerization are spaced by (0.74 ± 0.05) nm (figure 4.13a and c), while the dimer center-to-center distance of TIBP derived structures is (1.3 ± 0.05) nm (figure 4.14a and b). Any type of non-covalent intermolecular bond would result in detectably increased intermolecular distances and / or different bond geometries. Yet, the two triply iodinated monomers polymerize distinctly different on the same Au(111) substrate: while the smaller TIB molecule yields cross-linked networks (figure 4.13a), the larger TIPB molecule forms only oligomers, mostly dimers and trimers (figure 4.14a). Typically, the polymerized structures obtained upon room temperature deposition could not be imaged with high resolution either because the structures are partly covered by the split-off iodine atoms (TIB) or because the dimers and trimers were not fully stabilized on the surface at room temperature and exhibit residual mobility (TIPB). Yet, after thermal annealing the STM image quality could be significantly improved for networks from both monomers, because the iodine atoms rearrange and adsorb in the vicinity of the networks and the covalent aggregates grew larger, featuring a better stabilization on the surface (Figs. 4.13b and 4.14b). In order to study the substrate influence, TIB was likewise deposited onto Ag(111) and Cu(111). For both substrates regular hexagonal superstructures of clearly separated spherical protrusions with similar lattice parameters of (0.48 ± 0.05) nm were observed (cf. 4.15). However, this value is too small for regular covalent networks, but is in perfect agreement with previously published lattice parameters of iodine monolayers on Ag(111) [134] and Cu(111) [69].

Consequently, the superstructures observed on silver and copper are identified as iodine monolayers, and surprisingly no covalent organic networks were observed by STM. Occasionally observed impurities might originate from the organic remainder of the monomer. These results reveal important differences between smaller brominated vs. iodinated monomers. For both iodinated monomers the polymerization reaction,

including homolysis and diffusion of radicals, readily proceeds at room temperature without the need for additional thermal activation. In contrast, room temperature deposition of 1,3,5-tris-(4'-bromophenyl)benzene (TBPB) – the brominated analogue of TIPB – on Au(111) resulted in self-assembly of intact molecules [19]. For TBPB on Au(111) either post annealing up to 110 °C or deposition at elevated substrate temperature was required to activate the polymerization. A further notable difference is the adsorption state of the reaction by-product, the split-off halogen atoms. For brominated monomers on various coinage metal surfaces, the split-off Br atoms are not clearly resolved and only give rise to apparent depressions near step-edges on Cu(111) in low temperature STM [17]. This is very surprising, because according to TPD results Br should adsorb stably even at higher temperatures [102]. In contrast, in the synthesis of 1D polymers from diiodobenzene isomers on Cu(110), regular strings of equidistant iodine atoms spaced by 0.51 nm were observed along the troughs of this more anisotropic surface [86]. Also in the present study, iodine was clearly observed in the STM images, and even forms ordered superstructures after thermal activation (vide infra). Furthermore, the Au(111) substrate gives rise to an interesting difference in comparison to less noble metal substrates as copper and silver. Doubly and triply brominated monomers also spontaneously react upon deposition at room temperature onto Cu(111) into interlinked chains and networks, respectively [17, 59]. However, these networks were not yet covalently interlinked but stabilized by metal coordination bonds. In the on-surface reaction of either brominated or iodinated monomers on copper, the halogen atoms are split-off, but the resulting radicals form coordination bonds with mobile copper atoms supplied by the adatom gas rather than covalent interlinks. These metal coordination networks – termed proto-polymers – were found to be metastable and could be converted into covalent networks by further thermal annealing [86, 59]. Formation of proto-polymers is indicative for a reaction mechanism resembling the Ullmann reaction [163]. In this famous reaction, copper catalyses biphenyl formation from iodobenzene in solution via an intermediate state, where both phenyl radicals bond to copper. For the surface analogue of the Ullmann reaction on Cu(111), thermal annealing is required to convert proto-polymers into covalent structures [17, 163]. In contrast, on Au(111) proto-polymers have never been observed at room temperature, but already covalently interlinked molecules. This becomes obvious in figure 4.13a, where a lattice parameter of 0.74 nm indicates direct formation of covalently interlinked structures. These observations can either mean that proto-polymers are bound weaker on Au(111), hence are not stable at room temperature and short lived, or hint towards a deviating reaction mechanism. This important question on the detailed reaction mechanism might possibly be addressed by future temperature dependent experiments.

Post-processing by thermal annealing

In order to study the effect of post preparation on the covalent aggregates, networks prepared from room temperature deposition of both TIB and TIPB onto Au(111) were annealed at different temperatures from 400 °C up to 600 °C. Albeit these

temperatures are too low for breaking C−C bonds, morphological changes have nevertheless been observed. Subsequent annealing of the TIB networks up to $(400-450)°$C for 8 min results in an increased domain size of the covalent networks and more regular iodine superstructures, cf. figure 4.13b. Iodine superstructures and polymers can clearly be distinguished by their distinctly different appearance in the STM contrast. While iodine domains appear with spherical, clearly separated entities with a nearest neighbor spacing of (0.50 ± 0.05) nm indicating single atoms, the covalent networks appear as interconnected structures with uniform height without any dips. Also a very clear boundary with dark contrast separates these two different types of domains as evident in figure 4.13d. Although the organic networks are still irregular, several ideal six-membered rings with the anticipated "lattice parameter" of 0.74 nm (as shown in the extracted line-profiles in figure 4.13c) can now more clearly be discerned. The lattice parameter of the hexagonal superstructure formed by the split-off iodine atoms is in perfect agreement with the $(\sqrt{3} \times \sqrt{3})R\,30°$ iodine superstructure found for lower coverages of pure iodine on Au(111) [62]. Since for TIB polymerization a significant portion of the surface is covered by iodine, a further interesting aspect for both monomers is the ratio of surface area covered by iodine atoms to surface area covered by the organic networks. This ratio is significantly higher for TIB than for TIPB, due to the smaller size of its organic backbone. Theoretical estimates can be obtained based on lattice parameters of ideal hexagonal covalent networks and the iodine superstructure. According to these values, TIB polymerization yields surface coverages of approximately 58% iodine and 42% organic networks as compared to 14% iodine and 86% organic networks for TIPB. Consequently, larger monomers aid in reducing the surface coverage of the unwanted, but stably adsorbed reaction by-products at the cost of reduced radical mobility. However, it was difficult to experimentally confirm these theoretical values, because the covalent networks were not ideal and good statistics could not be obtained. The increase of the TIB domain size upon annealing at $\sim$450 °C can be explained by coalescence of covalent domains, rather than addition of single monomers to the preexistent structures. Due to the rather high diffusivity and reactivity of small TIB derived triradicals, single monomers have never been observed after room temperature deposition, but only interlinked aggregates. Even at $\sim$500 °C the thermal energy is too low for breaking strong C−C bonds (e.g., 4.38 eV for the methyl-phenyl bond [96]) and release single monomers from covalently interconnected networks. Also at this elevated temperature monomers would not be stable on the surface anymore and desorb. Accordingly, it is highly unlikely that free single monomers become available through annealing. It is more likely that the comparatively high temperatures are required to enable surface diffusion of relatively large pre-polymerized organic units.

Annealing the TIB networks obtained at room temperature to higher temperatures up to 550 °C for 5 minutes already leads to disappearance of iodine from terraces, and iodine atoms are mostly found at step-edges (figure 4.16a). As evident from the overview topograph presented in figure 4.16a the step-edge morphology changes drastically. Step-edges become rounded and do not exhibit a preferred distinct
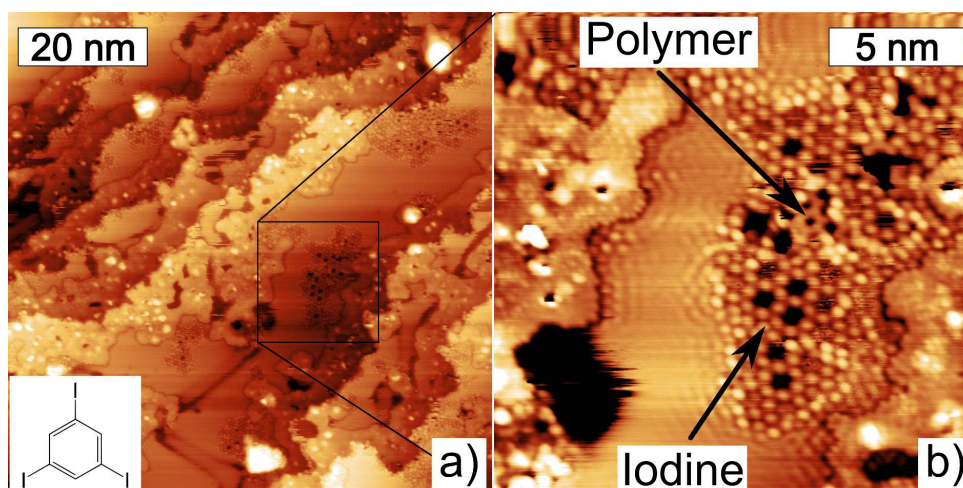
Figure 4.16: STM topographs: (a) Annealing of TIB networks to $550\,°C$ results in reorganisation of iodine atoms and an increase of the lattice parameter to $(0.60 \pm 0.1)\,\text{nm}$. Small patches of the polymer still remain on the surface ($V = 0.30\,\text{V}$ and $I = 40\,\text{pA}$). (b) Enlarged scan of the area marked by the black square in (a) ($V = -0.30\,\text{V}$ and $I = 40\,\text{pA}$).

crystallographic orientation anymore as commonly found for clean substrates. This indicates that iodine interacts with the step-edges at elevated temperature. The terraces still remain atomically flat and there are no hints toward a global iodine induced roughening of the surface. Interestingly, the nearest neighbor spacing of iodine increases from $0.50\,\text{nm}$ found for lower annealing temperatures, to $(0.60\pm0.1)\,\text{nm}$ (see figure 4.16b). Various coverage dependent superstructures were previously found for iodine adlayers on Au(111), where the iodine packing density decreases with coverage [62]. Based on these results, we suggest that the less dense iodine packing could be caused be a decreasing surface coverage of both polymers and iodine. Further annealing of the TIB derived networks up to $600\,°C$ for 5 minutes leads to almost complete thermal desorption of the whole iodine adlayers, as revealed by subsequent STM experiments. The surface still remains atomically flat and only some iodine atoms remain at rounded step-edges (figure 4.17).

This finding is in qualitative agreement with TPD results from iodine monolayers, which, however, find the desorption peak maximum already at $450\,°C$ on Au(111) [145]. Yet, only small domains of the covalent networks remain after such a harsh thermal treatment, suggesting that the covalent networks already start to desorb, possibly after a preceding decomposition step. STM data were only acquired after cooling down to room temperature; hence, it is not possible to draw solid conclusions on the exact decomposition mechanism Thermal annealing of TIPB derived oligomers at $\sim420\,°C$ for 8 minutes results in morphological changes by a secondary polymerization. The covalent dimers and trimers obtained at room temperature become fused into larger networks, albeit with significant higher defect density than for TIB, cf. figure 4.14b. Again, the thermal treatment also influences the iodine adsorption structure. For low surface coverage, thermally activated surface diffusion facilitates nucleation of iodine at the elbow sites of the Au(111) herringbone reconstruction (figure 4.18).
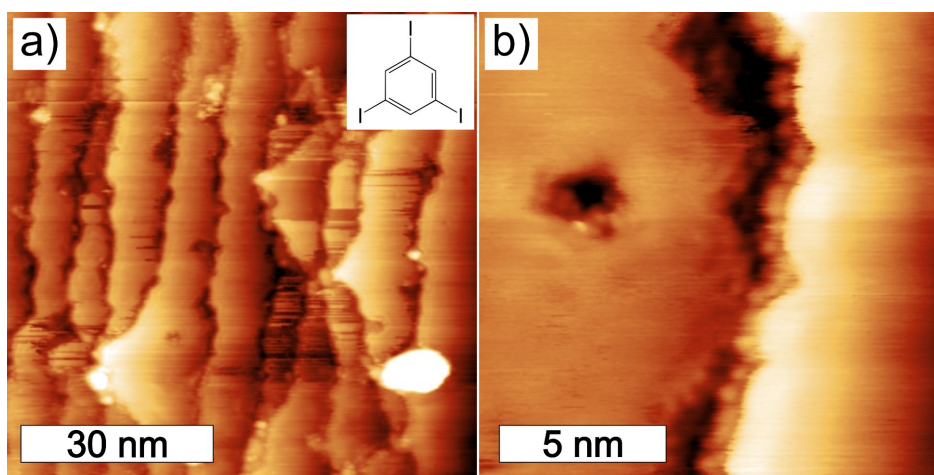
Figure 4.17: STM topographs of TIB (cf. inset) deposited onto Au(111) and thermally annealed to 600 °C. Both iodine adlayers and covalent networks on terraces are desorbed, only some iodine atoms remain at rounded step edges. (a) ($V = -0.15$ V, $I = 60$ pA) (b) ($V = -0.63$ V, $I = 50$ pA)

These sites are known to exhibit the strongest interactions with various adsorbates on the spatially inhomogeneous herringbone reconstruction, and can thus also act as nucleation centers [26]. Enhanced surface diffusivity of the covalently interconnected aggregates also facilitates formation of larger networks, albeit with a rather high defect density. Covalent networks obtained from the brominated monomer TBPB on Cu(111) and Au(111) appear more reticular, where pores are still not ideal but mostly closed [19]. An important difference for the polymerization kinetics might be that for TBPB on Cu(111) and Au(111) the extended networks polymerize from monomers rather than from preformed oligomers as for TIPB on Au(111). On Cu(111) TBPB derived proto-polymers already form at room temperature and can subsequently be converted into covalent networks without significant morphological changes. For deposition of TBPB onto Au(111) at room temperature the bromine homolysis is kinetically hindered and only takes place when additional thermal energy is supplied. At elevated temperature, however, the C−Br bonds are cleaved and the surface-stabilized radicals are mobile, resulting in extended networks. In contrast, TIPB forms only smaller covalent aggregates at room temperature, although the iodine homolysis takes place and single monomers covalently interlink. Since these covalent aggregates do not grow further at room temperature, it can be assumed that they are already immobilized as a consequence of their increased size and thus interaction with the substrate. Dimers are comparable in size to the likewise immobile hexaphenylene monomers studied by Bieri and coworkers [19]. Consequently, already dimers are not mobile anymore at room temperature; hence, the networks cannot grow further. A secondary polymerization of these conformationally less-well defined TIPB dimers and trimers into extended networks is different from direct polymerization of monomers as for TBPB. In conclusion, we suggest that the different morphology observed for TIPB polymerization is related to their pre-polymerization into oligomers already at
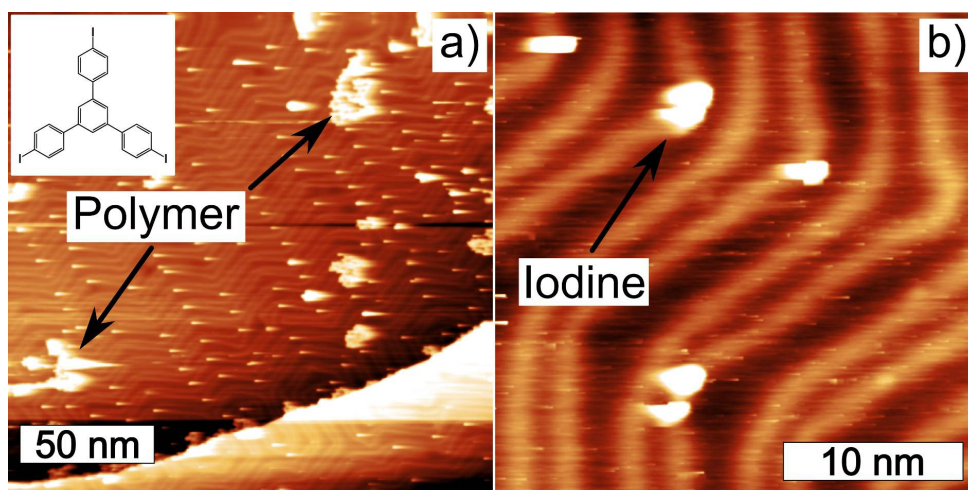
Figure 4.18: STM topographs: (a) Annealing of TIPB samples with low coverage at 420 °C for 8 min facilitates diffusion of iodine atoms to the elbow sites of the Au(111) herringbone reconstruction ($V = -3.10$ V and $I = 50$ pA). (b) Close-up of iodine atoms at elbow sites ($V = -2.70$ V and $I = 50$ pA).

room temperature.

Analysis and Simulation of Topological Defects

In contrast to the large six-fold halogenated hexaphenylene monomer, the covalent networks obtained from simpler triply halogenated monomers are less regular and exhibit a high density of topological defects. Typically observed defects upon polymerization of these simple tritopic monomers are non-ideal rings that consist of less or more than six monomeric units (examples are marked by gray overlays in figure 4.13d). On the other hand polymerization of the large hexaphenylene monomers with a more complex topology of binding sites promotes formation of vacancies or dendritic growth [14]. So the type of defect is to some extend predetermined by structure and halogen substitution pattern of the monomer. In order to shed light on defect formation during polymerization, the energetics of commonly observed, topologically well-defined defects was studied by DFT calculations (cf. section 4.2.5 for details). Total energies of 5-, 6-, and 7-membered rings were calculated for networks derived from both TIB and TIPB monomers. To facilitate comparison between the different monomers and rings, the respective total energies were normalized to the number of phenyl units in each ring, e.g., 5 for a 5-membered TIB derived ring and 15 for a 5-membered TIPB derived ring, results are depicted in figure 4.19.

As anticipated, for both monomers the 6-membered rings with perfectly straight phenyl-phenyl bonds represent the energetic minima. Interestingly, the energy difference between ideal 6-membered and strained 5- or 7-membered rings is significantly smaller for the larger TIPB monomer than for the smaller TIB monomer. Most of the strain is compensated by the phenyl-phenyl bond and the aromatic units remain nearly unaffected. Accordingly, the results can readily be explained by the magnitude of phenyl-phenyl bond distortions which are directly related to the number of phenyl
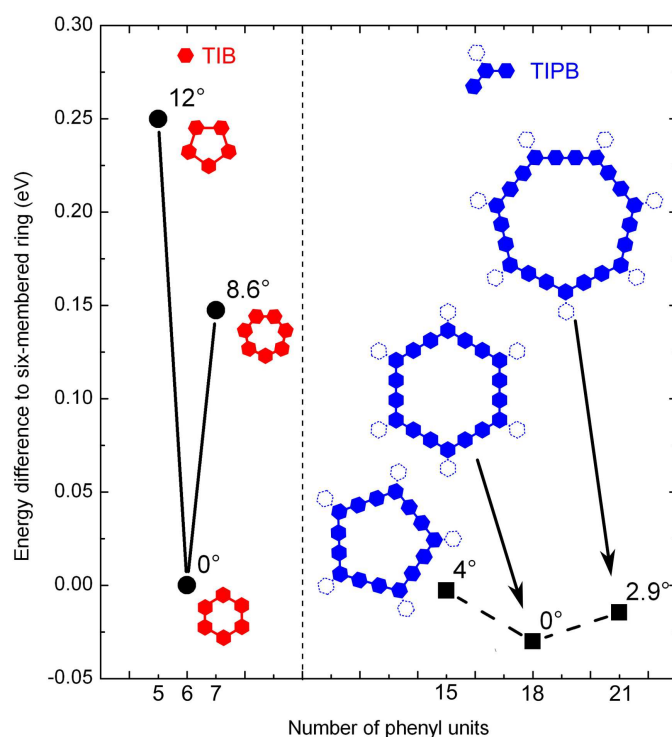
Figure 4.19: DFT derived total energies per phenyl unit for 5-, 6-, and 7-membered rings resulting from TIB (red) and TIPB (blue) polymerization. As illustrated by the insets, only isolated inner rings saturated with hydrogen were considered (the dashed phenyl rings of TIPB are only shown for clarity, but were not considered in the calculation). Corresponding cyclic structures from TIPB consist of a factor three more phenyl units in the respective ring. Average angular distortions of phenyl-phenyl bonds are given next to each data point. The energies are referred to the 6-membered TIB ring.
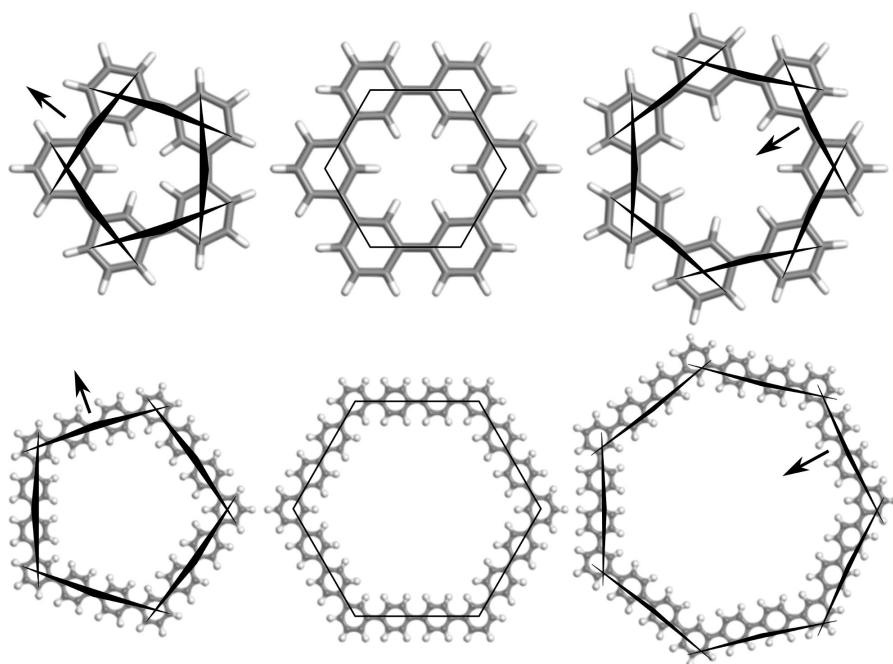
Figure 4.20: Visualization of the bond distortion in polyphenylene rings resulting from polymerization of 5, 6, and 7 monomeric units (left to right). The structures depict results of a DFT geometry optimization. The upper row refers to the TIB monomer, the lower row refers to the TIPB monomer. For both monomers the six-membered rings represent the optimal structure with undistorted phenyl-phenyl bonds. The amount of bond distortion (as indicated by the triangle, the distortion direction is made clear by the black arrows) is in both cases larger for the 5-membered ring than for the 7-membered ring.

rings along the circumference of a nonideal ring. For instance, in a 5-membered TIB ring the loop has to be closed by angular distortion of only five phenyl-phenyl bonds, whereas in the 5-membered TIPB ring, 15 phenyl-phenyl bonds are available for ring closure. Thus the required average angular distortion of each phenyl-phenyl bond is significantly smaller in the TIPB 5-ring ($4\,°$) as compared to the TIB 5-ring ($12\,°$), resulting in a lower energy cost that possibly manifests itself in a higher formation probability of non-ideal TIPB rings (see figure 4.20 for a visualization of bond distortions).

In order to relate these theoretical results to the experiment, a statistical analysis for covalent networks obtained from TIB polymerization was conducted. The covalent networks obtained from TIPB are irregular and exhibit mostly not clearly classifiable topological defects and could thus not be evaluated. A statistical analysis of 76 rings in several (20×20)nm^2 STM topographs of different regions of post annealed TIB samples ($450\,°$C for 8 min) resulted in 56% 6-membered rings, 40% 5-membered rings, and only 4% 7-membered rings. The high probability for ideal 6-membered rings correlates well with its energetic preference. However, for an equilibrium distribution the energetically more favourable 7-membered rings should be preferred over 5- membered rings. But formation of 7-membered rings is kinetically disfavoured because more monomers are required to close the ring. On the other hand these results clearly demonstrate that the reaction kinetics and the irreversibility of the
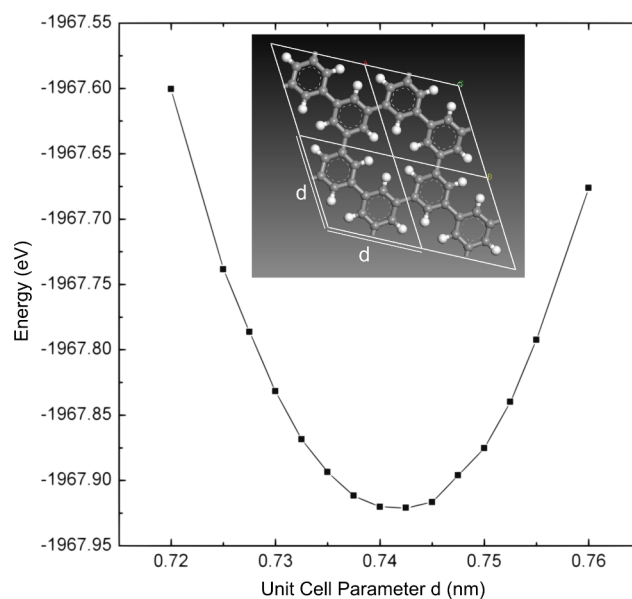
Figure 4.21: DFT derived total energies (per unit cell) of two-dimensional infinite polyphenylene networks as a function of enforced lattice parameter in a hexagonal unit cell. Periodic boundary conditions were applied for these calculations. The energetic minimum corresponds to a lattice parameter of $0.74\,\text{nm}$. Inset: 2×2 unit cells of the calculated structure.

covalent bond are mostly responsible for defect formation in these networks.

4.2.5 DFT Results

Lattice parameter and band structure of infinitely extended polyphenylene networks

Experimental lattice parameters of the polyphenylene networks were compared with DFT structure simulations based on a gradient corrected (GGA) functional PW91 [113] with plane wave basis set as implemented in the CASTEP code [137]. The substrate influence was neglected, because for covalent structures molecule-molecule interactions are significantly stronger than molecule-substrate interactions. Total energies per unit cell were calculated as a function of lattice parameter for a hexagonal unit cell with periodic boundary conditions. The energy vs. lattice parameter curve as shown in figure 4.21 exhibits a parabolic shape; the energetic minimum at $0.74\,\text{nm}$ was assigned to the optimized lattice parameter. Our DFT calculations are also in accordance with previously published Molecular Mechanics simulations and experiments [15]. The electronic structure of the perfectly periodic network exhibits semiconducting behavior with a direct bandgap of $\sim 3\,\text{eV}$. Yet, since DFT is known to underestimate band gaps [32], the actual bandgap might be larger (cf. figure 4.22)
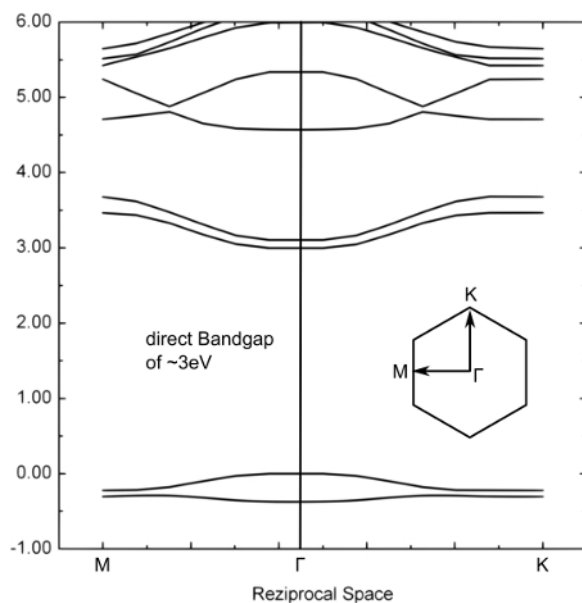
Figure 4.22: DFT results depicting the electronic band structure of the geometry optimized polyphenylene network with 0.74 nm lattice parameter. Although the CASTEP code underestimates the bandgap, the direct bandgap is nevertheless in the order of 3 eV.

Structure and energy of Isolated Polyphenylene Rings

Energies of geometry optimized isolated polyphenylene rings were calculated using Gaussian09 [48] with a B3LYP functional and a 6-31G* basis set applying standard convergence criteria. Considered were polyphenylene rings consisting of 5, 6, and 7 monomeric units, corresponding to 5-, 6-, and 7-membered polyphenylene rings in the case of TIB polymerization, and 15-, 18-, and 21- membered polyphenylene rings in the case of TIPB polymerization. Again the substrate was neglected, and the rings were forced into planar geometry. For the larger rings resulting from TIPB polymerization, only the inner phenyl units were considered and the rings were saturated with hydrogen. Total energies as depicted in figure 4.19 were normalized to the number of phenyl units in each ring.

4.2.6   Conclusion

In summary, these experiments further confirm that iodinated precursors are easily dehalogenated at room temperature by even the catalytic properties of the Au(111) noble metal surface. In contrast to larger monomers, the smaller tri-radicals are still mobile at room temperature; hence, the polymerization of these monomers can take place without additional thermal activation. In contrast to previous studies, where the split-off bromine substituents were hardly observed in STM, iodine forms rather stable, in STM experiments clearly observable superstructures. In particular for monomers with comparatively small organic backbone as TIB, the split-off iodine atoms can cover a large portion of the surface, and thus hamper the polymerization. An interesting aspect is the influence of monomer size on the network formation.

While for the smaller TIB monomers crosslinked networks were already observed at room temperature, polymerization of the larger TIPB monomers only yielded oligomers. Thermal post-processing induces growth of the covalent networks and rearrangement and desorption of the iodine atoms for both monomers. Unfortunately, at the temperatures required for iodine desorption, the covalent networks are not stable anymore and start to disintegrate. The covalent networks obtained from TIPB monomers are rather fragmented and irregular. In contrast, polymerization of the analogous brominated monomer with similar backbone yields likewise irregular, but reticulated covalent networks. We rationalize this observation by the successive two-step polymerization of TIPB upon annealing. The first polymerization takes place at room temperature and results in immobile oligomers. Only after thermal annealing these oligomers polymerize into networks. Thermal healing of topological defects has not been observed in these studies up to temperatures of $600\,^\circ\mathrm{C}$, where the covalent networks already disintegrate. Lastly, formation energies of commonly observed topological defects were evaluated by DFT calculations. The formation energies are not extraordinarily high and as the experiment shows can be overcome at room temperature. The energetic cost of defects could in part be correlated with their experimentally observed probability of occurrence. With all this in mind, the challenge is now to design monomers and / or realize preparation conditions, where formation energies of defects are decisive in order to prepare long range ordered 2D COFs.

4.3 Molecular Dendritic Structures of Tetraiodotetrathiafulvalene on Au(111)

4.3.1 Introduction

To modify the electronic properties of materials, it is common to introduce different types of atoms into semiconductors or metals, i.e. to dope materials [142]. In the field of polymer synthesis, doping can be achieved by post-functionalization of the preexisting material or by using conventional click chemistry to introduce different acceptor-type and donor-type monomers [98]. Bottom-up synthesis of two-dimensional polymers can enhance the electronic properties in the same way by using altered monomers with substituted atoms. This has already been done extensively introducing boroxine rings via polycondensation reaction into polymers [35, 38, 45] or by polymerizing borazine $(BH)_3(NH)_3$ into boron-nitride layers by high temperature exposure to rhodium surfaces [33, 70].

In the emerging field of nanoelectronics and one-dimensional wires, materials with enhanced conductivity play an important role [90]. One possible class of these materials are thiafulvalenes and its derivatives. The molecules consist of two conjugated hydrocarbon-rings with four carbon atoms substituted by sulfur atoms. They serve as strong π-electron donors and can be used for electroactive molecular rods [136], allow for excellent electron conductors [22, 138], or are utilized for switchable molecular structures [23].

STM studies on supramolecular tetrathiafulvalene (TTF) wires with alkane side chains were performed at the liquid-graphite interface [51, 1, 122]. Another promising candidate for bottom-up polymerization on surfaces is 4,5,4',5'-tetraiodo-2,2'-bis(1,3-dithiolylidene), or tetraiodotetrathiafulvalene as a common name (TITTF) (cf. figure 4.23a). This is a molecule with four iodine atoms serving as functional groups for polymerization reactions and a TTF backbone. The synthesis of covalent hybrid carbon sulfur networks will be studied by STM, where thermally induced on-surface homolysis of the iodine functional groups leads to TTF radicals which subsequently recombine and polymerize into networks.

After a brief description of the experimental details, structures of TITTF on Au(111) deposited at room temperature are analyzed. In the next section the impact of post-processing by thermal annealing is studied, while in the last section DFT calculations are applied to compare structural models with the observed molecular structures.

4.3.2 Experimental Methods

All experiments were conducted with a home-built beetle type scanning tunneling microscope (STM) at room temperature under ultra-high vacuum (UHV) conditions at a base pressure below 3×10^{-10} mbar. The STM was carefully calibrated and lattice parameters and distances were derived from topographs with an accuracy of 0.05 nm. Single crystal metal surfaces were prepared by cycles of Ne^+-ion-sputtering and electron-beam annealing at 500 eV and 550 °C for Au(111). The cleanliness of
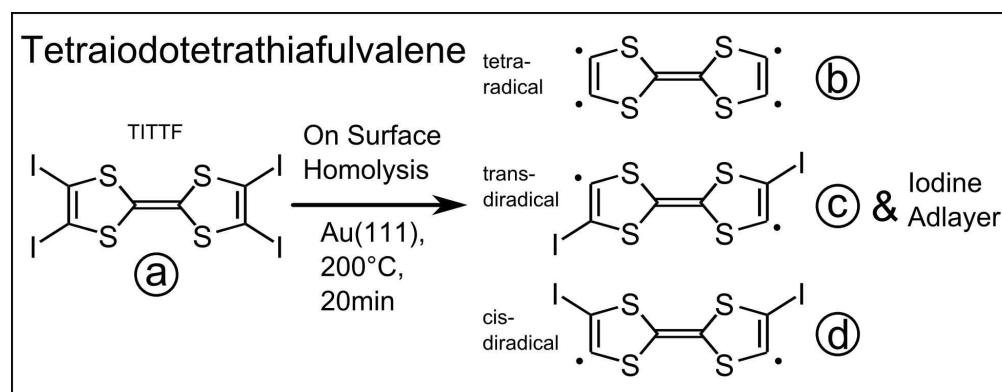
Figure 4.23: Reaction pathways of 4,5,4',5'-Tetraiodotetrathiafulvalene (TITTF) molecules (a): after homolysis the split-off iodine atoms form a hexagonal adlayer. Depending on the degree of homolysis, in addition to completely deiodinated tetraradicals (b) also diradicals in trans- (c) or cis-state (d) can emerge.

all substrates was verified by STM imaging prior to deposition. 4,5,4',5'-tetraiodo-2,2'-bis(1,3-dithiolylidene) molecules were synthesized. No information about the purity was given. The molecules were evaporated at temperatures of 150 °C after sufficient degassing from a home-built Knudsen cell with an implemented quartz crystal microbalance [57]. During the annealing process at a temperature of 200 °C the crystal temperature was monitored by an infrared emission pyrometer.

4.3.3   Results and Discussion

Room Temperature Deposition on Au(111)

Deposition of TITTF molecules held at a temperature of 150 °C for 15 min on a Au(111) surface held at room temperature leads to disordered aggregates of molecules as can be discerned from figure 4.24a. The molecular coverage is about 10%, while the herringbone reconstruction of Au(111) surface is still preserved. A higher resolution topograph reveals single entities within the aggregates but does not allow for an identification of individual molecules (cf. figure 4.24b). No further conclusions can be drawn from STM data of room temperature deposition experiments.

Annealing and Thermal Activation of TITTF

After thermal annealing of this crystal to 200 °C for 20 minutes different structures could be observed. The surface is mainly covered by a hexagonal structure with lattice parameters of (0.5 ± 0.05) nm, as derived by FFT processing of the STM topographs (cf. figure 4.25a). Comparing this experimentally obtained parameter with literature values of halogen adlayers on Au(111) of (0.45 ± 0.05) nm, one finds a good agreement with densely packed iodine adlayers [62, 129].
Although it is known that reactive sites on Au(111) surfaces can lead to homolysis of C−I bonds even below room temperature [145], slight annealing enhances the homolysis rate. The dehalogenated iodine atoms form strong bonds to Au atoms and
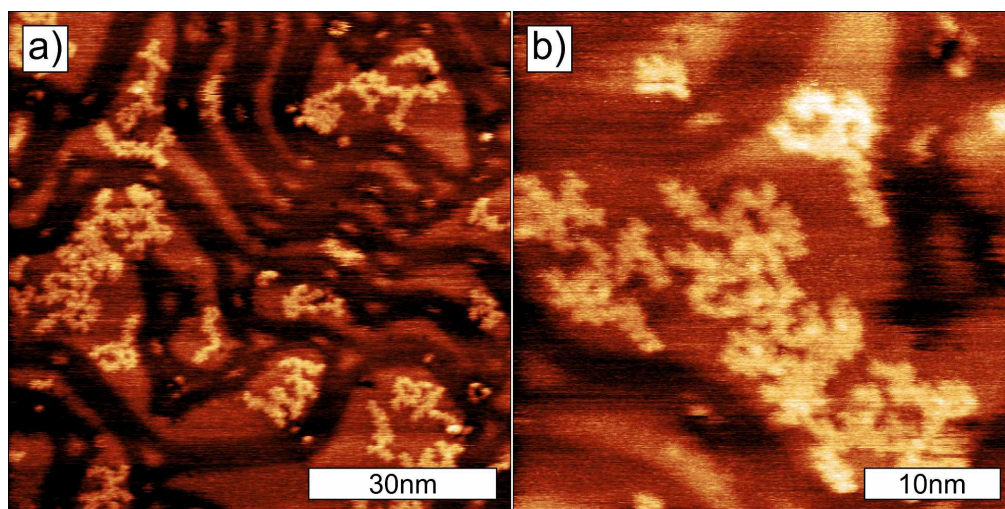
Figure 4.24: STM topograph of TITTF molecules held at a temperature of $150\,°C$ for $15\,min$ after deposition on Au(111) held at room temperature: (a) overview image with remaining herringbone reconstruction ($V = -1.0\,V$ and $I = 40\,pA$); (b) close-up ($V = -1.0\,V$ and $I = 40\,pA$)
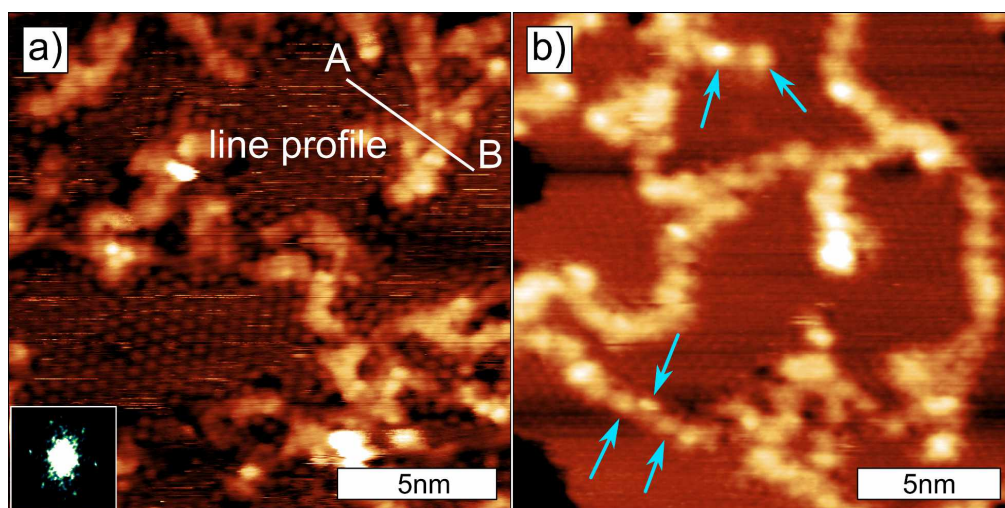

Figure 4.25: STM topograph of TITTF on Au(111) after thermal annealing to $200\,°C$ for $20\,minutes$: (a) A densely packed iodine adlayer can be discerned. Hexagonal lattice parameters of $(0.5 \pm 0.05)\,nm$ were derived from FFT. A line profile is extracted along the white line $A - B$ (see figure 4.26). ($V = -0.6\,V$ and $I = 40\,pA$) (b) Besides the iodine adlayer, spherical protrusions can be distinguished (indicated by arrows). ($V = 0.8\,V$ and $I = 50\,pA$)
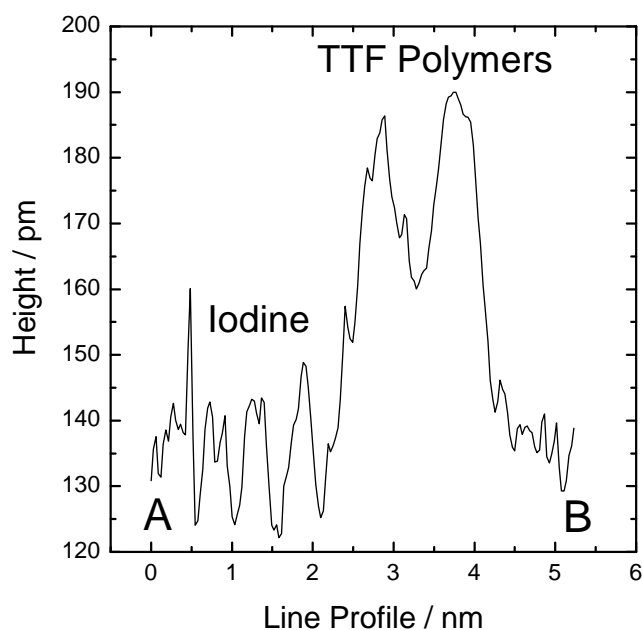
Figure 4.26: Extracted line-profile from figure 4.25a: the profile shows distances between single iodine atoms of $\sim$0.5 nm and a mean height difference between polymerized TTF chains and iodine atoms of $\sim$50 pm.

prefer to arrange in densely packed domains [62]. The agreement of lattice parameter substantiate the conclusion that the surface is partially covered by iodine in a densely packed structure.

Moreover dendritic structures with several branches surrounded by the iodine layer can be discerned (cf. figure 4.25b). The extracted line-profile from figure 4.25a is depicted in figure 4.26. The height difference between the iodine atoms and the TTF chains is below 50 pm, while apparent heights of aromatic molecules on metal surfaces are in the order of 280 pm [63]. This indicates a planar layer of molecules. The individual chains have a width in the order of 1 nm and average distances of about $\sim$5 nm between two branching points. The dendritic structures are always surrounded by iodine layers. Along the dendritic structures, typical distances between single discernible bright spheres (indicated by turquoise arrows in the topography of figure 4.25b) are in the range of (0.8 ± 1.0) nm.

In the literature it is reported that annealing up to 230 °C leads to polymerization of phenylene radicals after iodine dehalogenation on Cu(111), Ag(111) and Au(111) surfaces [14]. If one assumes that TTF molecules behave similar to phenyl rings, the dendritic structure could be assigned to polymerized TTF molecules. It is remarkable that the TITTF molecule, although functionalized for possible polymerization into two-dimensional networks, forms one-dimensional dendritic branches only.

In order to create one-dimensional structures out of a molecule with two possible reaction sites on opposing sides, either a partial homolysis or a partial polymerization can be assumed.

At first a partial homolysis is discussed:

Depending on the degree of homolysis, molecules in different radical states can emerge
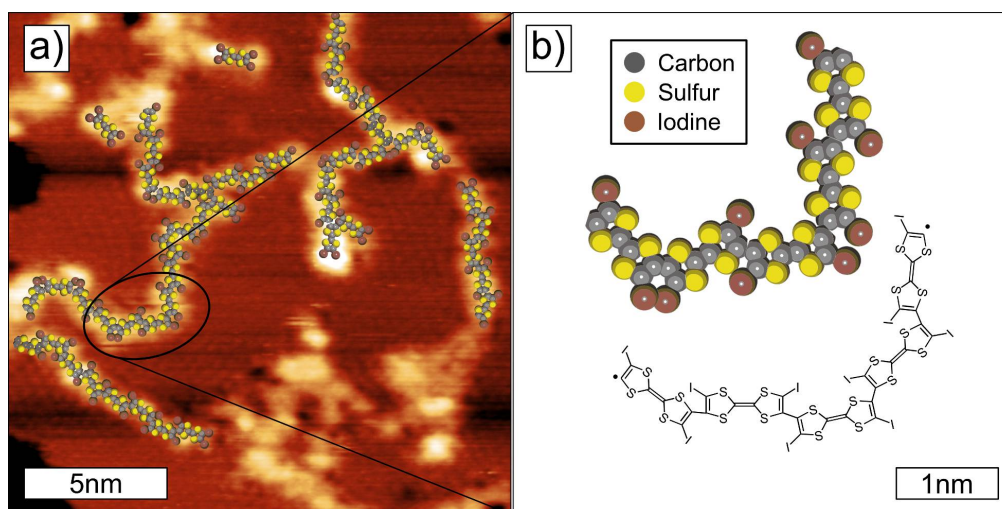
Figure 4.27: STM image with scaled overlay of TTF chains polymerized from cis- and trans-diradicals: (a) Size and symmetry of the one-dimensional chains with branches are in agreement with the overlaid model. (STM topograph $V = 0.8$ V and $I = 50$ pA). A schematic view of the DFT calculated molecular chain is given in (b).

(cf. figure 4.23 (b) to (d)). Besides completely dehalogenated TTF tetraradicals, polymerization of cis- and trans-diradicals can lead to one-dimensional structures. Taking into account a possible chirality of adsorbed molecules on the surface and using cis- and trans-diradicals, curved molecular chains can be formed. Branching can be explained by coupling of cis- or trans-diradicals with TTF molecules with three radical sites.

Two different DFT geometry optimizations of two coupled TTF molecules were performed. A dimer consisting of two TTF molecules forming a linear chain (remaining iodine atoms are on opposing molecular sites) gives a intermolecular distance of 0.82 nm, while a dimer, where two iodine atoms are placed next to each other, gives a chain tilted by an angle of 75° with a intermolecular distance of 0.76 nm. An out of plane rotation of the iodine atoms is caused by steric hindrance. Structural models are visualized in figure 4.28.

Based on these different coupling types, an overlay of molecules with actual polymerized single and branched chains of figure 4.25b can be formed. This model is visualized in figure 4.27. Size and structure are in agreement with the experimental data. Because of the steric hindrance it is useful to take into account interactions between remaining iodine functional groups of not fully homolyzed TTF molecules and the surrounding iodine adlayer. Additional bonds and forces can influence the rotation angle of the dendritic structures.

Up to now partial dehalogenation has never been reported in the literature, however an additional model involving partial polymerization due to steric hindrance is also possible:

The area that is covered by four adsorbed iodine atoms is even larger than the area covered by the backbone molecule TTF. For polymerization several TTF molecules have to aggregate, so a certain TTF density on the surface is needed for fully
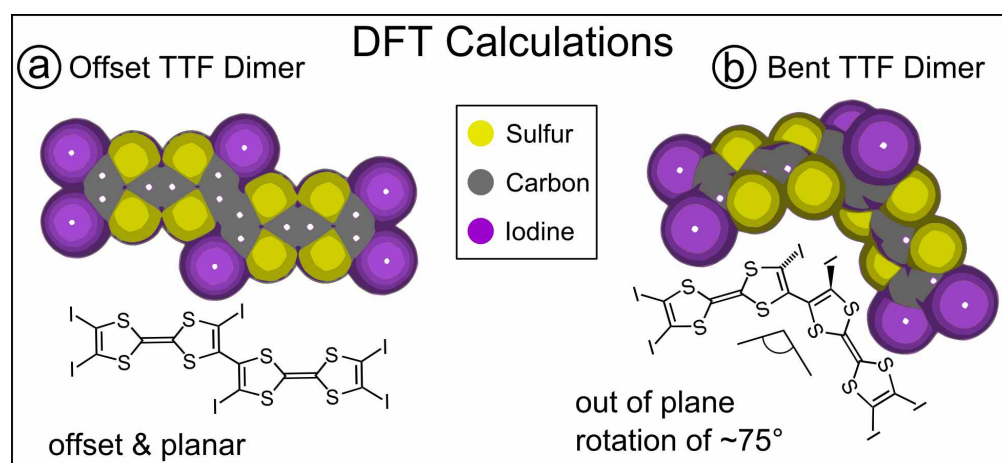
Figure 4.28: Geometry optimization of an offset and a bent dimer. The offset dimer is essentially planar, although the substrate was neglected and no additional constraints were applied. The bent dimer is rotated by 75 °. The iodine atoms are turned out of plane because of steric hindrance. Additional surface effects were neglected.

crosslinked networks. Since the on-surface dehalogenation process leads to adsorbed iodine atoms, this adlayer hampers the network growth. It is possible that the backbone density in the performed experiments is too low. No aggregation of TTF backbones can take place, so the reaction into two-dimensional TTF networks is inhibited and one-dimensional branches emerge only. Remaining active radical sites on the TTF backbone that are not saturated by covalent bonds can introduce surface-supported radicals, which have previously been found on all coinage metal surfaces. According to Bieri et al., the "free electrons of the metal surface couple to the unpaired electrons of the radical" [14].

The TTF molecules have the same structural properties as for example triiodobenzene or triiodophenylbenzene (cf. section 4.2), where the functional group to backbone ratio of the area covered on the surface is too high. The adsorbed iodine atoms hamper the network growth and negatively influence the desired polymerization.

4.3.4 DFT Geometry Optimization of TTF Dimers

Geometry optimized DFT calculations of isolated dimers in two different conformations were conducted using the software package *GAUSSIAN03*, Gaussian Inc., with a B3LYP functional and a 3-21G basis set applying standard convergence criteria [47]. The offset dimer is essentially planar, although the substrate was neglected and no additional constraints were applied. The bent dimer is rotated by 75 °. The results are presented in figure 4.28. Both dimers are shown with their corresponding van-der-Waals surfaces and additionally in schematic view.

4.3.5 Conclusion

Polymerization of TITTF molecules to one-dimensional dendritic structures was performed on a Au(111) surface. The dendritic chains are surrounded by an coadsorbed

iodine adlayer formed by on-surface homolysis of the iodine functional groups. It is remarkable that molecules with four equal reactive sites only create one-dimensional chains with branches instead of fully crosslinked two-dimensional networks. Different explanations like partial homolysis of the TITTF molecule or partial polymerization of the fully dehalogenated TTF radicals were proposed to address these concerns. Partial homolysis has never been reported so far in the literature. Opposite to that, polymer growth hampering induced by halogen adlayers have also been observed with other molecules in this work (see section 4.2). This hampering can be also seen as an additional controllable parameter for selective influence of intermolecular reactions. Although both models are sufficient to explain the experimental data, a partial polymerization in agreement with reported literature is more likely.

4.3.6   Acknowledgment

4.4   Influence of Pendant Groups: Different surface chemistry of Hydrogenated vs. Fluorinated Tribromobenzene on Ag(111) and Cu(111)

4.4.1   Introduction

In order to systematically study the influence of pendant groups on the self-assembly and surface chemistry process, similar experiments are performed with 1,3,5-tribromo-2,4,6-trifluoro-benzene and 1,3,5-tribromobenzene. 1,3,5-tribromo-2,4,6-trifluoro-benzene (TBrTFB) consists of a phenyl ring with two different functional groups (bromine and fluorine) linked to the phenyl ring in an alternating way (cf. figure 4.29a). 1,3,5-tribromobenzene (TBrB) is an organobromine compound with three bromine functional groups attached to a phenyl ring (cf. figure 4.29b). To put it in one sentence: Substitution of the hydrogen atoms in TBrB with fluorine atoms results in TBrTFB. This substitution has two main implications: on the one hand the molecular mass increases by 17% from 314.8 u to 368.8 u, and on the other hand the fluorine atoms act as strong electron acceptors, thus can alter the interaction with the surface and other molecules. In the literature a substitution of hydrogen atoms with different pendant groups is most often used for controlled steric hindrance to influence reaction parameters [159, 119]. Steric hindrance can also influence the self-assembly properties of planar molecules. Methyl pendant groups on phenyl rings alter self-assembly on surfaces through weakening of the aromatic interactions [58]. Moreover, physical and electrochemical behavior, such as water retention, can also be influenced by different pendant groups [157].

In the performed experiments it has not been possible to deposit TBrB neither on Cu(111) nor on Ag(111) surfaces held at room temperature. The adsorption energies are too low to stabilize the molecule at room temperature. Therefore deposition experiments were performed at low temperature with substrates held at 80 K. The different functional groups – fluorine vs. hydrogen – are expected to have a massive impact on adsorption characteristics. Thermal programmed desorption studies by Müller et al. on alkane derivatives with acetic acid and bromoacetic acid functional groups show a variation in desorption energies by a factor of four just by substituting one hydrogen atom with one bromine atom [100]. Given the fact that the cited study used an inert HOPG surface for their desorption experiments, reactive metal surfaces like Ag(111) or Cu(111) in combination with a strong electron acceptor like fluorine could lead to an even higher difference in surface interactions.

After a brief description of the experimental details, room temperature deposition of TBrTFB on Ag(111) and Cu(111) and subsequent annealing to 200 °C and 320 °C is analyzed. Deposition and annealing experiments (up to 500 °C) on Cu(111) follow. To analyze the influence of pendant groups, TBrB was deposited on Ag(111) and Cu(111), both held at low-temperature. In the last section a theoretical approach to model the peculiar molecular structures of TBrTFB on Ag(111) is performed.
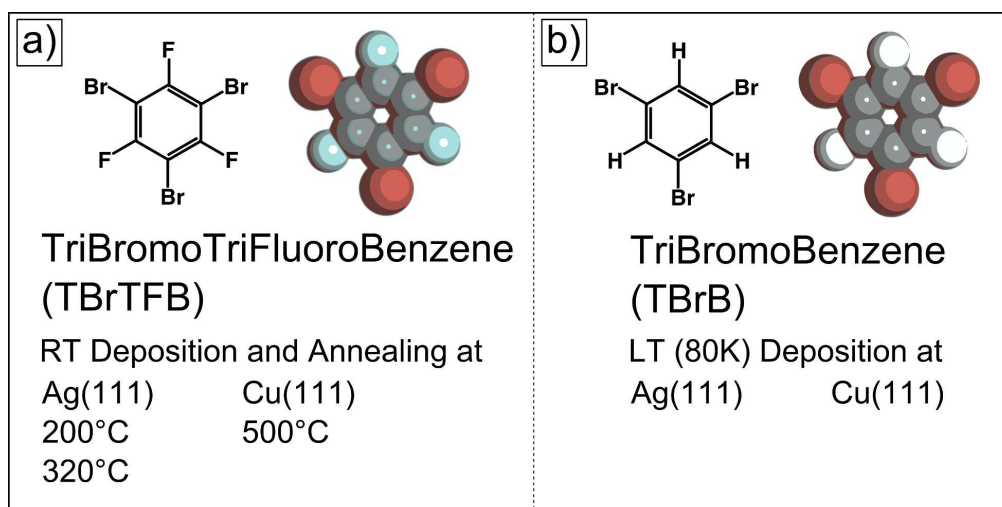
Figure 4.29: Schematic views of the molecular models of TBrTFB and TBrB. TBrTFB consists of a benzene ring with three fluorine and three bromine functional groups. TBrTFB was deposited onto Ag(111) and Cu(111) (a). TBrB consists of a hydrogenated benzene ring with three bromine functional groups and was deposited to Ag(111) and Cu(111), both held at low temperature (b).

4.4.2 Experimental Methods

All experiments were conducted with a home-built beetle type scanning tunneling microscope (STM) at room temperature under ultra-high vacuum (UHV) conditions at a base pressure below 3×10^{-10} mbar. The STM was carefully calibrated and lattice parameters and distances were derived from topographies with an accuracy of 0.05 nm. Single crystal metal surfaces were prepared by cycles of Ne$^+$-ion-sputtering and electron-beam annealing at 1000 eV and 550 °C for Ag(111) and 1000 eV and 500 °C for Cu(111). The cleanliness of all substrates was verified by STM imaging prior to deposition. Both monomers, 1,3,5-tribromobenzene (TBrB, CAS 626-39-1, purity > 98%, molecular mass 314.80 u) and 1,3,5-tribromo-2,4,6-trifluoro-benzene (TBrTFB, CAS 2368-49-2, purity not specified, molecular mass 368.774 u), were obtained from Sigma Aldrich GmbH, Germany. Both molecules were deposited through a high precision sapphire leak valve equipped with a drift tube directly aiming at the sample. Prior to deposition both molecules were thoroughly out-gassed. During deposition procedures of TBrTFB, the substrates were held at room temperature, while TBrB was deposited on substrates cooled to a temperature of ∼80 K with a continuous flow liquid nitrogen cryostat.

4.4.3 Results and Discussions

Deposition and annealing of TBrTFB on Ag(111)

TBrTFB was deposited on a Ag(111) crystal held at room temperature. In STM experiments neither singular entities nor regular molecular structures could be distinguished on the surface, therefore no structural model could be derived. After

annealing the sample to a temperature of $200\,°C$ for $20\,min$ two self-assembly building blocks coexisted (cf. figure 4.30a). Domain sizes of both structures are in the range of ten to one hundred nanometers. An analysis of the rectangular pattern with two-dimensional fast Fourier transformation (as can be seen in figure 4.30b) and structural overlay of molecule schematics resulted in a 2D space group *cmm* [91] and lattice parameters of $d_1 = 1.5\,nm$ and $d_2 = 1.6\,nm$. The unit cells are indicated by white rectangles with yellow outlines. The STM contrast is composed of a bright sphere in the center surrounded by four smaller bright spheres with rotation centers of order two as can be depicted from the STM topography. One white rectangle per unit cell indicates the basic molecular building block of the *cmm* structure.

The same analysis for the second structure gives a rhombitrihexagonal tiling in plane crystallographic group *p6mm* (cf. inset in figure 4.30c). A rhombitrihexagonal tiling requires six elements per unit cell and belongs to the Archimedean tilings [56]. Each unit cell consists of one black hexagon, two green triangles and two white squares. As indicated by the STM topography, only the spots marked by white squares show molecules. In a rhombitrihexagonal tiling each unit cell contains three white squares (one centered plus four half squares: $1 + \frac{1}{2} \cdot 4 = 3$). So each white square can be assigned to one molecular building block, and each unit cell contains three of these basic building blocks. Isolated spherical protrusion with a diameter of $(0.5 \pm 0.05)\,nm$ surrounding the ordered structure can be attributed to bromine atoms through comparison to literature values of $(0.45 \pm 0.05)\,nm$ [17].

Further annealing of the same sample to $320\,°C$ leads to unordered networks, where all molecules appear to be interconnected. No regular protrusions can be discerned and no conclusions can be drawn about intermolecular distances or possible structures.

Deposition and Annealing of TBrTFB on Cu(111)

Cu(111) is known to be a more reactive surface than Ag(111) [15], and accordingly measurements indicate a different reaction pathway on both substrates (cf. figure 4.31). After room temperature deposition of TBrTFB on Cu(111) the surface is mainly covered by a hexagonal structure with lattice parameters of $(0.4 \pm 0.05)\,nm$, as derived by FFT processing of STM topographs (cf. figure 4.31a). Comparing this experimentally obtained lattice parameter with halogen adlayer literature values of $(0.4 \pm 0.05)\,nm$ on Cu(111), one finds a good agreement with densely packed bromine adlayers with a lattice parameter of $(0.42 \pm 0.02)\,nm$ [69]. This finding is also in plausible agreement if one takes the catalytic properties of Cu(111) at room temperature into account. Homolysis of carbon-bromine bonds can be explained by Cu-mediated Ullmann reactions [106, 154], where the cleaved-off bromine atoms adsorb at the surface. The hexagonal structure is surrounded by bright spherical protrusions with diameters of $(0.5-0.8)nm$. Further annealing at $500\,°C$ for $10\,min$ does not lead to full desorption of the halogen adlayer, which is in agreement with thermal desorption experiments on Cu(100), where bromine fully desorbs at temperatures above $730\,°C$ [102]. The previously observed protrusions could not be detected anymore after the harsh treatment (cf. figure 4.31b).
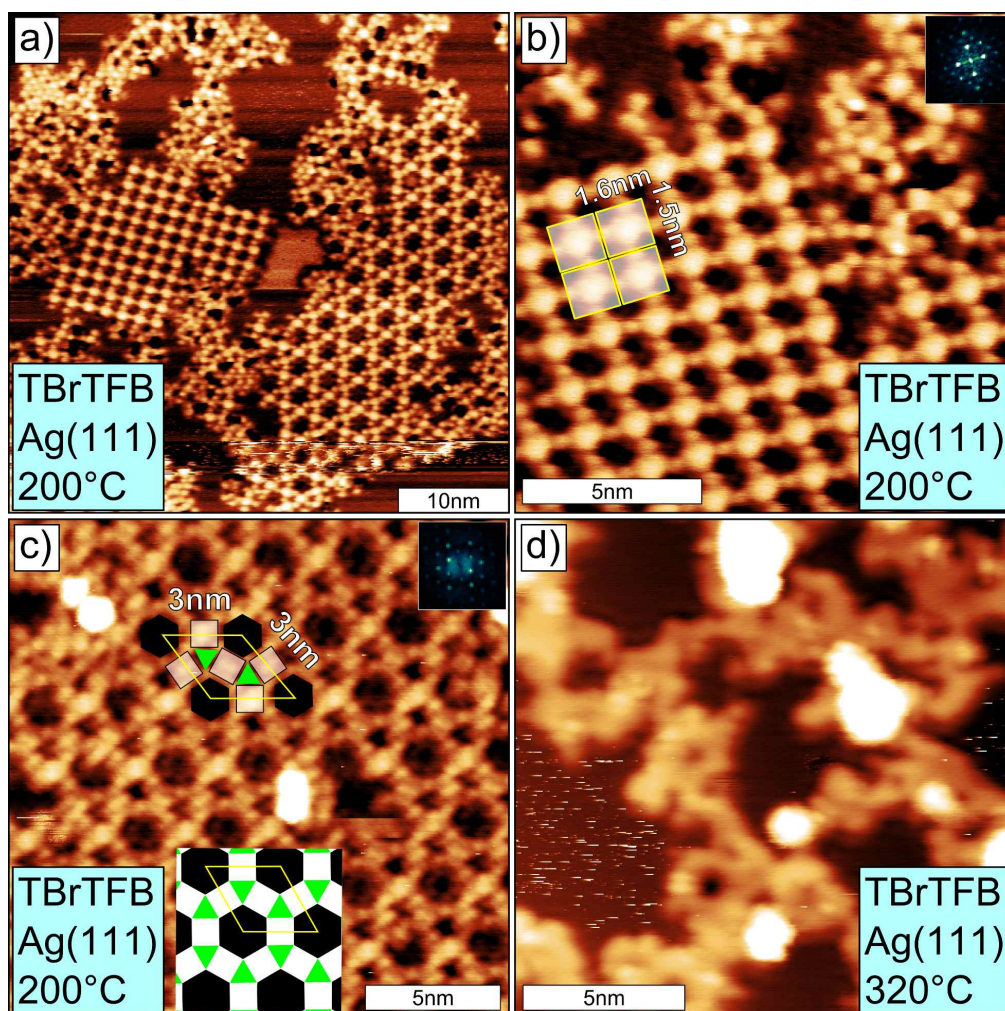
Figure 4.30: STM topographs after annealing of TBrTFB on Ag(111) at 200 °C for 20 min: (a) Large scale overview showing coexistence of two different ordered structures ($V = -0.7$ V and $I = 50$ pA); (b) rectangular structure in plane space group *cmm* and lattice parameters of $d_1 = 1.5$ nm and $d_2 = 1.6$ nm ($V = -0.7$ V and $I = 50$ pA); A rhombitrihexagonal tiling in plane space group *p6mm* with lattice parameters of 3.0 nm can be derived from figure (c). The tiling is visualized in the inset: black hexagons indicate large pores and green triangles indicate small pores between the white squares, which can be assigned to molecular building blocks. Only the white squares correlate with protrusions in the STM topography ($V = 0.4$ V and $I = 40$ pA). (d) Further annealing to 320 °C leads to unordered networks, where all molecules appear to be interconnected ($V = 0.6$ V and $I = 50$ pA).
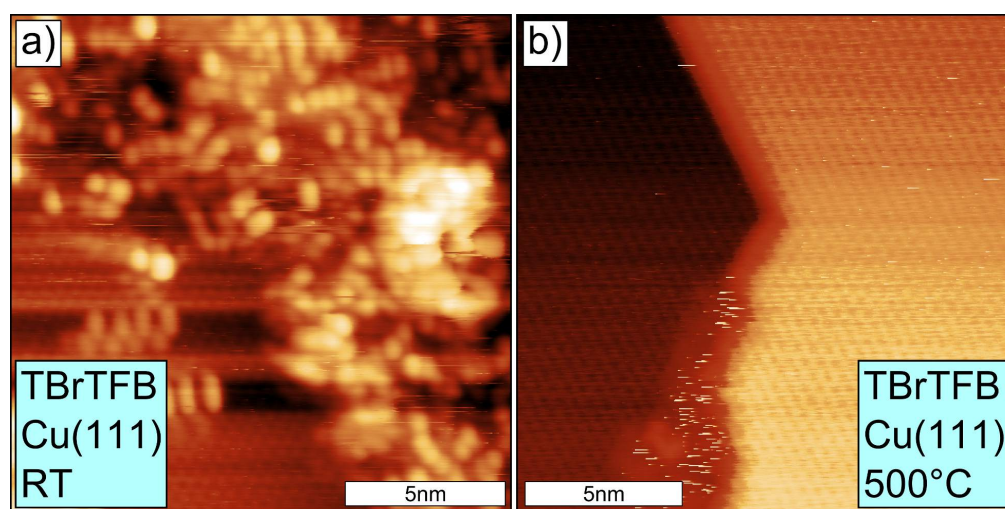
Figure 4.31: STM topographs of (a) RT deposition of TBrTFB molecules: an unordered structure coexists with a hexagonal pattern with a lattice parameters of (0.4 ± 0.05) nm. A literature comparison of the lattice parameters indicates a bromine adlayer ($V = 0.6$ V and $I = 50$ pA). (b) Further annealing up to temperatures of 500 °C for 10 min leads to desorption of all protrusions and to complete coverage of the surface with bromine atoms ($V = -0.7$ V and $I = 50$ pA).

Low Temperature Comparative Deposition Experiments of TBrB on Ag(111) and Cu(111)

In order to assess the influence of the fluorine pendant groups of the TBrTFB building blocks on surface reactivity, deposition experiments are repeated with TBrB molecules. Room temperature deposition of TBrB on both Ag(111) and Cu(111) surfaces for several hours does not show any adsorbed molecules. Therefore deposition experiments were performed with surfaces held at a temperature of 80 K.

STM measurements of TBrB deposition on Ag(111) show adsorbed molecules in a loose arrangement with no long-range order, where single molecules can hardly be discerned. Typical domain sizes are around ~ 100 nm^2 (cf. figure 4.32a).

A different picture arises on Cu(111): The domain areas of ~ 100 nm^2 are comparable to those on the Ag(111) surface, but TBrB molecules arrange in a self-assembled hexagonal lattice with parameters of 1.35 nm as derived from FFT calculations (see inset bottom right corner). An overlay of the hexagonal arrangement is indicated in the inset on the top right corner in figure 4.31b.

Annealing of the sample – even if performed slowly overnight – leads to desorption of the molecules without any further reaction. No additional measurements were carried out at intermediate temperatures between 80 K and RT.

Analysis and Discussion of TBrTFB Structures on Ag(111)

As can be derived from figure 4.30b and 4.30c, both molecular structures are comprised of the same molecular building blocks (as evident from the white rectangular overlays). The deviation of the rectangular building block of figure 4.30b from a squared building
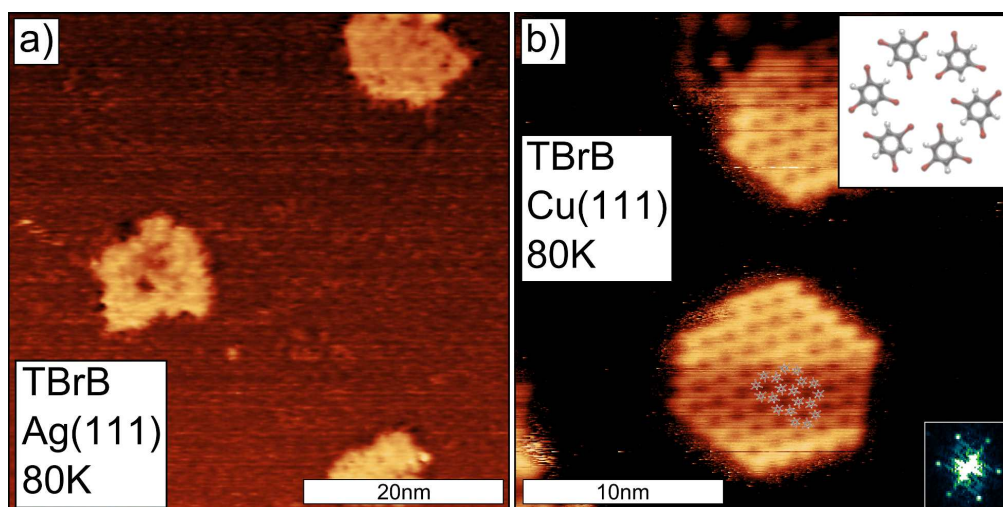
Figure 4.32: STM topographs of TBrB deposition experiments at Ag(111) and Cu(111) surfaces held at temperatures of 80 K: (a) TBrB molecules adsorb on Ag(111) in a loose arrangement with typical domain sizes around $\sim$100 nm^2 ($V = -1.6$ V and $I = 50$ pA). (b) TBrB molecules arrange on Cu(111) in a self-assembled hexagonal lattice with parameters of 1.35 nm as derived from FFT calculations (see inset on bottom right corner). An overlay of the hexagonal arrangement is indicated in the inset on the top right corner ($V = 1.4$ V and $I = 40$ pA).

block of figure 4.30c is below the accuracy of the STM of 5%. Therefore it is justified to assume that different mutual arrangements of the same building blocks lead to the rectangular as well as hexagonal structures. To resolve the molecular nature of the basic building block, conclusions and assumptions can be made from the deposition experiments:

- Both structures are based on the same building block,

- the network is thermally not stable, so a fully cross-linked covalent network is unlikely,

- and the observation of isolated smaller spherical protrusion indicate bromine atoms, so at least a partial homolysis of the C−Br bonds occurs.

A structural model that explains both structures and includes all of the assumptions is the formation of a biphenyl after homolysis of one bromine bond on each TBrTFB. The so formed 3,3',5,5'-tetrabromo-2,2',4,4',6,6'-hexafluoro-1,1'-biphenyl (TeBrHFBP) serves as the molecular building block. Both networks are stabilized by bromine-bromine halogen bonds. Split-off bromine atoms surround the network and can be clearly identified as additional protrusions. Dimerization appears to be self-limiting as no more homolysis reaction occurs after formation of a biphenyl, so the TeBrHFBP seems to be the thermally and kinetically stable end product after annealing to a temperature of 200 °C.

That structural model is presented in overlays in figure 4.33. The stabilizing effect of bromine-bromine interactions is well known and was found in self-assembled layers
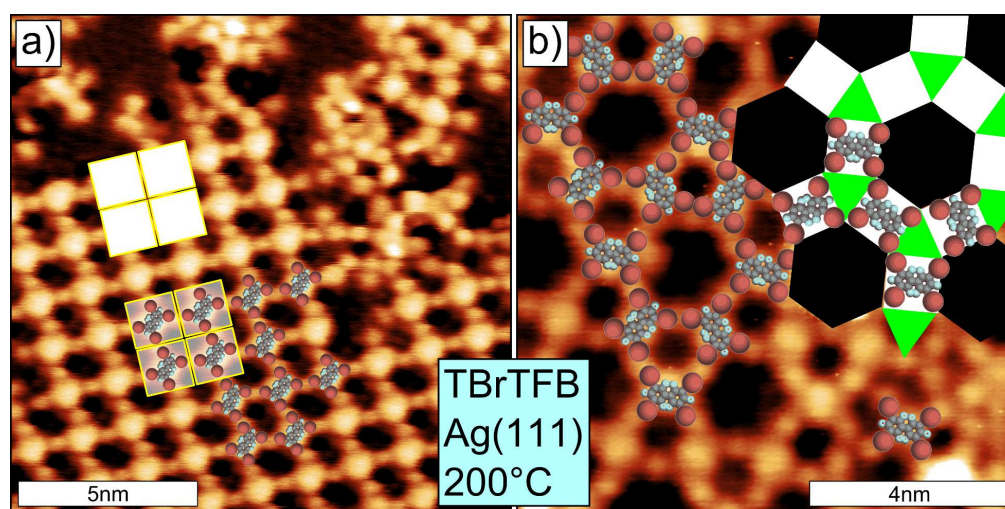
Figure 4.33: STM topographs of TeBrHFBP structures with plane space group *cmm* ($V = -0.7$ V and $I = 50$ pA) (a) and *p6mm* plane space groups ($V = 1.7$ V and $I = 40$ pA) (b). The TeBrHFBP dimers are mapped by the white rectangles. This is the basic building block of both structures. Further explanation is provided in the text.

of tribromobenzene or hexabromobenzene [156, 130]. Moreover, these interactions are also substantiated by theoretical models [20, 121, 89, 124].

Inductive effects: One possible explanation for the self-limiting formation of the biphenyl (TeBrHFBP) is provided by inductive effects. The transmission of charge due to electrostatic effects induced by fluorine atoms is a basic principle in organic chemistry which can explain bond strength [97]. Bond polarization due to the strong electronegative character of fluorine results in a partial negative charge δ^- for each fluorine atom, while each of the carbon atoms of the aromatic system obtains a positive partial charge δ^+. Fluorine is known as one of the strongest electron withdrawing elements ("minus inductive effect") and significantly more electronegative than hydrogen. This could explain the difference in the surface chemistry of TBrB and TBrTFB.

DFT calculations of the C−Br binding energy dependent on the amount of remaining bromine atoms for both TBrB and TBrTFB were performed. In order to deduce the influence of fluorine atoms in comparison to hydrogen atoms, the difference in binding energies for the C−Br bond for both intact molecules and after one, two or three bromine dehalogenations was calculated. If there is a large difference in binding energy (i.e. an increase), one can attribute this difference to the inductive effects of fluorine atoms, thereby explaining the partial dehalogenation and self-limiting dimer formation.

For excluding basis set superposition errors, counterpoise correction of the GAUSSIAN03 code was introduced [47]. A B3LYP functional, 6-31G* basis sets and the maximum possible number of fragments was used for counterpoise correction. In principle, all superposition errors were taken into account, because the number of fragments equals the number of atoms. The results are listed in table 4.1.

Table 4.1: Counterpoise corrected total energies and differences in binding energies between TBrB and TBrTFB molecules for the C−Br bond for different successive debrominations:

Degree of bromine dehalogenation	TBrB total energies in kJ/mol	TBrTFB total energies in kJ/mol	Energy differences in kJ/mol
1. Dehalogenation	326.037	326.725	0.688
3. Dehalogenation	315.145	315.679	0.534

These energy differences in binding energies below $1\,kJ/mol$ are insignificantly small compared to the typical C−Br binding energy in the range of $320\,kJ/mol$ or to temperature induced energy fluctuations of $k_b T = 2.42\,kJ/mol$. They cannot account solely for an explanation of dimerization, so additional effects must influence the reaction process.

Difference in adsorption geometry of monomers and dimers: A possible re-action pathway to the formation of dimers can be postulated by taking different adsorption geometries of monomers and dimers into account.

1. The first bromine dehalogenation takes place right upon adsorption due to catalytic properties of Ag(111).

2. Radical monomers adsorb in an upright position on the substrate analog to the Ullmann-coupling of bromobenzene on Cu(111) [154, 163, 17] (see figure 4.34a).

3. Dimerization to TeBrHFBP takes place when two monomers meet (see figure 4.34b).

4. The dimers adsorb planarly on the surface (see figure 4.34c).

5. Catalytic properties of Ag(111) are not sufficient to further dehalogenate the planarly adsorbed dimers.

The dimers are stabilized on the surface and can self-assemble into the observed structures, but no further debromination takes place.

4.4.4 Conclusion

The influence of pendant groups on interactions of the system hydrogenated vs. fluorinated tribromobenzene on Ag(111) and Cu(111) surfaces was compared. While TBrB just self-assembles at liquid-nitrogen temperatures and desorbs from the surface during warm-up to room temperature, TBrTFB adsorbs at room temperature and self-assembles into ordered structures. Careful analysis of high resolution STM images of ordered structures allows for an assumption for a structural model. Hereby TBrTFB undergoes a homolysis reaction of only one bromine atom and forms TeBrHFBP biphenyls with four remaining bromine atoms. These dimers serve as molecular building blocks for the two observed structures in plane space groups *cmm* and *p6mm*. Both structures coexist on the Ag(111) surface. These dimerization
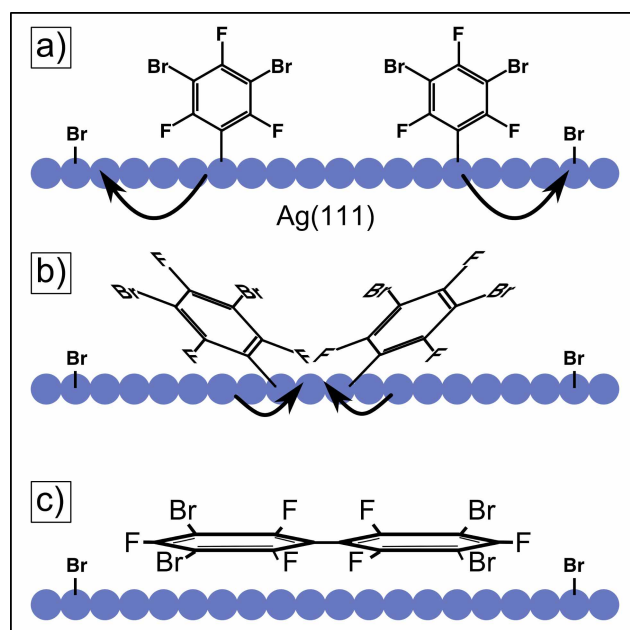
Figure 4.34: Schematic view of the reaction pathway from TBrTFB monomers to dimers. For explanation see enumeration in text.

was explained by an upright adsorption and debromination of the monomer with successive recombination into planar dimers and self-assembly into ordered structures. No further debromination takes place due to unknown reasons. In order to revise the presented model, further adsorption spectroscopy experiments, such as XPS or NEXAFS, are reasonable to gain more insights into binding mechanisms of dimers and self-assembled structures.

4.5 Thermally Induced Dehalogenation of Tribromobenzene prior to Deposition

4.5.1 Introduction

In the present work, molecule reactions in the heatable crucible (see section 4.1) as well as surface-mediated reactions in sections 4.2, 4.3 and 4.4 after deposition of intact molecules were studied. A possible next step to investigate is the deposition of already pre-activated species.

This enhances the options to influence the overall reaction by one more parameter, where pre-activation of molecules induced by a separated device can be externally controlled. Catalytic surface properties are no longer needed to induce the activation of molecules, so adsorption of pre-activated species can be extended to inert surfaces.

In the following work the realization of such a device that activates molecules by cleavage of leaving groups prior to deposition is established. After presenting the experimental details of the proposed device, quadrupole mass spectrometer measurements and deposition experiments of activated tribromobenzene on a graphite(0001) surface were shown. Structure analysis was performed by means of STM.

4.5.2 Experimental Methods

1,3,5-tribromobenzene (TBrB, CAS 626-39-1, purity $> 98\%$, molecular mass $314.80\,\mathrm{u}$) was obtained from Sigma Aldrich GmbH, Germany. TBrB molecules were deposited through a high precision sapphire leak valve equipped with a heatable drift tube (HDT) directly aiming at the sample. Prior to deposition the molecules were thoroughly out-gassed. The HDT device can be heated via a tungsten filament guided inside a ceramic capillary. The whole drift tube can be heated to $600\,^{\circ}\mathrm{C}$, were approximately $50\,\mathrm{W}$ of electric power are needed. A basic schematic drawing is depicted in figure 4.35. The molecules are stored in a heatable crucible reservoir, which is connected to the stainless steel drift tube inside the UHV system. The temperature of the drift tube is measured on the outer surface of the metal tube by a thermocouple. Temperatures inside the tube, especially on the ceramics, are higher.

Mass spectrometer measurements were conducted with the commercially available quadrupole mass spectrometer (QMS) *QMA 430*, Balzers, Liechtenstein. During experiments the drift tube directly aimed towards the mass spectrometer.

All STM experiments were conducted with a home-built beetle type scanning tunneling microscope at room temperature under ultra-high vacuum (UHV) conditions at a base pressure below $3 \times 10^{-10}\,\mathrm{mbar}$. The STM was carefully calibrated and lattice parameters and distances were derived from topographs with an accuracy of $0.05\,\mathrm{nm}$. The cleanliness of graphite(0001) surface after annealing at a temperature of $500\,^{\circ}\mathrm{C}$ was verified by STM imaging prior to deposition.

4.5.3   Results and Discussion

QMS Measurements

To obtain evidence that the HDT induces homolysis, mass spectrometry results of activated TBrB molecules are presented.

The fragmentation scheme in figure 4.36 is used to discuss frequent reaction steps in the homolysis of TBrB. Depending on the reaction pathway, mono-, bi- or triradical aromatic molecules as well as bromine radicals are formed.

Starting with the original molecule with an atomic mass of 315 u, homolysis of one bromine radical leads to a positively charged phenyl ring with two remaining bromine atoms and a mass of 233 u. Further dehalogenation and removal of either a bromine radical or a HBr molecule results in aromatic molecules with 154 u or 153 u, respectively. The last homolysis step cleaves all bromine atoms and mono-, bi- or triradical aromatic molecule in the range of $(73-75)$u are produced (see tabular 4.2). Five groups of fragments can be detected in the QMS spectrum in figure 4.37.

Each group consists of several peaks due to the isotope distribution. For discussions the isotope distribution is neglected and only weighted average isotope masses are used. Split-off bromine atoms around 80 u can be distinguished in the spectrum [160]. More fragments of the TBrB molecule can be observed at other mass values.

In addition to the homolysis abilities of the HDT setup, a quadrupole mass spectrometer (QMS) is also capable to break bonds. So one has to distinguish the two effects from each other: homolysis by the HDT (HDT type fragments) and bond breaking through electron impact ionization by the QMS (QMS type fragments) [120]. QMS type fragments can be detected with higher efficiency due to the ionization of
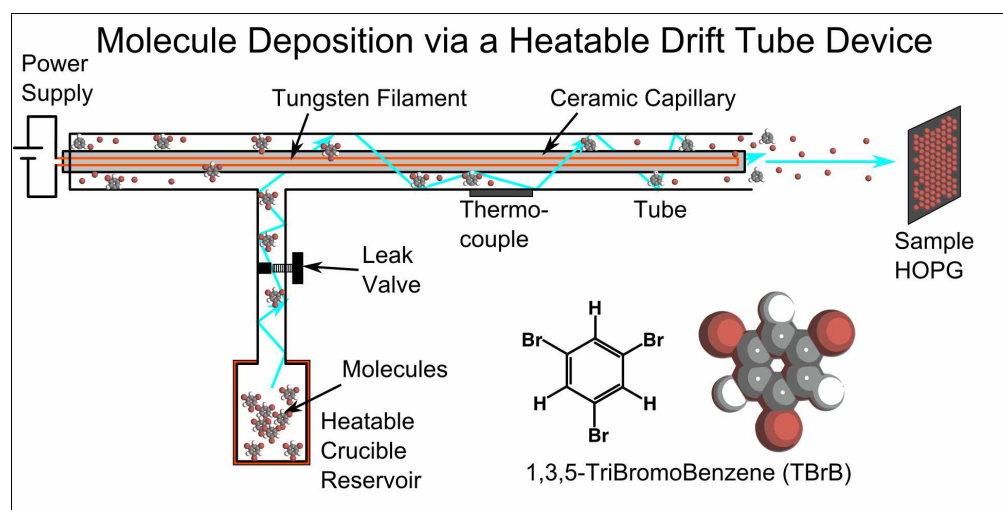
Figure 4.35: Schematic illustration of the heatable drift tube device: molecules are stored behind a high precision sapphire leak valve in a heatable crucible reservoir and dosed into a drift tube. This stainless steel tube can be heated through an internal tungsten filament and directs the molecules towards the surface. Multiple collisions with the tube wall thermally activate the TBrB molecules by homolysis of the C-Br bond and lead to bromine and phenyl radicals.
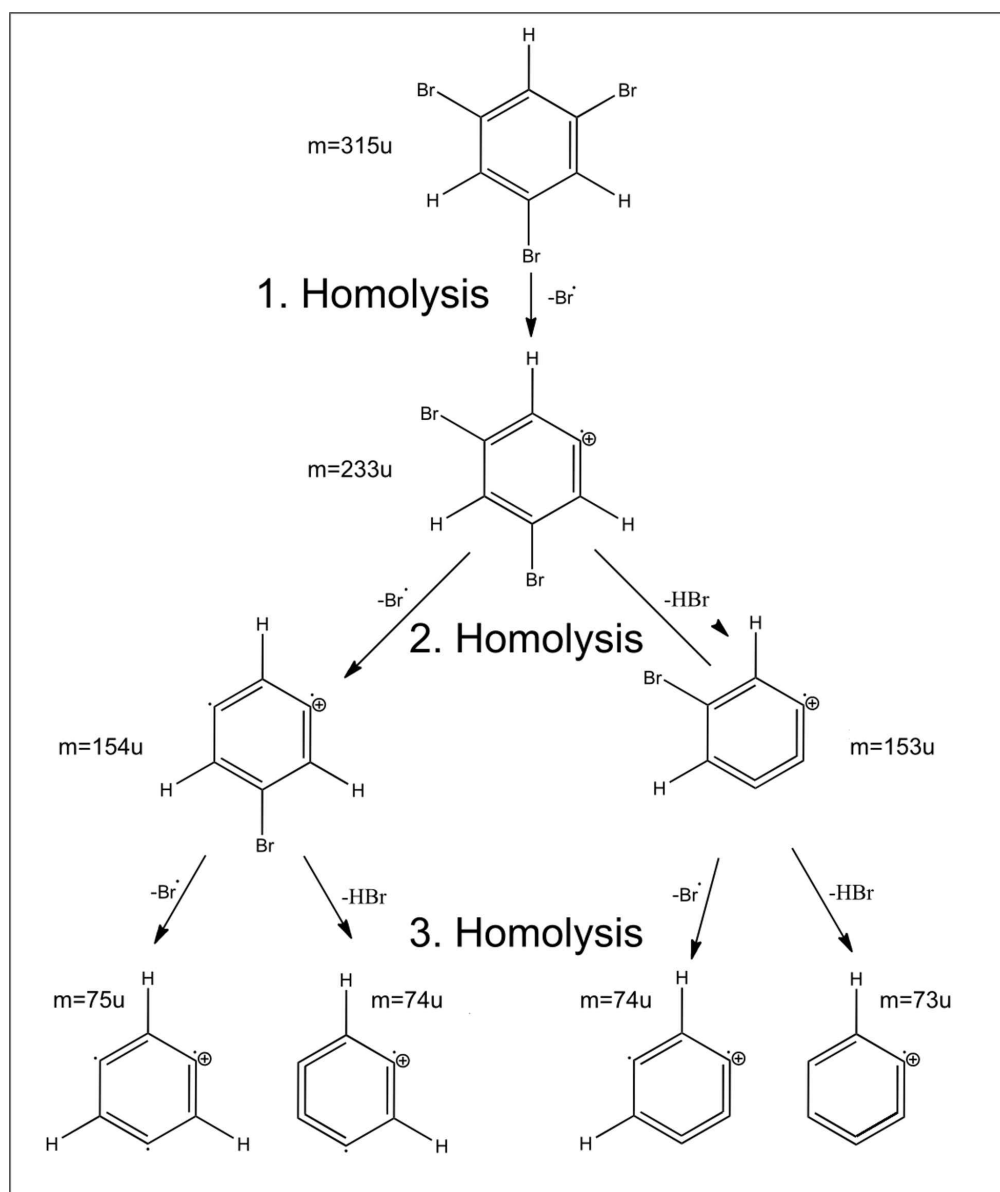
Figure 4.36: Fragmentation scheme for possible homolysis reaction pathways for TBrB: intact molecule around 315 u; homolysis of one C−Br bond gives phenyl radicals with masses around 233 u. Further dehalogenation and removal of either a bromine radical or a HBr molecule results in phenyl rings with one bromine atom and masses of 154 u or 153 u, respectively. After the third homolysis, molecules have masses in the range $(73 - 75)$u. Other reaction pathways are less frequent and neglected.

Table 4.2: Weighted average isotope masses of the elements and attribution to detected fragments:

Atomic mass	Description
1 u	Hydrogen
12 u	Carbon
80 u	Bromine atom (each 50% ^{79}Br and ^{81}Br)
315 u	Intact molecule: $C_6H_3Br_3$
233 u	Minus one bromine atom: $C_6H_3Br_2$
154 u	Minus two bromine atoms: $C_6H_3Br\cdot$
153 u	Minus two bromine atoms: $C_6H_2Br\cdot$
75 u	Benzene triradical $C_6H_3\cdot$
74 u	Benzene biradical $C_6H_2\cdot$
73 u	Benzene monoradical $C_6H\cdot$

fragments inside the QMS device. HDT type fragments are activated by the drift tube, so probably only a smaller fraction of these fragments is directed towards the QMS and detected.

Homolysis capabilities of the HDT are clearly indicated in the QMS spectrum (see figure 4.37). Seven different spectra are plotted, each for a specific HDT temperature between room temperature and 600 °C. On the x-axis the atomic mass in units of u is given, while on the y-axis the normalized signal is drawn in arbitrary units. In the temperature range of $(500-600)$°C one can clearly see an absence of signal at atomic masses above 50 u. This can be explained by the C−Br bond homolysis abilities of the HDT, where TBrB is activated by the HDT. Only a small fraction of the fragments is detected by the QMS. At lower temperatures fully intact molecules are directed into the QMS and undergo the electron impact induced fragmentation with detectable peaks as depicted in table 4.2.

If the HDT is deactivated, QMS type fragments are detected after all homolysis steps and dehalogenation of up to three bromine atoms takes place in the QMS. Above a certain threshold temperature, full homolysis takes place inside the drift tube and only HDT type fragments with smaller atomic masses are detected by the QMS.

More detailed temperature dependent QMS measurements narrow the drift tube induced homolysis threshold to temperatures around $(430-440)$°C. In order to guarantee a full homolysis for deposition experiments, a temperature of 600 °C well above the threshold was set to the drift tube.

Based on the QMS results, it is suggested that the homolysis takes place prior to deposition of the molecules onto the surface. There is no detailed insight into the mechanism of the homolysis. Possibly the molecules adsorb at the hot drift tube, become vibrationally excited thereby overcoming the energy barrier for breaking of the C−Br bonds. It is reported by Levinger et al. that energy transfer of a vibrationally excited backbone stretch mode into a functional group bond stretch is responsible for H-bond breaking, yet there is some controversial discussion about the exact mechanism with deviating relaxation pathways [83]. Catalytic support by the
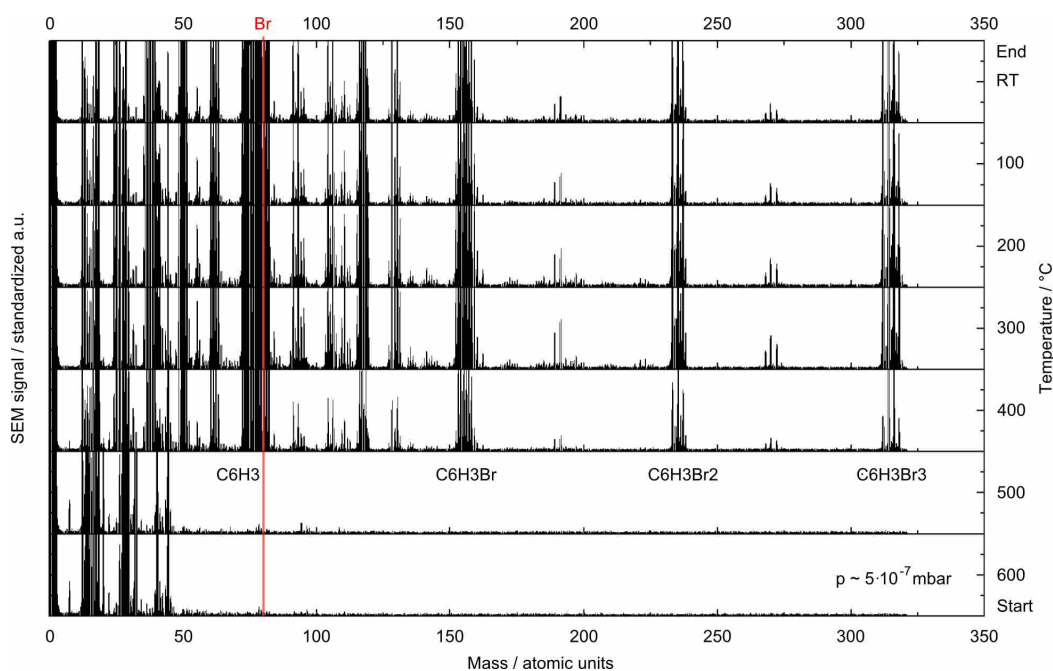
Figure 4.37: Temperature dependent QMS measurement with higher resolution: Seven different spectra, each for a specific HDT temperature between room temperature and 600 °C, are plotted with an offset. On the x-axis the atomic mass in units of u is given, while on the y-axis the standardized signal in arbitrary units is presented. *Matthias Lischka is acknowledged for the measurement.*

Fe atoms of the stainless steel alloy are also possible, albeit somehow speculative. At such elevated temperatures above 600 °C the Boltzmann distribution allows for very high molecule energies. This should further increase the kinetics and enable bond breaking.

STM Measurements

In order to show the possibilities of the homolysis prior to deposition, a bromine adlayer is prepared on HOPG in UHV. Until now no measurements of halogen adlayers on HOPG were reported in the literature. TBrB deposition via the deactivated HDT device did not result in adsorption of any species on the graphite(0001) surface. Further experiments were conducted at drift tube temperatures of 600 °C, as concluded from the QMS measurements. After deposition of the TBrB molecules via enabled HDT, the STM topograph (figure 4.38) depicts a hexagonal adlayer with 2D space group $p6mm$ and lattice parameters of (0.42 ± 0.05) nm. Moreover a periodic modulation with a hexagonal superstructure (also $p6mm$) with lattice parameters of (2.58 ± 0.05) nm can be observed. A literature comparison of the adlayer periodicity indicates a bromine adlayer, although literature values are only available for metallic surfaces and lie in the range of $(0.40 - 0.50)$ nm depending on the adlayer coverage [69, 11, 12, 73, 102]. The adsorption of atomic bromine on HOPG proves the capability of the HDT device.

In figure 4.38a one can see a full coverage of the surface with a bromine adlayer.
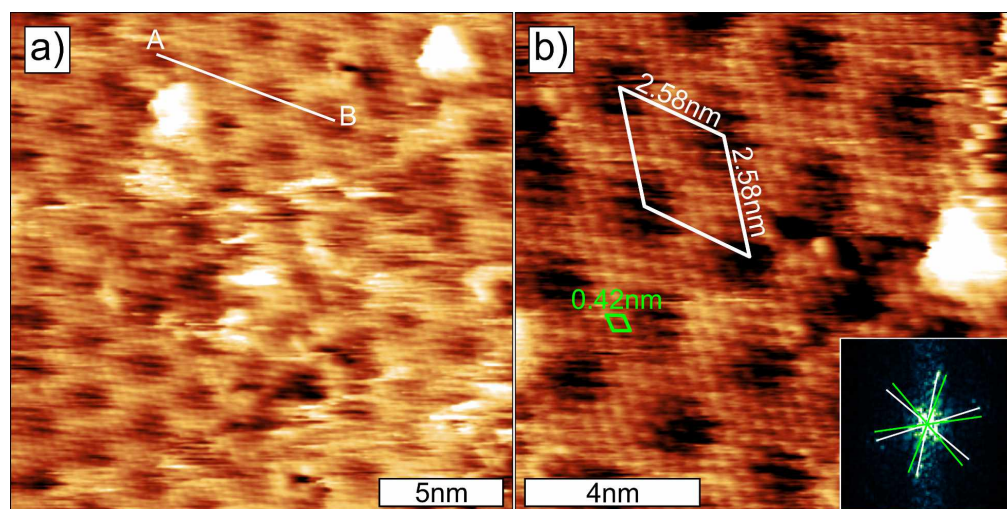
Figure 4.38: STM topographs of a hexagonal bromine adlayer on HOPG: (a) corrugation along the line $A - B$ is about $150\,\mathrm{pm}$ ($V = -0.54\,\mathrm{V}$ and $I = 40\,\mathrm{pA}$); (b)close-up of (a). FFT (see inset) of the hexagonal lattice yields a smaller hexagonal unit cell of $(0.42 \pm 0.05)\,\mathrm{nm}$ (green unit cell) and a larger superstructure of $(2.58 \pm 0.05)\,\mathrm{nm}$ (white unit cell). The angular mismatch between the two unit cells is about $(9.7 \pm 1.0)\,^\circ$. ($V = -0.54\,\mathrm{V}$ and $I = 40\,\mathrm{pA}$)

The corrugation of the hexagonal superstructure (about $150\,\mathrm{pm}$) is about five times larger than the corrugation of the bromine atoms (about $30\,\mathrm{pm}$), which is typical for Moirè patterns of adlayers.

Moirè superstructures were observed in the STM already several years ago. For instance rotated graphite flakes on graphite(0001) surface lead to Moirè superstructures [126, 162]. Also self-assembled monolayers of fatty acids with long alkane chains formed a Moirè superstructure on HOPG [123]. Silly et al. describe the electronic influence of graphite(0001) substrate on the 1-octanol molecules that cause a Moirè pattern [140]. A common feature of all experiments is the weak interaction of molecules with HOPG, enabling Moirè superstructures.

A direct measurement of angles within the FFT of figure 4.38(b) gives an angle of $(9.5 \pm 1.0)\,^\circ$ between the Moirè pattern and the halogen adlayer. Because it was not possible to directly derive the arrangement of the bromine adlayer on HOPG, an indirect analysis is performed.

For a further determination of the bromine adlayer arrangement on top of the HOPG surface, one can use the Moirè superstructure periodicity. The schematic arrangement of the Moirè pattern in figure 4.39 allows for derivation of the angle between the bromine adlayer and HOPG lattice arrangements. Structural parameters comparable to experimentally derived values of the bromine adlayer and HOPG are used for the schematic arrangement. The two lattices are rotated until a relative orientation of $\angle (\mathrm{Moire/Br}) = 9.5\,^\circ$ between the bromine adlayer and the Moirè superstructure occurs. Now, the angle between Br adlayer and HOPG is about $\angle (\mathrm{HOPG/Br}) \approx 25\,^\circ$. Calibration of the schematic lattices gives the same structural parameters for the Moirè pattern of $2.58\,\mathrm{nm}$ as could be derived experimentally.

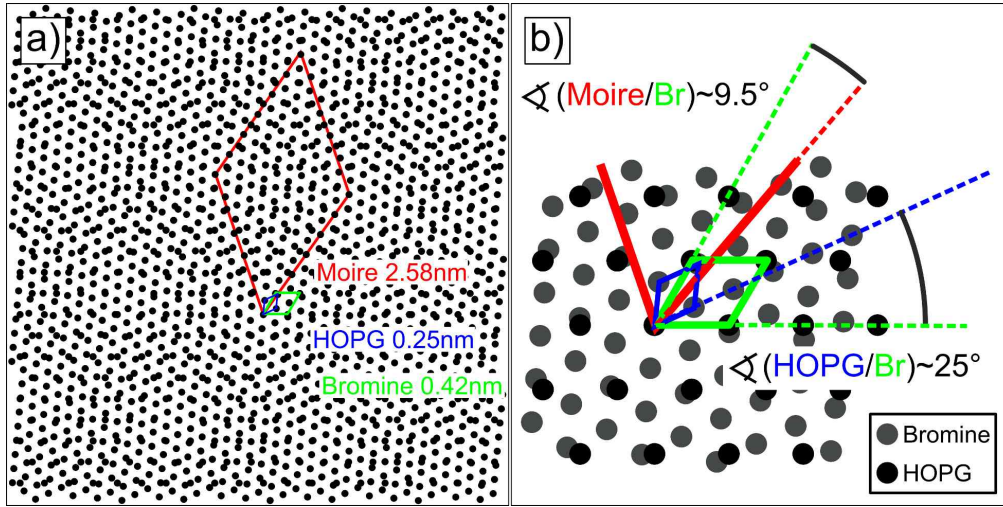Comparing the lattice constants of the bromine adlayer and the (0001) surface of

Figure 4.39: Schematic view of the Moirè pattern of a bromine adlayer on HOPG. The model is based on distances and angles as derived from the STM measurements. Two rotated hexagonal pattern with different lattice parameters lead to a Moirè superstructure (a). An indirect analysis to determine the angle between the bromine adlayer and HOPG orientation is used (b). The two hexagonal patterns were rotated to match the periodicity of the Moirè pattern with the experimental finding. An angle between the two lattices with the same periodicities like the Br adlayer and HOPG was derived to $\measuredangle\,(\mathrm{HOPG/Br}) \approx 25\,°$.

graphite in STM topographies [149, 7], one finds a ratio of

$$\frac{0.42\,\mathrm{nm}}{0.246\,\mathrm{nm}} = 1.71 \tag{4.1}$$

which is in the range $\sqrt{3} = 1.73$. Combining this with the periodicity of the Moirè pattern and the angle between Br adlayer and HOPG gives a bromine superstructure on graphite(0001) of $(1.71 \times 1.71)\,R25\,°$. Due to the strong interaction of bromine atoms on metal surfaces like Cu(111) $\left(\sqrt{3} \times \sqrt{3}\right) R30\,°$ is the preferred superstructure for low coverages as found by Jones et al. [73] or Inukai et al. [69]. For such commensurate superstructures no Moirè pattern is observable. The slight deviation of $5\,°$ from the typical value for hexagonal lattices on metal surfaces leads to the Moirè superstructure on HOPG. The two unit cells of graphite(0001) and bromine can be found in figure 4.39: The green bromine unit cell has a 1.71 times larger lattice parameter than the blue graphite unit cell. The two lattices were rotated by an angle of $25\,°$ with respect to each other. This rotation leads to the Moirè superstructure as indicated by the red unit cell with lattice parameters comparable to the experimental findings.

A coexistence of four different Moirè superstructures could be observed at step edges (see figure 4.40), giving further evidence for weak interactions of bromine on HOPG. By comparing these lattices with the presented schematic model, one finds additional rotation angles of certain domains between HOPG and bromine in the range of $(11.0 - 24.5)\,°$. Superstructure lattice parameters for all experimentally derived Moirè periodicities are shown in table 4.3.
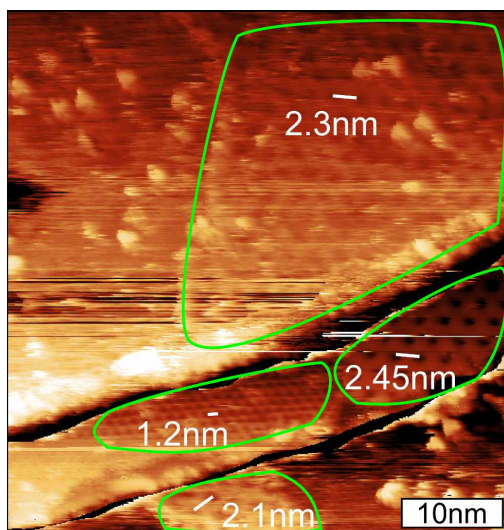
Figure 4.40: STM topograph of several coexisting domains of Moirè superstructures on HOPG near step edges (indicated by green circles). The superstructure periodicities vary between 1.2 nm and 2.45 nm (see exact values in the image). This corresponds to angles between the HOPG and bromine adlayer of $(11.0 \pm 1.0)\,°$ to $(24.5 \pm 1.0)\,°$ (see table 4.3). ($V = -0.61$ V and $I = 45$ pA. The color code for each terrace was individually adapted to increase contrast.

Table 4.3: Moirè periodicities and corresponding superstructures of the Br adlayer on HOPG:

Moirè periodicity	$\measuredangle$ (HOPG/Br)	Superstructure
1.20 nm	11.0 °	$(1.71 \times 1.71)\,R11\,°$
2.10 nm	23.5 °	$(1.71 \times 1.71)\,R23.5\,°$
2.30 nm	24.0 °	$(1.71 \times 1.71)\,R24.0\,°$
2.45 nm	24.5 °	$(1.71 \times 1.71)\,R24.5\,°$
2.58 nm	25.0 °	$(1.71 \times 1.71)\,R25.0\,°$

4.5.4 Conclusion

In this work a device for homolysis of halogen atoms *en route* prior to deposition in a heatable drift tube was presented. The proof of principle was provided by temperature dependent QMS spectra. Furthermore this novel preparation procedure was used to generate a bromine adlayer on graphite(0001) surface in UHV. The homolysis of the carbon-bromine bond takes place at elevated temperatures of the heatable drift tube of more than 600 °C. The split-off bromine atoms are deposited onto the surface, where an atomic physisorption takes place.

Different hexagonal Moirè patterns were evaluated from STM topographies and assigned to a bromine adlayer on top of the graphite(0001) surface. Superstructure periodicities were derived from a schematic model, where the rotation angle between bromine and graphite was altered in order to match the lattice constants of experimentally deduced Moirè patterns. As already discussed above, the Moirè patterns indicate weak interactions between bromine and HOPG and can therefore be seen as characteristic features of the graphite surface, since such effects have not been

observed on metal surfaces yet.

4.5.5 Acknowledgments

4.6 Structural and Electronic Properties of Polycyclooctate-traene

4.6.1 Introduction

A new two-dimensional polymer is proposed with consideration of one major require-ment only: the polymer has to be fully conjugated. As depicted in figure 4.41b, the proposed polymer consists of polycyclic aromatic hydrocarbons with eight delocalized electrons per unit cell and exclusively alternating single and double bonds. The polymer is expected to show an aromatic behavior with a binding energy gain through delocalization although the number of electrons per unit cell does not fulfill Hückel's rule ($8 \neq 4 \cdot n + 2$ for integer numbers n). But because of polycyclic properties, the requirements for Hückel's rule are not fulfilled anyways [125, 97].

The polymer has a quadratic unit cell containing eight atoms and a truncated square tiling with 2D space group *p4mm*. Each atom has three nearest neighbors. The polymer is named *polycyclooctatetraene* (PCOT), because it consists of eight carbon atoms and four double bonds per unit cell and is in a cyclic arrangement.

Distances between next neighbor atoms are 146 pm and 136 pm, respectively (see figure 4.41b). These values lie in the range of typical interatomic distances for an ethane C−C single bond of 154 pm and ethene C=C double bonds of 134 pm, expressing the conjugated properties with effective "one-and-a-half" bonds. The regular arrangement of the atoms is indicated by internal angles of the octagons of 135 ° and internal angles of 90 ° for the tetragons.

Interatomic distances are comparable to that of polyphenylene with C−C bonds between $(139 - 146)$ pm, nevertheless polyphenylen has some angular mismatches of (120 ± 3) ° and is not composed of regular hexagons.

4.6.2 Reversal Engineering

For the synthesis of the polymer appropriate molecular building blocks have to be found. Basic units of the PCOT polymer are either carbon octagons or tetragons. For an on-surface activation of monomers, one needs suitable functional groups. Bromine can be easily cleaved off by catalytic properties of Ag(111) or Cu(111) surfaces. So possible molecular building blocks are tetrabromocyclobutadien (TBCB) (cf. figure 4.42(a)) and octobromocyclooctatetraene (OBCOT) (cf. figure 4.42(b)). Forcefield geometry optimizations yield a planar structure of TBCB with C−C distances of 139 pm and angles of 90 °. OBCOT shows a conformational behavior similar to cyclobenzene [104] and is comprised of a chair-like conformation with C−C distances of 140 pm and solid angles of 125 ° due to the non-planarity. Possibly more conformations exist, but only the most stable conformation with the lowest total energy was calculated. Because TBCB is only stable at low temperatures, the only suitable candidate for the molecular building block is OBCOT. A possible reaction pathway to OBCOT with hexabromo-cyclobutene and octabromo-tricyclo-octadiene as intermediate products was published by Criegee et al. [36]. Deposition of the
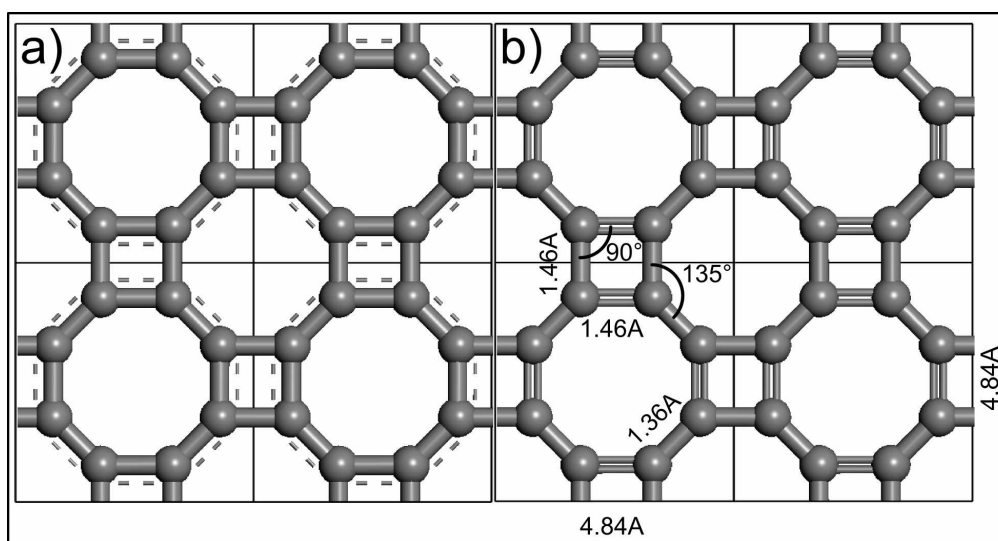
Figure 4.41: Schematic view of the PCOT Polymer: Four quadratic unit cells of PCOT with full electron conjugation and delocalized electrons are shown in a. PCOT is illustrated with alternating single and double bonds in figure b. Furthermore, interatomic distances, angles and lattice parameters are indicated.
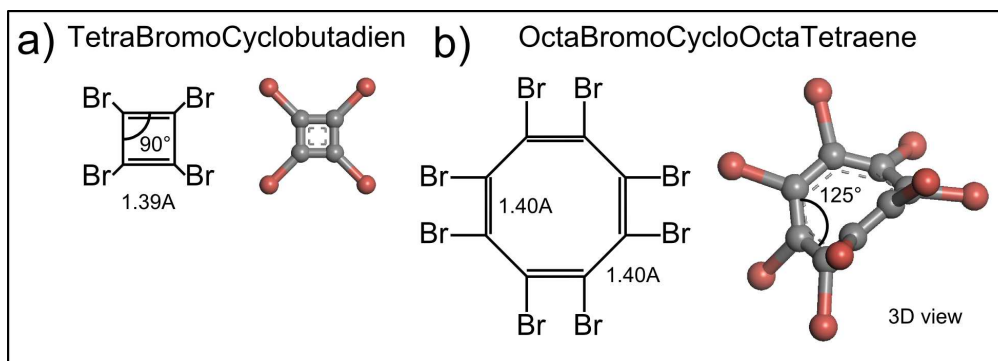

Figure 4.42: Possible molecular building blocks for the synthesis of PCOT polymer.

molecule in an UHV chamber via evaporation onto Ag(111) or Cu(111) at low temperature should hamper the dehalogenation process. Further thermal activation induces and mediates polymerization. After dehalogenation an annulation of the aromatic hydrocarbon backbone is expected.

Room temperature deposition of the molecule on Cu(111) should result in on-surface activation and cleavage of the bromine atoms through Ullmann coupling [154, 17]. A halogen adlayer is expected, possibly hampering the network growth of the carbon octagons.

4.6.3   DFT Results

First-principle total energy calculations of free standing layers of PCOT polymer with unit cells consisting of eight carbon atoms in an octagonal arrangement were performed. In order to optimize the geometry, total energy calculations were repeated

as a function of constrained lattice parameters. The minimum of the parabolic total energy curve has the energetically most favorable structural parameters with a lattice constant of $d = 0.484\,\text{nm}$ (see figure 4.43).

All DFT calculations were performed with the CASTEP code [137] and the superlattice approach. Local density approximation with PW91 [113] functional and plane-wave basis set was used. Convergence criteria were set to $1 \times 10^{-5}\,\text{eV}$ and unit cells in 2D space group *p4mm* were used. Single layers were separated by two nanometers, so no interaction between layers occurred.

The related band structure of the PCOT polymer from electron energies between $-20\,\text{eV}$ and $10\,\text{eV}$ is shown in figure 4.44a. A magnification around the Fermi energy is depicted in figure 4.44b. Dispersion relations were calculated along the k-vectors of the first quadratic 2D Brillouin zone ($\Gamma = [0, 0, 0]$, F$= \left[0, \frac{b^*}{2}, 0\right]$ and M$= \left[\frac{a^*}{2}, \frac{b^*}{2}, 0\right]$) [60]. The band structure shows a direct band gap with energies below $0.1\,\text{eV}$. Although the k-point resolution of the CASTEP code was set to the maximum (19 k-points), additional calculations are required to increase the resolution of the band structure to gain reliable insights into electronic properties. Nevertheless, it can be proposed that PCOT is a low energy direct band gap semiconductor.

The full conjugation of the aromatic system should lead to a high dispersion, since the effective electron mass is inversely proportional to the band curvature. Delocalized electrons have small effective electron masses and therefore high electron mobilities. The total electron isosurface is depicted in figure 4.45.

4.6.4 Conclusion

PCOT is a promising candidate for a new polymer with interesting physical properties like high electron mobility and low band gap energies. A possible reaction pathway via dehalogenation from octobromocyclooctatetraene and annulation of activated carbon rings to polymerization of two-dimensional networks was shown. Physical and electronic properties like structural parameters and dispersion relations of the two-dimensional polymer were derived with DFT calculations. The geometry optimized polymer has a truncated square tiling with 2D space group *p4mm* and lattice parameters of $d = 0.484\,\text{nm}$.
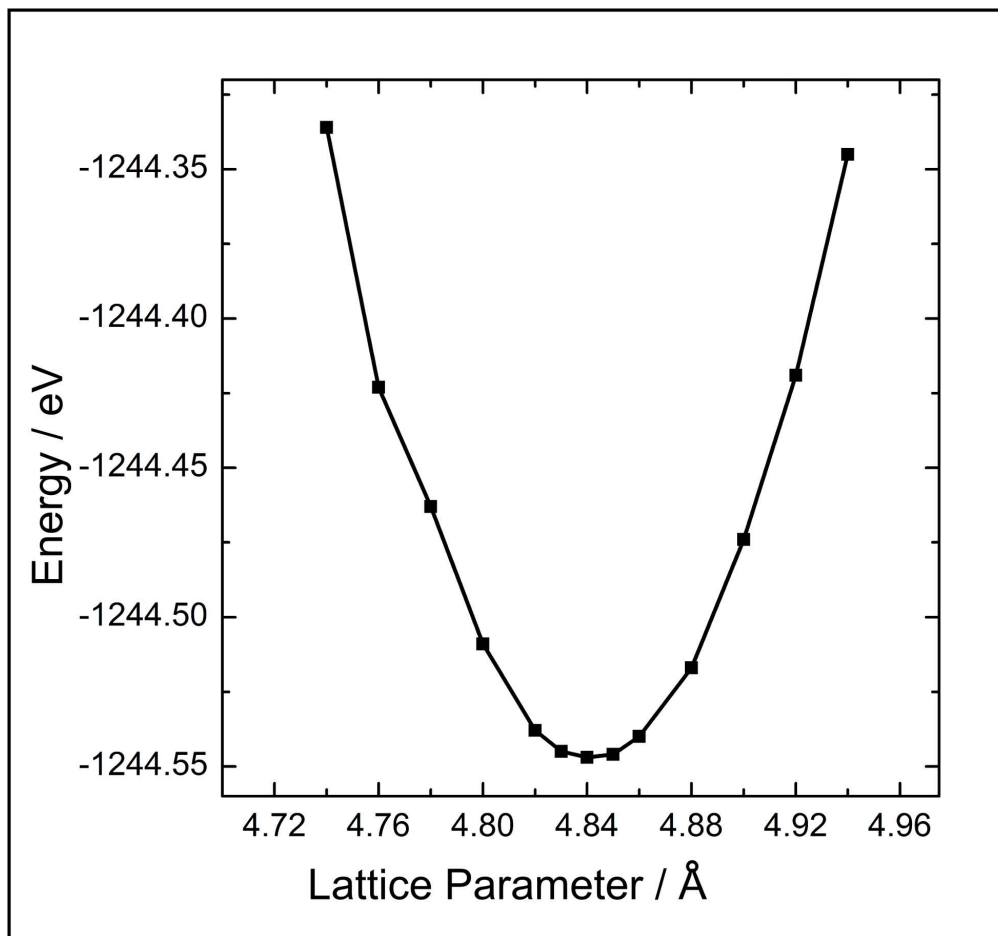
Figure 4.43: Total energy calculations for quadratic PCOT unit cells as a function of lattice parameters is shown. The minimum energy of the parabolic function indicates a most favorable lattice parameter of $d = 0.484$ nm.
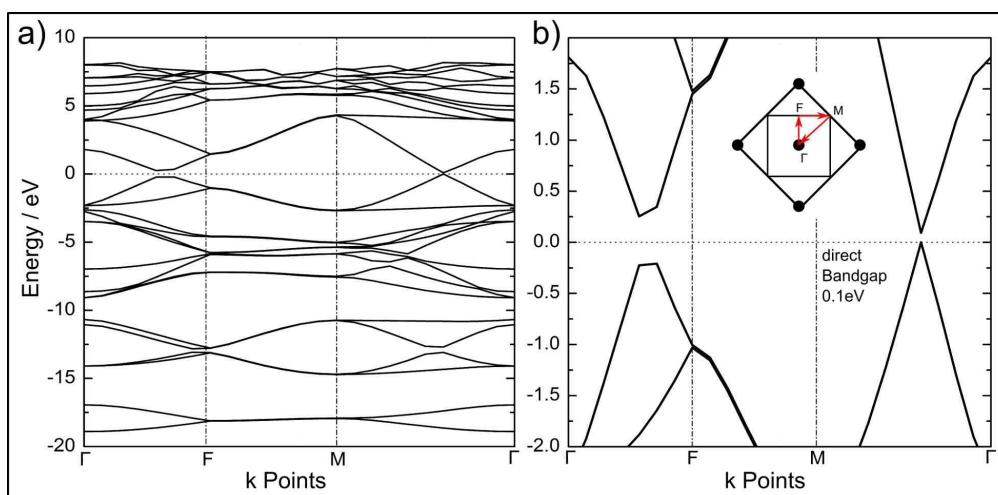

Figure 4.44: Dispersion relation for the PCOT polymer. The band structure from electron energies between -20 eV and 10 eV is shown in a) and a magnification around the Fermi energy is shown in b). PCOT has a direct band gap of ≈ 0.1 eV. The dispersion directions in k-space can be discerned from the inset in b).
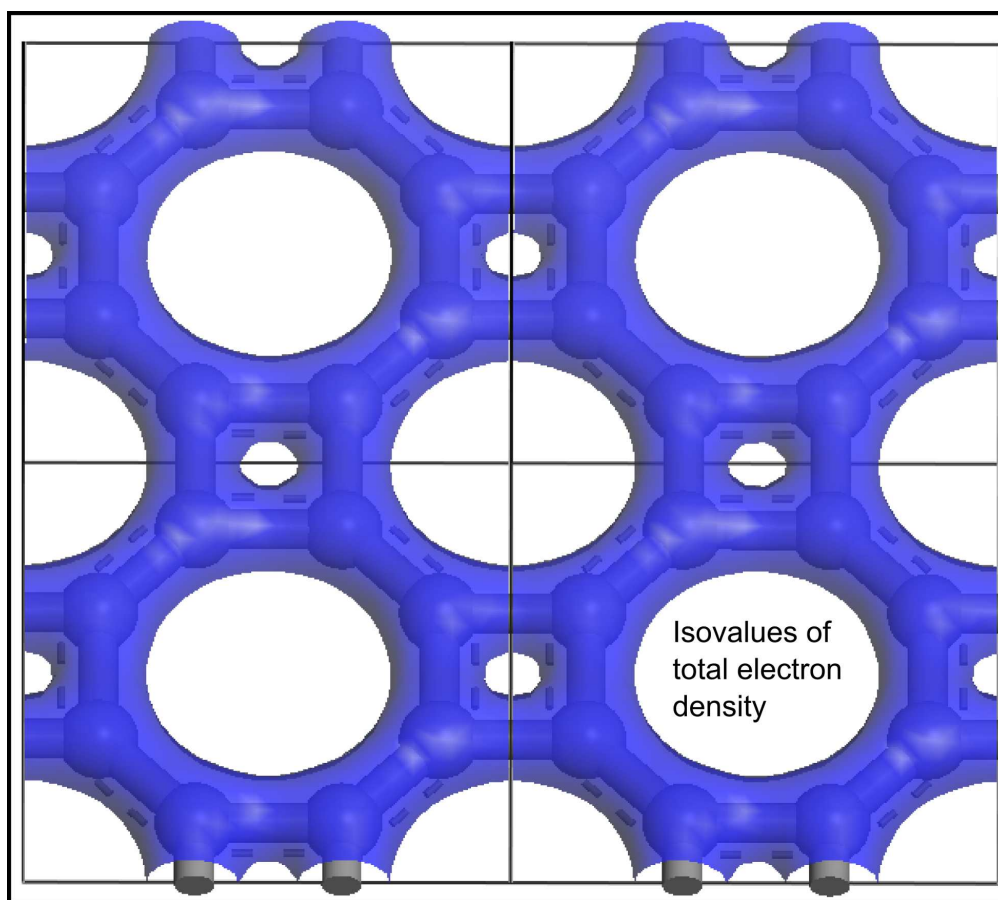
Figure 4.45: The total electron isosurface was visualized. A homogeneous electron distribution can be discerned.

Chapter 5

Conclusion

In the work presented, the synthesis of two-dimensional polymers was systematically studied. Preparation of the molecular layers and two-dimensional polymers was realized inside an ultra-high vacuum chamber on single crystal metal and graphite surfaces. The characterization of reaction products was performed by means of a scanning tunneling microscope, quadrupole mass spectrometer and a low energy electron diffraction device. Moreover, theoretical insights into two-dimensional polymers were gained by density functional theory calculations.

The main chapter consists of six different concepts for the synthesis, while each section focused on different reaction parameters. Possible limitations of reaction pathways were shown and solutions to overcome these problems were proposed. An attempt was made to classify these different reaction processes (see scheme 5.1). Following main conclusions can be drawn from the performed experiments:

- On the one hand, chemical reactions of molecules in the crucible at elevated temperature limit thermal evaporation. These reactions can be controlled and used for in-crucible synthesis of more complex molecules prior to deposition on the other hand. In section 4.1, an in-crucible condensation reaction from 3,5-dibromophenylboronic acid to 1,3,5-tris(3',5'-dibromophenyl)-boroxine is described. Subsequent deposition onto a Ag(111) surface and thermal annealing of this molecules leads to two-dimensional polymers.

- Deposition and thermal activation of 1,3,5-triiodobenzene and 1,3,5-tris(4'-iodophenyl)benzene on a Au(111) surface leads to dehalogenation of the molecular backbone. The split-off iodine atoms can cover a large portion of the surface, and thus hamper the polymerization. This negative influence is more pronounced for the smaller triiodobenzene, where three iodine atoms are split-off from each benzene ring. Compared to that, dehalogenation of the larger tris(iodophenyl)benzene yields three iodine atoms per four phenyl rings. This leads to less limitation of the network growth. On the other hand, defect densities of the resulting oligomers and polymers are smaller for the benzene backbone compared to the larger (triphenyl)benzene backbone. This influence of monomer size is rationalized by different energy deviations of defect forma-

tion energies for both resulting oligomers (see section 4.2). A careful analysis of different molecular building blocks is inevitable to minimize hampering of defect-free two-dimensional polymer growth.

- Another example for the influence of the polymerization process by an halogen adlayer was shown by deposition and annealing experiments of tetraiodotetrathiafulvalene on Au(111) surface (see section 4.3). One-dimensional chain-like structures are polymerized from building blocks with a topology suitable for two-dimensional networks. The dendritic chains are surrounded by an iodine adlayer formed by on-surface homolysis of the iodine functional groups. It is noteworthy that molecules with four equal reactive sites only create one-dimensional chains with branches instead of two-dimensional networks. Different explanations like partial homolysis of the TITTF molecule or partial polymerization of the fully dehalogenated TTF radicals were proposed to address these concerns.

- Substitution of the pendant groups can be used to influence the network topology and reaction pathway (see section 4.4). Reactions of hydrogenated vs. fluorinated tribromobenzene on Ag(111) and Cu(111) surfaces were compared. While tribromobenzene self-assembles at liquid nitrogen temperatures and desorbs from the surface during warm-up to room temperature, tribromotrifluorobenzene adsorbs and is stable up to 320 °C. This stability was explained by an upright adsorption and debromination of the monomer with successive recombination into planar dimers. A self-assembly of dimers into ordered structures on the Ag(111) surface was observed by means of STM measurements.

- In section 4.5 a device for homolysis of the carbon-bromine bond in 1,3,5-tribromobenzene *en route* in a heatable drift tube before their deposition onto graphite(0001) was presented. This novel preparation procedure was used to generate a bromine adlayer on an inert graphite(0001) surface in UHV. The atomic physisorption of the bromine adlayer leads to different hexagonal Moirè patterns, which were classified and described by a schematic model.

- A promising candidate for a new polymer with interesting physical properties like high electron mobility and low band gap energies was proposed in section 4.6. A possible reaction pathway via dehalogenation from suitable monomers to polymerization of two-dimensional networks was shown. Physical and electronic properties like structural parameters and dispersion relations of the two-dimensional polymer were derived with DFT calculations.

The presented insights enhance the knowledge of surface-mediated polymer synthesis and provide approaches to ultimately synthesize long-range ordered, stable two-dimensional polymers with desired physical and chemical properties in the future.
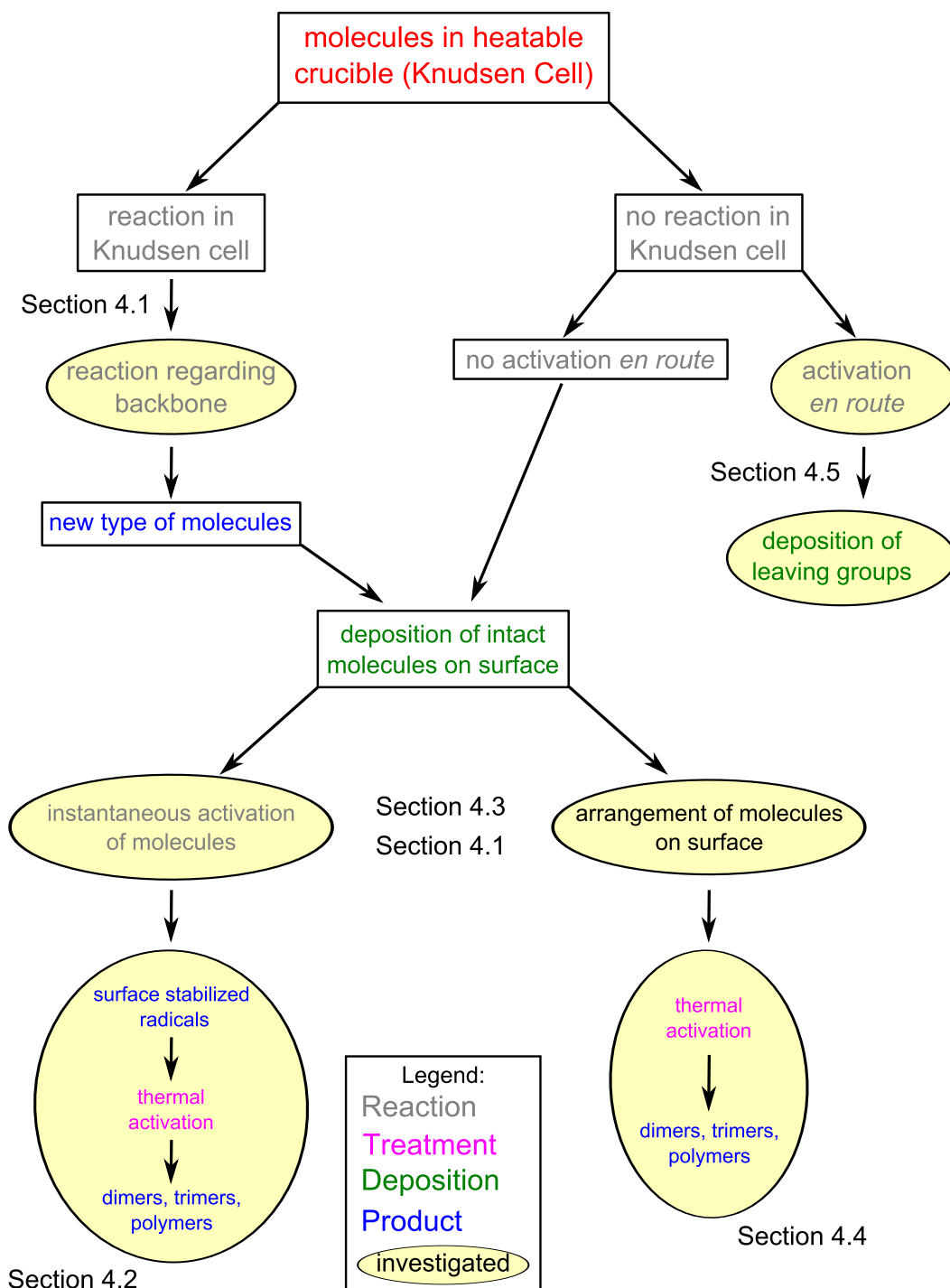
Figure 5.1: Overview of investigated different reaction pathways leading to two-dimensional polymers

List of Figures

References

[1] M. M. S. Abdel-Mottaleb, E. Gomar-Nadal, M. Surin, H. Uji-i, W. Mamdouh, J. Veciana, V. Lemaur, C. Rovira, J. Cornil, R. Lazzaroni, D. B. Amabilino, S. De Feyter, and F. C. De Schryver. Self-assembly of tetrathiafulvalene derivatives at a liquid/solid interface – compositional and constitutional influence on supramolecular ordering. *J. Mater. Chem.*, 15(43):4601–4615, 2005. URL: http://dx.doi.org/10.1039/B509336H.

[2] I. Alves, G. Demazeau, B. Tanguy, and F. Weill. On a new model of the graphitic form of C_3N_4. *Solid State Commun.*, 109(11):697–701, 1999. URL: http://dx.doi.org/10.1016/S0038-1098(98)00631-0.

[3] D. Armstrong and P. Perkins. The [small pi]-electronic structures of some compounds containing boron-oxygen bonds. Part II. Cyclic compounds. *J. Chem. Soc. (A)*, pages 790–792, 1967. URL: http://dx.doi.org/10.1039/J19670000790.

[4] D. Asturiol, M. Duran, and P. Salvador. Intramolecular basis set superposition error effects on the planarity of benzene and other aromatic molecules: A solution to the problem. *J. Chem. Phys.*, 128(14):144108, 2008. URL: http://link.aip.org/link/?JCP/128/144108/1.

[5] J. Bardeen. Tunnelling from a many-particle point of view. *Phys. Rev. Lett.*, 6(2):57–59, 1961. URL: http://dx.doi.org/10.1103/PhysRevLett.6.57.

[6] L. Bartels. Tailoring molecular layers at metal surfaces. *Nature Chem.*, 2(2):87–95, 2010. URL: http://dx.doi.org/10.1038/nchem.517.

[7] I. P. Batra, N. Garcia, H. Rohrer, H. Salemink, E. Stoll, and S. Ciraci. A study of graphite surface with STM and electronic structure calculations. *Surf. Sci.*, 181(2):126–138, 1987. URL: http://www.sciencedirect.com/science/article/pii/003960288790149X.

[8] A. D. Becke. Density-functional exchange-energy approximation with correct asymptotic behavior. *Phys. Rev. A*, 38:3098–3100, 1988. URL: http://link.aps.org/doi/10.1103/PhysRevA.38.3098.

[9] A. D. Becke. Density-functional thermochemistry. III. The role of exact exchange. *J. Chem. Phys.*, 98(7):5648–5652, 1993. URL: http://link.aip.org/link/?JCP/98/5648/1.

[10] A. D. Becke. A new mixing of hartree-fock and local density-functional theories. *J. Chem. Phys.*, 98(2):1372–1377, 1993. URL: http://link.aip.org/link/?JCP/98/1372/1.

[11] C. Benndorf and B. Krüger. Adsorption and reaction of bromine with Ag(110). *Surf. Sci.*, 151(1):271–288, 1985. URL: http://dx.doi.org/10.1016/0039-6028(85)90466-2.

[12] E. Bertel and F. F. Netzer. Adsorption of bromine on the reconstructed Au(100) surface: LEED, thermal desorption and work function measurements. *Surf. Sci.*, 97(2-3):409–424, 1980. URL: http://dx.doi.org/10.1016/0039-6028(80)90676-7.

[13] K. Besocke. An easily operable scanning tunneling microscope. *Surf. Sci.*, 181:145–153, 1987. URL: http://www.sciencedirect.com/science/article/pii/0039602887901518.

[14] M. Bieri, M. Nguyen, O. Gröning, J. Cai, M. Treier, K. Ait-Mansour, P. Ruffieux, C. Pignedoli, D. Passerone, M. Kastler, K. Müllen, and R. Fasel. Two-dimensional polymer formation on surfaces: Insight into the roles of precursor mobility and reactivity. *J. Am. Chem. Soc.*, 132:16669–16676, 2010. URL: http://dx.doi.org/10.1021/ja107947z.

[15] M. Bieri, M. Treier, J. Cai, K. Ait-Mansour, P. Ruffieux, O. Groning, P. Groning, M. Kastler, R. Rieger, X. Feng, K. Müllen, and R. Fasel. Porous graphenes: Two-dimensional polymer synthesis with atomic precision. *Chem. Commun.*, 45:6919–6921, 2009. URL: http://dx.doi.org/10.1039/b915190g.

[16] G. Binnig, H. Rohrer, C. Gerber, and E. Weibel. Surface studies by scanning tunneling microscopy. *Phys. Rev. Lett.*, 49(1):57–61, 1982. URL: http://dx.doi.org/10.1103/PhysRevLett.49.57.

[17] M. M. Blake, S. U. Nanayakkara, S. A. Claridge, L. C. Fernandez-Torres, E. C. H. Sykes, and P. S. Weiss. Identifying reactive intermediates in the Ullmann coupling reaction by scanning tunneling microscopy and spectroscopy. *J. Phys. Chem. A*, 113(47):13167–13172, 2009. URL: http://dx.doi.org/10.1021/jp903590c.

[18] S. Blankenburg, M. Bieri, R. Fasel, K. Müllen, C. A. Pignedoli, and D. Passerone. Porous graphene as an atmospheric nanofilter. *Small*, 6(20):2266–2271, 2010. URL: http://dx.doi.org/10.1002/smll.201001126.

[19] M. O. Blunt, J. C. Russell, N. R. Champness, and P. H. Beton. Templating molecular adsorption using a covalent organic framework. *Chem. Commun.*, 46(38):7157–7159, 2010. URL: http://dx.doi.org/10.1039/C0CC01810D.

[20] E. Bosch and C. Barnes. Triangular halogen-halogen-halogen interactions as a cohesive force in the structures of trihalomesitylenes. *Cryst. Growth Des.*, 2(4):299–302, 2002. URL: http://dx.doi.org/10.1021/cg025517w.

[21] G. Brunetto, P. A. d. S. Autreto, L. D. Machado, B. I. Santos, R. Santos, and D. S. Galvao. A nonzero gap two-dimensional carbon allotrope from porous graphene. *J. Phys. Chem. C*, 116(23):12810–12813, 2012. URL: http://dx.doi.org/10.1021/jp211300n.

[22] M. R. Bryce. Tetrathiafulvalenes as pi-electron donors for intramolecular charge-transfer materials. *Adv. Mater.*, 11(1):11–23, 1999. URL: http://dx.doi.org/10.1002/(SICI)1521-4095(199901)11:1<11::AID-ADMA11>3.0.CO;2-3.

[23] D. Canevet, M. Salle, G. Zhang, D. Zhang, and D. Zhu. Tetrathiafulvalene (TTF) derivatives: Key building-blocks for switchable processes. *Chem. Commun.*, 17:2245–2269, 2009. URL: http://dx.doi.org/10.1039/B818607N.

[24] W. H. Carothers. Studies on polymerization and ring formation. I. An introduction to the general theory of condensation polymers. *J. Am. Chem. Soc.*, 51(8):2548–2559, 1929. URL: http://pubs.acs.org/

doi/abs/10.1021/ja01383a041, arXiv:http://pubs.acs.org/doi/pdf/10.1021/ja01383a041.

[25] D. M. Ceperley and B. J. Alder. Ground state of the electron gas by a stochastic method. *Phys. Rev. Lett.*, 45:566–569, 1980. URL: http://link.aps.org/doi/10.1103/PhysRevLett.45.566.

[26] D. D. Chambliss, R. J. Wilson, and S. Chiang. Nucleation of ordered Ni island arrays on Au(111) by surface-lattice dislocations. *Phys. Rev. Lett.*, 66(13):1721–1724, 1991. URL: http://link.aps.org/doi/10.1103/PhysRevLett.66.1721.

[27] N. R. Champness. Surface chemistry: Making the right connections. *Nature Chem.*, 4(3):149–150, 2012. URL: http://dx.doi.org/10.1038/nchem.1276.

[28] C. J. Chen. Tunneling matrix elements in three-dimensional space: The derivative rule and the sum rule. *Phys. Rev. B*, 42:8841–8857, 1990. URL: http://link.aps.org/doi/10.1103/PhysRevB.42.8841.

[29] K.-H. Chung, J. Park, K. Y. Kim, J. K. Yoon, H. Kim, S. Han, and S.-J. Kahng. Polymorphic porous supramolecular networks mediated by halogen bonds on Ag(111). *Chem. Commun.*, 47(41):11492–11494, 2011. URL: http://dx.doi.org/10.1039/c1cc14679c.

[30] S. Clair, O. Ourdjini, M. Abel, and L. Porte. Two-dimensional polymer as a mask for surface nanopatterning. *Adv. Mater.*, 24(9):1252–1254, 2012. URL: http://dx.doi.org/10.1002/adma.201200063.

[31] T. Clark, M. Hennemann, J. Murray, and P. Politzer. Halogen bonding: The s-hole. *J. Mol. Model.*, 13(2):291–296, 2007. URL: http://dx.doi.org/10.1007/s00894-006-0130-2.

[32] A. J. Cohen, P. Mori-Sanchez, and W. Yang. Insights into current limitations of density functional theory. *Science*, 321(5890):792–794, 2008. URL: http://dx.doi.org/10.1126/science.1158722.

[33] M. Corso, W. Auwärter, M. Muntwiler, A. Tamai, T. Greber, and J. Osterwalder. Boron nitride nanomesh. *Science*, 303(5655):217–220, 2004. URL: http://www.sciencemag.org/content/303/5655/217.abstract, arXiv:http://www.sciencemag.org/content/303/5655/217.full.pdf.

[34] A. Cote, A. Benin, N. Ockwig, M. O'Keeffe, A. Matzger, and O. Yaghi. Porous, crystalline, covalent organic frameworks. *Science*, 310(5751):1166–1170, 2005. URL: http://dx.doi.org/10.1126/science.1120411.

[35] A. P. Cote, H. M. El-Kaderi, H. Furukawa, J. R. Hunt, and O. M. Yaghi. Reticular synthesis of microporous and mesoporous 2D covalent organic frameworks. *J. Am. Chem. Soc.*, 129(43):12914–12915, 2007. URL: http://dx.doi.org/10.1021/ja0751781.

[36] R. Criegee and R. Huber. Tetrachlor- und Tetrabrom-cyclobutadien als Zwischenprodukte. *Chem. Ber.*, 103(6):1862–1866, 1970. URL: http://dx.doi.org/10.1002/cber.19701030623.

[37] M. Döblinger, B. Lotsch, J. Wack, J. Thun, J. Senker, and W. Schnick. Structure elucidation of polyheptazine imide by electron diffraction – a templated 2D carbon nitride network. *Chem. Commun.*, 12(12):1541–1543, 2009. URL: http://dx.doi.org/10.1039/B820032G.

[38] J. F. Dienstmaier, A. M. Gigler, A. J. Goetz, P. Knochel, T. Bein, A. Lyapin, S. Reichlmaier, W. M. Heckl, and M. Lackinger. Synthesis of well-ordered COF monolayers: Surface growth of nanocrystalline precursors versus direct on-surface polycondensation. *ACS Nano*, 5(12):9737–9745, 2011. URL: http://pubs.acs.org/doi/abs/10.1021/nn2032616, arXiv: http://pubs.acs.org/doi/pdf/10.1021/nn2032616.

[39] A. Du, S. Sanvito, Z. Li, D. Wang, Y. Jiao, T. Liao, Q. Sun, Y. H. Ng, Z. Zhu, R. Amal, and S. C. Smith. Hybrid graphene and graphitic carbon nitride nanocomposite: Gap opening, electron-hole puddle, interfacial charge transfer, and enhanced visible light response. *J. Am. Chem. Soc.*, 134(9):4393–4397, 2012. URL: http://pubs.acs.org/doi/abs/10.1021/ja211637p, arXiv:http:// pubs.acs.org/doi/pdf/10.1021/ja211637p.

[40] A. Du, Z. Zhu, and S. C. Smith. Multifunctional porous graphene for nano-electronics and hydrogen storage: New properties revealed by first principle calculations. *J. Am. Chem. Soc.*, 132(9):2876–2877, 2010. URL: http://pubs. acs.org/doi/abs/10.1021/ja100156d, arXiv:http://pubs.acs.org/doi/ pdf/10.1021/ja100156d.

[41] O. Endo, H. Kondoh, and T. Ohta. Scanning tunneling microscope study of bromine adsorbed on the Ag(111) surface. *Surf. Sci.*, 441(2-3):L924–L930, 1999. URL: http://dx.doi.org/10.1016/S0039-6028(99)00914-0.

[42] J. M. Englert, C. Dotzer, G. Yang, M. Schmid, C. Papp, J. M. Gottfried, H.-P. Steinrück, E. Spiecker, F. Hauke, and A. Hirsch. Covalent bulk functionalization of graphene. *Nature Chem.*, 3(4):279–286, 2011. URL: http://dx.doi.org/ 10.1038/nchem.1010.

[43] G. Ertl. Reactions at surfaces: From atoms to complexity (Nobel Lecture). *Angew. Chem., Int. Ed.*, 47(19):3524–3535, 2008. URL: http://dx.doi.org/ 10.1002/anie.200800480.

[44] M. J. Farrall and J. M. J. Frechet. Bromination and lithiation: Two important steps in the functionalization of polystyrene resins. *J. Org. Chem.*, 41(24):3877–3882, 1976. URL: http://dx.doi.org/10.1021/jo00886a023.

[45] T. Faury, S. Clair, M. Abel, F. Dumur, D. Gigmes, and L. Porte. Sequential linking to control the growth of a surface covalent organic framework. *J. Phys. Chem. C*, 116(7):4819–4823, 2012. URL: http://pubs.acs.org/doi/abs/10.1021/ jp300417g, arXiv:http://pubs.acs.org/doi/pdf/10.1021/jp300417g.

[46] P. J. Flory. *Principles of Polymer Chemistry.* Cornell University Press, 1953. URL: http://www.cornellpress.cornell.edu/book/?GCOI= 80140100145700.

[47] M. J. Frisch, G. W. Trucks, H. B. Schlegel, G. E. Scuseria, M. A. Robb, J. R. Cheeseman, J. A. Montgomery, T. Vreven, K. N. Kudin, J. C. Burant, J. M. Millam, S. S. Iyengar, J. Tomasi, V. Barone, B. Mennucci, M. Cossi, G. Scalmani, N. Rega, G. A. Petersson, H. Nakatsuji, M. Hada, M. Ehara, K. Toyota, R. Fukuda, J. Hasegawa, M. Ishida, T. Nakajima, Y. Honda, O. Kitao, H. Nakai, M. Klene, X. Li, J. E. Knox, H. P. Hratchian, J. B. Cross, V. Bakken, C. Adamo, J. Jaramillo, R. Gomperts, R. E. Stratmann, O. Yazyev, A. J. Austin, R. Cammi, C. Pomelli, J. W. Ochterski, P. Y. Ayala, K. Morokuma, G. A. Voth, P. Salvador, J. J. Dannenberg, V. G. Zakrzewski, S. Dapprich, A. D. Daniels, M. C. Strain, O. Farkas, D. K. Malick, A. D. Rabuck, K. Raghavachari, J. B. Foresman, J. V. Ortiz, Q. Cui, A. G. Baboul, S. Clifford, J. Cioslowski, B. B. Stefanov, G. Liu, A. Liashenko, P. Piskorz,

I. Komaromi, R. L. Martin, D. J. Fox, T. Keith, A. M. A. Laham, C. Y. Peng, A. Nanayakkara, M. Challacombe, P. M. W. Gill, B. Johnson, W. Chen, M. W. Wong, C. Gonzalez, and J. A. Pople. Gaussian 03, Revision C.02, 2003. URL: http://www.gaussian.com/g_misc/g03/citation_g03.htm.

[48] M. J. Frisch, G. W. Trucks, H. B. Schlegel, G. E. Scuseria, M. A. Robb, J. R. Cheeseman, G. Scalmani, V. Barone, B. Mennucci, G. A. Petersson, H. Nakatsuji, M. Caricato, X. Li, H. P. Hratchian, A. F. Izmaylov, J. Bloino, G. Zheng, J. L. Sonnenberg, M. Hada, M. Ehara, K. Toyota, R. Fukuda, J. Hasegawa, M. Ishida, T. Nakajima, Y. Honda, O. Kitao, H. Nakai, T. Vreven, J. A. Montgomery, J. E. Peralta, F. Ogliaro, M. Bearpark, J. J. Heyd, E. Brothers, K. N. Kudin, V. N. Staroverov, R. Kobayashi, J. Normand, K. Raghavachari, A. Rendell, J. C. Burant, S. S. Iyengar, J. Tomasi, M. Cossi, N. Rega, J. M. Millam, M. Klene, J. E. Knox, J. B. Cross, V. Bakken, C. Adamo, J. Jaramillo, R. Gomperts, R. E. Stratmann, O. Yazyev, A. J. Austin, R. Cammi, C. Pomelli, J. W. Ochterski, R. L. Martin, K. Morokuma, V. G. Zakrzewski, G. A. Voth, P. Salvador, J. J. Dannenberg, S. Dapprich, A. D. Daniels, Farkas, J. B. Foresman, J. V. Ortiz, J. Cioslowski, and D. J. Fox. Gaussian 09, Revision B.01, 2009. URL: http://www.gaussian.com/g_tech/g_ur/m_citation.htm.

[49] J. Frohn, J. F. Wolf, K. Besocke, and M. Teske. Coarse tip distance adjustment and positioner for a scanning tunneling microscope. *Rev. Sci. Instrum.*, 60(6):1200–1201, 1989. URL: http://link.aip.org/link/?RSI/60/1200/1.

[50] A. K. Geim and K. S. Novoselov. The rise of graphene. *Nature Mater.*, 6(3):183–191, 2007. URL: http://dx.doi.org/10.1038/nmat1849.

[51] E. Gomar-Nadal, M. M. S. Abdel-Mottaleb, S. De Feyter, J. Veciana, C. Rovira, D. B. Amabilino, and F. C. De Schryver. Synthesis, separation, and isomer-dependent packing in two dimensions - detected by scanning tunnelling microscopy - of a TTF derivative. *Chem. Commun.*, 7:906–907, 2003. URL: http://dx.doi.org/10.1039/B300731F.

[52] A. D. Gottlieb and L. Wesoloski. Bardeen's tunnelling theory as applied to scanning tunnelling microscopy: A technical guide to the traditional interpretation. *Nanotechnology*, 17(8):R57–R65, 2006. URL: http://dx.doi.org/10.1088/0957-4484/17/8/R01.

[53] J. Goubeau and H. Keller. RAMAN Spektren und Struktur von Boroxol Verbindungen. *Z. Anorg. Allg. Chem.*, 272(5-6):303–312, 1953. URL: http://dx.doi.org/10.1002/zaac.19532720510.

[54] A. Gourdon. On surface covalent coupling in ultrahigh vacuum. *Angew. Chem., Int. Ed.*, 47(37):6950–6953, 2008. URL: http://dx.doi.org/10.1002/anie.200802229.

[55] L. Grill, M. Dyer, M. Lafferentz, L. Persson, M. V. Peters, and S. Hecht. Nano-architectures by covalent assembly of molecular building blocks. *Nature Nanotech.*, 2:687–691, 2007. URL: http://dx.doi.org/10.1038/nnano.2007.346.

[56] B. Grünbaum and G. C. Shephard. *Tilings and Patterns*. W. H. Freeman and Company, 1987.

[57] R. Gutzler, W. Heckl, and M. Lackinger. Combination of a Knudsen effusion cell with a quartz crystal microbalance: In situ measurement of molecular evaporation rates with a fully functional deposition source. *Rev. Sci. Instrum.*, 81:015108, 2010. URL: http://dx.doi.org/10.1063/1.3292510.

[58] R. Gutzler, S. Lappe, K. Mahata, M. Schmittel, W. Heckl, and M. Lackinger. Aromatic interaction vs. hydrogen bonding in self-assembly at the liquid–solid interface. *Chem. Commun.*, 6:680–682, 2009. URL: http://dx.doi.org/10.1039/B812890A.

[59] R. Gutzler, H. Walch, G. Eder, S. Kloft, W. M. Heckl, and M. Lackinger. Surface mediated synthesis of 2D covalent organic frameworks: 1,3,5-tris(4-bromophenyl)benzene on graphite(001), Cu(111), and Ag(110). *Chem. Commun.*, 29:4456–4458, 2009. URL: http://dx.doi.org/10.1039/B906836H.

[60] R. Haddon, T. Siegrist, R. Fleming, P. Bridenbaugh, and R. Laudise. Band structures of organic thin-film transistor materials. *J. Mater. Chem.*, 5(10):1719–1724, 1995. URL: http://pubs.rsc.org/en/content/articlepdf/1995/JM/JM9950501719.

[61] G. H. Haertling. Ferroelectric ceramics: History and technology. *J. Am. Ceram. Soc.*, 82(4):797–818, 1999. URL: http://dx.doi.org/10.1111/j.1151-2916.1999.tb01840.x.

[62] W. Haiss, J. K. Sass, X. Gao, and M. J. Weaver. Iodine adlayer structures on Au(111) as discerned by atomic-resolution scanning tunnelling microscopy: Relation to iodide electrochemical adsorption. *Surf. Sci.*, 274(3):593–598, 1992. URL: http://dx.doi.org/10.1016/0039-6028(92)90831-P.

[63] A. Hauschild, K. Karki, B. Cowie, M. Rohlfing, F. Tautz, and M. Sokolowski. Molecular distortions and chemical bonding of a large pi-conjugated molecule on a metal surface. *Phys. Rev. Lett.*, 94(3):36106, 2005. URL: http://link.aps.org/doi/10.1103/PhysRevLett.94.036106.

[64] G. Heyne. *Elektronische Messtechnik*. Oldenbourg Verlag, München, 1999. URL: http://www.oldenbourg-verlag.de/wissenschaftsverlag/elektronische-messtechnik/9783486249767.

[65] P. Hohenberg and W. Kohn. Inhomogeneous electron gas. *Phys. Rev.*, 136:B864–B871, 1964. URL: http://link.aps.org/doi/10.1103/PhysRev.136.B864.

[66] W. Huang, X. Ouyang, and L. J. Lee. High-performance nanopapers based on benzenesulfonic functionalized graphenes. *ACS Nano*, 6(11):10178–10185, 2012. URL: http://pubs.acs.org/doi/abs/10.1021/nn303917p.

[67] J. R. Hunt, C. J. Doonan, J. D. LeVangie, A. P. Cote, and O. M. Yaghi. Reticular synthesis of covalent organic borosilicate frameworks. *J. Am. Chem. Soc.*, 130(36):11872–11873, 2008. URL: http://dx.doi.org/10.1021/ja805064f.

[68] IBM. Made in IBM labs: IBM scientists demonstrate world's fastest graphene transistor, 2010. URL: http://www-03.ibm.com/press/us/en/pressrelease/29343.wss.

[69] J. Inukai, Y. Osawa, and K. Itaya. Adlayer structures of chlorine, bromine, and iodine on Cu(111) electrode in solution: In-situ STM and ex-situ LEED studies. *J. Phys. Chem. B*, 102(49):10034–10040, 1998. URL: http://dx.doi.org/10.1021/jp982952l.

[70] A. Ismach, H. Chou, D. A. Ferrer, Y. Wu, S. McDonnell, H. C. Floresca, A. Covacevich, C. Pope, R. Piner, M. J. Kim, R. M. Wallace, L. Colombo, and R. S. Ruoff. Toward the controlled synthesis of hexagonal boron nitride films. *ACS Nano*, 6(7):6378–6385, 2012. URL: http://pubs.acs.org/doi/abs/10.1021/nn301940k, arXiv:http://pubs.acs.org/doi/pdf/10.1021/nn301940k.

[71] G. A. Jeffrey. *An Introduction to Hydrogen Bonding.* Oxford University Press, 1997. URL: http://www.oup.com/us/catalog/general/subject/Chemistry/BiologicalChemistry/Crystallography/?view=usa&ci=9780195095494.

[72] I.-Y. Jeon, H.-J. Choi, S.-M. Jung, J.-M. Seo, M.-J. Kim, L. Dai, and J.-B. Baek. Large-scale production of edge-selectively functionalized graphene nanoplatelets via ball milling and their use as metal-free electrocatalysts for oxygen reduction reaction. *J. Am. Chem. Soc.*, 135(4):1386–1393, 2012. URL: http://dx.doi.org/10.1021/ja3091643.

[73] R. G. Jones and M. Kadodwala. Bromine adsorption on Cu(111). *Surf. Sci.*, 370:219–225, 1997. URL: http://www.sciencedirect.com/science/article/pii/S0039602896012988.

[74] W. Koch and M. C. Holthausen. *A Chemist's Guide to Density Functional Theory, 2nd Edition.* Wiley-VCH, 2nd edition, July 2001. URL: http://eu.wiley.com/WileyCDA/WileyTitle/productCd-3527303723.html.

[75] W. Kohn and L. J. Sham. Self-consistent equations including exchange and correlation effects. *Phys. Rev.*, 140:A1133–A1138, 1965. URL: http://link.aps.org/doi/10.1103/PhysRev.140.A1133.

[76] A. Korich and P. Iovine. Boroxine chemistry and applications: A perspective. *Dalton Trans.*, 39(6):1423–1431, 2010. URL: http://dx.doi.org/10.1039/B917043J.

[77] E. Kroke and M. Schwarz. Novel group 14 nitrides. *Coord. Chem. Rev.*, 248(5-6):493–532, 2004. URL: http://dx.doi.org/10.1016/j.ccr.2004.02.001.

[78] M. Lackinger and W. Heckl. Carboxylic acids: Versatile building blocks and mediators for two-dimensional supramolecular self-assembly. *Langmuir*, 25(19):11307–11321, 2009. URL: http://dx.doi.org/10.1021/la900785f.

[79] M. Lackinger and W. M. Heckl. A STM perspective on covalent intermolecular coupling reactions on surfaces. *J. Phys. D: Appl. Phys.*, 44(46):464011, 2011. URL: http://dx.doi.org/10.1088/0022-3727/44/46/464011.

[80] L. Lafferentz, V. Eberhardt, C. Dri, C. Africh, G. Comelli, F. Esch, S. Hecht, and L. Grill. Controlling on-surface polymerization by hierarchical and substrate-directed growth. *Nature Chem.*, 4:215–220, 2012. URL: http://dx.doi.org/10.1038/nchem.1242.

[81] I. Langmuir. The arrangement of electrons in atoms and molecules. *J. Am. Chem. Soc.*, 41(6):868–934, 1919. URL: http://pubs.acs.org/doi/abs/10.1021/ja02227a002, arXiv:http://pubs.acs.org/doi/pdf/10.1021/ja02227a002.

[82] A. Langner, S. L. Tait, N. Lin, C. Rajadurai, M. Ruben, and K. Kern. Self-recognition and self-selection in multicomponent supramolecular coordination networks on surfaces. *PNAS*, 104(46):17927–17930, 2007. URL: http://dx.doi.org/10.1073/pnas.0704882104.

[83] N. E. Levinger, P. H. Davis, and M. D. Fayer. Vibrational relaxation of the free terminal hydroxyl stretch in methanol oligomers: Indirect pathway to hydrogen bond breaking. *J. Chem. Phys.*, 115(20):9352–9360, 2001. URL: http://link.aip.org/link/?JCP/115/9352/1.

[84] Y. Li, Z. Zhou, P. Shen, and Z. Chen. Two-dimensional polyphenylene: experimentally available porous graphene as a hydrogen purification membrane. *Chem. Commun.*, 46(21):3672–3674, 2010. URL: http://dx.doi.org/10.1039/B926313F.

[85] N. Lin, A. Dmitriev, J. Weckesser, J. Barth, and K. Kern. Real-time single-molecule imaging of the formation and dynamics of coordination compounds. *Angew. Chem., Int. Ed.*, 41(24):4779–4783, 2002. URL: http://dx.doi.org/10.1002/anie.200290046.

[86] J. A. Lipton-Duffin, O. Ivasenko, D. F. Perepichka, and F. Rosei. Synthesis of polyphenylene molecular wires by surface-confined polymerization. *Small*, 5(5):592–597, 2009. URL: http://dx.doi.org/10.1002/smll.200801943.

[87] B. Lotsch and W. Schnick. Thermal conversion of guanylurea dicyanamide into graphitic carbon nitride via prototype CN_x precursors. *Chem. Mater.*, 17(15):3976–3982, 2005. URL: http://dx.doi.org/http://dx.doi.org/10.1021/cm050350q.

[88] B. Lotsch and W. Schnick. From triazines to heptazines: Novel nonmetal tricyanomelaminates as precursors for graphitic carbon nitride materials. *Chem. Mater.*, 18(7):1891–1900, 2006. URL: http://dx.doi.org/10.1021/cm052342f.

[89] Y. Lu, J. Zou, H. Wang, Q. Yu, H. Zhang, and Y. Jiang. Triangular halogen trimers. a DFT study of the structure, cooperativity, and vibrational properties. *J. Phys. Chem. A*, 109(51):11956–11961, 2005. URL: http://dx.doi.org/10.1021/jp0547360.

[90] A. G. MacDiarmid. Synthetic metals: A novel role for organic polymers (Nobel Lecture). *Angew. Chem., Int. Ed.*, 40(14):2581–2590, 2001. URL: http://dx.doi.org/10.1002/1521-3773(20010716)40:14<2581::AID-ANIE2581>3.0.CO;2-2.

[91] A. L. Mackay. Extensions of space-group theory. *Acta Crystallogr.*, 10(9):543–548, 1957. URL: http://dx.doi.org/10.1107/S0365110X57001966.

[92] H. Margenau. Van der Waals forces. *Rev. Mod. Phys.*, 11(1):1–35, 1939. URL: http://dx.doi.org/10.1103/RevModPhys.11.1.

[93] R. Mas-Balleste, C. Gómez-Navarro, J. Gómez-Herrero, and F. Zamora. 2D materials: To graphene and beyond. *Nanoscale*, 3(1):20–30, 2011. URL: http://dx.doi.org/10.1039/C0NR00323A.

[94] A. E. Mattsson. In pursuit of the "divine" functional. *Science*, 298(5594):759–760, 2002. URL: http://www.sciencemag.org/content/298/5594/759.short, arXiv:http://www.sciencemag.org/content/298/5594/759.full.pdf.

[95] G. S. McCarty and P. S. Weiss. Formation and manipulation of protopolymer chains. *J. Am. Chem. Soc.*, 126(51):16772–16776, 2004. URL: http://dx.doi.org/10.1021/ja038930g.

[96] D. F. McMillen and D. M. Golden. Hydrocarbon bond dissociation energies. *Annu. Rev. Phys. Chem.*, 33(1):493–532, 1982. URL: http://www.annualreviews.org/doi/abs/10.1146/annurev.pc.33.100182.002425.

[97] A. McNaught and A. Wilkinson. *IUPAC Compendium of Chemical Terminology - the Gold Book*. Blackwell Scientific Publications, 2nd edition, 1997. URL: http://goldbook.iupac.org.

[98] T. Michinobu. Adapting semiconducting polymer doping techniques to create new types of click postfunctionalization. *Chem. Soc. Rev.*, 40(5):2306–2316, 2011. URL: http://dx.doi.org/10.1039/C0CS00205D.

[99] I. Mills, T. Cvitas, K. Homann, N. Kallay, and K. Kuchitsu. *Quantities, Units and Symbols in Physical Chemistry*. Blackwell Science, 2nd edition, 1993. URL: http://old.iupac.org/publications/books/gbook/green_book_2ed.pdf.

[100] T. Müller, G. W. Flynn, A. T. Mathauser, and A. V. Teplyakov. Temperature-programmed desorption studies of n-alkane derivatives on graphite: Desorption energetics and the influence of functional groups on adsorbate self-assembly. *Langmuir*, 19(7):2812–2821, 2003. URL: http://dx.doi.org/10.1021/la020856c.

[101] A. Morgan, J. Jurs, and J. Tour. Synthesis, flame-retardancy testing, and preliminary mechanism studies of nonhalogenated aromatic boronic acids: A new class of condensed-phase polymer flame-retardant additives for acrylonitrile-butadiene-styrene and polycarbonate. *J. Appl. Polym. Sci.*, 76(8):1257–1268, 2000. URL: http://dx.doi.org/10.1002/(SICI)1097-4628(20000523)76:8<1257::AID-APP6>3.0.CO;2-#.

[102] C. Nakakura and E. Altman. Bromine adsorption, reaction, and etching of Cu(100). *Surf. Sci.*, 370(1):32–46, 1996. URL: http://dx.doi.org/10.1016/S0039-6028(96)00950-8.

[103] D. Necas and P. Klapetek. Gwyddion - a free SPM data analysis software, 2012. URL: http://gwyddion.net/.

[104] D. J. Nelson and C. N. Brammer. Toward consistent terminology for cyclohexane conformers in introductory organic chemistry. *J. Chem. Educ.*, 88(3):292–294, 2011. URL: http://pubs.acs.org/doi/abs/10.1021/ed100172k, arXiv:http://pubs.acs.org/doi/pdf/10.1021/ed100172k.

[105] A. Neumann, K. Christmann, and T. Solomun. Binding states and structural phase transformations upon iodine adsorption on a gold (100) surface. *Surf. Sci.*, 287:593–599, 1993. URL: http://dx.doi.org/10.1016/0039-6028(93)91034-M.

[106] M.-T. Nguyen, C. A. Pignedoli, and D. Passerone. An *ab initio* insight into the Cu(111)-mediated Ullmann reaction. *Phys. Chem. Chem. Phys.*, 13(1):154–160, 2011. URL: http://dx.doi.org/10.1039/c0cp00759e.

[107] Nobelprize.org. The nobel prize in physics 2010, 2010. 24 Jan 2013. URL: http://www.nobelprize.org/nobel_prizes/physics/laureates/2010/.

[108] K. S. Novoselov. Nobel lecture: Graphene: Materials in the flatland. *Rev. Mod. Phys.*, 83:837–849, 2011. URL: http://link.aps.org/doi/10.1103/RevModPhys.83.837.

[109] J. Paier, M. Marsman, and G. Kresse. Why does the B3LYP hybrid functional fail for metals? *J. Chem. Phys.*, 127(2):024103, 2007. URL: http://link.aip.org/link/?JCP/127/024103/1.

[110] J. Park, K. Y. Kim, K.-H. Chung, J. K. Yoon, H. Kim, S. Han, and S.-J. Kahng. Interchain interactions mediated by br adsorbates in arrays of metal-organic hybrid chains on Ag(111). *J. Phys. Chem. C*, 115(30):14834–14838, 2011. URL: http://dx.doi.org/10.1021/jp203129f.

[111] J. Pellon, L. H. Schwind, M. J. Guinard, and W. M. Thomas. Polymerization of vinyl monomers containing boron II. P-vinylphenylboronic acid. *J. Polym. Sci.*, 55(161):161–167, 1961. URL: http://dx.doi.org/10.1002/pol.1961.1205516117.

[112] J. Perdew, K. Burke, and M. Ernzerhof. Generalized gradient approximation made simple. *Phys. Rev. Lett.*, 77(18):3865–3868, 1996. URL: http://link.aps.org/doi/10.1103/PhysRevLett.77.3865.

[113] J. Perdew and Y. Wang. Accurate and simple analytic representation of the electron-gas correlation energy. *Phys. Rev. B*, 45(23):13244–13249, 1992. URL: http://link.aps.org/doi/10.1103/PhysRevB.45.13244.

[114] J. P. Perdew, S. Kurth, A. Zupan, and P. Blaha. Accurate density functional with correct formal properties: A step beyond the generalized gradient approximation. *Phys. Rev. Lett.*, 82:2544–2547, 1999. URL: http://link.aps.org/doi/10.1103/PhysRevLett.82.2544.

[115] J. P. Perdew, A. Ruzsinszky, J. Tao, V. N. Staroverov, G. E. Scuseria, and G. I. Csonka. Prescription for the design and selection of density functional approximations: More constraint satisfaction with fewer fits. *J. Chem. Phys.*, 123(6):062201, 2005. URL: http://link.aip.org/link/?JCP/123/062201/1.

[116] J. P. Perdew and A. Zunger. Self-interaction correction to density-functional approximations for many-electron systems. *Phys. Rev. B*, 23:5048–5079, 1981. URL: http://link.aps.org/doi/10.1103/PhysRevB.23.5048.

[117] D. F. Perepichka and F. Rosei. Extending polymer conjugation into the second dimension. *Science*, 323(5911):216–217, 2009. URL: http://dx.doi.org/10.1126/science.1165429, arXiv:http://www.sciencemag.org/cgi/reprint/323/5911/216.pdf.

[118] P. Politzer, J. S. Murray, and T. Clark. Halogen bonding: An electrostatically-driven highly directional noncovalent interaction. *Phys. Chem. Chem. Phys.*, 12(28):7748–7757, 2010. URL: http://dx.doi.org/10.1039/c004189k.

[119] V. Pophristic and L. Goodman. Hyperconjugation not steric repulsion leads to the staggered structure of ethane. *Nature*, 411(6837):565–568, 2001. URL: http://dx.doi.org/10.1038/35079036.

[120] P. Price. Standard definitions of terms relating to mass spectrometry. *J. Am. Soc. Mass Spectrom.*, 2:336–348, 1991. URL: http://dx.doi.org/10.1016/1044-0305(91)80025-3.

[121] S. L. Price, A. J. Stone, J. Lucas, R. S. Rowland, and A. E. Thornley. The nature of -Cl...Cl- intermolecular interactions. *J. Am. Chem. Soc.*, 116(11):4910–4918, 1994. URL: http://dx.doi.org/10.1021/ja00090a041.

[122] J. Puigmarti-Luis, A. Minoia, S. Lei, V. Geskin, B. Li, R. Lazzaroni, S. De Feyter, and D. B. Amabilino. Self-assembly of supramolecular wires and cross-junctions and efficient electron tunnelling across them. *Chem. Sci.*, 2(10):1945–1951, 2011. URL: http://dx.doi.org/10.1039/C1SC00330E.

[123] J. Rabe and S. Buchholz. Commensurability and mobility in two-dimensional molecular patterns on graphite. *Science*, 253(5018):424, 1991. URL: http://dx.doi.org/10.1126/science.253.5018.424.

[124] K. E. Riley and P. Hobza. Investigations into the nature of halogen bonding including symmetry adapted perturbation theory analyses. *J. Chem. Theory Comput.*, 4(2):232–242, 2008. URL: http://dx.doi.org/10.1021/ct700216w.

[125] J. D. Roberts, A. Streitwieser, and C. M. Regan. Small-ring compounds. X. Molecular orbital calculations of properties of some small-ring hydrocarbons and free radicals. *J. Am. Chem. Soc.*, 74(18):4579–4582, 1952. URL: http://dx.doi.org/10.1021/ja01138a038.

[126] Z. Rong and P. Kuiper. Electronic effects in scanning tunneling microscopy: Moirè pattern on a graphite surface. *Phys. Rev. B*, 48(23):17427, 1993. URL: http://link.aps.org/doi/10.1103/PhysRevB.48.17427.

[127] T. Sainsbury, A. Satti, P. May, Z. Wang, I. T. McGovern, Y. K. Gun'Ko, and J. N. Coleman. Oxygen radical functionalization of boron nitride nanosheets. *J. Am. Chem. Soc.*, 134(45):18758–18771, 2012. URL: http://pubs.acs.org/doi/abs/10.1021/ja3080665.

[128] J. Sakamoto, J. van Heijst, O. Lukin, and A. Schlüter. Two-dimensional polymers: Just a dream of synthetic chemists? *Angew. Chem., Int. Ed.*, 48(6):1030–1069, 2009. URL: http://dx.doi.org/10.1002/anie.200801863.

[129] S. Schlögl, W. M. Heckl, and M. Lackinger. On-surface radical addition of triply iodinated monomers on Au(111) - the influence of monomer size and thermal post-processing. *Surf. Sci.*, 606(13-14):999–1004, 2012. URL: http://www.sciencedirect.com/science/article/pii/S0039602812000623.

[130] S. Schlögl, T. Sirtl, J. Eichhorn, W. M. Heckl, and M. Lackinger. Synthesis of two-dimensional phenylene-boroxine networks through *in vacuo* condensation and on-surface radical addition. *Chem. Commun.*, 47(45):12355–12357, 2011. URL: http://dx.doi.org/10.1039/C1CC13896K.

[131] U. Schlickum, R. Decker, F. Klappenberger, G. Zoppellaro, S. Klyatskaya, M. Ruben, I. Silanes, A. Arnau, K. Kern, H. Brune, and J. V. Barth. Metal-organic honeycomb nanomeshes with tunable cavity size. *Nano Lett.*, 7(12):3813–3817, 2007. URL: http://dx.doi.org/10.1021/nl072466m.

[132] C. H. Schmitz, J. Ikonomov, and M. Sokolowski. Two-dimensional ordering of poly(p-phenylene-terephthalamide) on the Ag(111) surface investigated by scanning tunneling microscopy. *J. Phys. Chem. C*, 113(28):11984–11987, 2009. URL: http://dx.doi.org/10.1021/jp9041777.

[133] H. Schniepp, J. Li, M. McAllister, H. Sai, M. Herrera-Alonso, D. Adamson, R. Prud'homme, R. Car, D. Saville, and I. Aksay. Functionalized single graphene sheets derived from splitting graphite oxide. *J. Phys. Chem. B*, 110(17):8535–8539, 2006. URL: http://dx.doi.org/10.1021/jp060936f.

[134] J. H. Schott and H. S. White. Halogen adlayers on Ag(111). *J. Phys. Chem.*, 98(1):291–296, 1994. URL: http://dx.doi.org/10.1021/j100052a049.

[135] M. G. Schwab, A. Narita, Y. Hernandez, T. Balandina, K. S. Mali, S. De Feyter, X. Feng, and K. Müllen. Structurally defined graphene nanoribbons with high lateral extension. *J. Am. Chem. Soc.*, 134(44):18169–18172, 2012. URL: http://pubs.acs.org/doi/abs/10.1021/ja307697j.

[136] P. F. H. Schwab, M. D. Levin, and J. Michl. Molecular rods. 1. Simple axial rods. *Chem. Rev.*, 99(7):1863–1934, 1999. URL: http://pubs.acs.org/doi/abs/10.1021/cr970070x, arXiv:http://pubs.acs.org/doi/pdf/10.1021/cr970070x.

[137] M. Segall, P. Lindan, M. Probert, C. Pickard, P. Hasnip, S. Clark, and M. Payne. First-principles simulation: Ideas, illustrations and the CASTEP code. *J. Phys.: Condens. Matter*, 14:2717–2744, 2002. URL: http://dx.doi.org/10.1088/0953-8984/14/11/301.

[138] J. L. Segura and N. Martin. New concepts in tetrathiafulvalene chemistry. *Angew. Chem., Int. Ed.*, 40(8):1372–1409, 2001. URL: http://dx.doi.org/10.1002/1521-3773(20010417)40:8<1372::AID-ANIE1372>3.0.CO;2-I.

[139] D. Sherrill. Counterpoise correction and basis set superposition error, 2010. URL: http://vergil.chemistry.gatech.edu/notes/cp.pdf.

[140] F. Silly. Moire pattern induced by the electronic coupling between 1-octanol self-assembled monolayers and graphite surface. *Nanotechnology*, 23(22):225603–225609, 2012. URL: http://stacks.iop.org/0957-4484/23/i=22/a=225603.

[141] S. Simon, M. Duran, and J. J. Dannenberg. How does basis set superposition error change the potential surfaces for hydrogen-bonded dimers? *J. Chem. Phys.*, 105(24):11024–11031, 1996. URL: http://link.aip.org/link/?JCP/105/11024/1.

[142] M. Sparks, G. K. Teal, and N. Summit. Method of making p-n junctions in semiconductor materials, March 1953. US Patent 2631356. URL: http://www.google.com/patents?id=Di5JAAAAEBAJ&pg=PA1&hl=de&source=gbs_selected_pages&cad=1#v=onepage&q&f=false.

[143] S. Stepanow, N. Lin, D. Payer, U. Schlickum, F. Klappenberger, G. Zoppellaro, M. Ruben, H. Brune, J. Barth, and K. Kern. Surface-assisted assembly of 2D metal–organic networks that exhibit unusual threefold coordination symmetry. *Angew. Chem., Int. Ed.*, 119(5):724–727, 2007. URL: http://dx.doi.org/10.1002/ange.200603644.

[144] B. C. Stipe, M. A. Rezaei, and W. Ho. A variable-temperature scanning tunneling microscope capable of single-molecule vibrational spectroscopy. *Rev. Sci. Instrum.*, 70(1):137–143, 1999. URL: http://dx.doi.org/10.1063/1.1149555.

[145] D. Syomin, J. Kim, B. E. Koel, and G. B. Ellison. Identification of adsorbed phenyl (C_6H_5) groups on metal surfaces: Electron-induced dissociation of benzene on Au(111). *J. Phys. Chem. B*, 105(35):8387–8394, 2001. URL: http://dx.doi.org/10.1021/jp012069e.

[146] H. Tang and S. Ismail-Beigi. Novel precursors for boron nanotubes: The competition of two-center and three-center bonding in boron sheets. *Phys. Rev. Lett.*, 99(11):115501, 2007. URL: http://link.aps.org/doi/10.1103/PhysRevLett.99.115501.

[147] H. Tang and S. Ismail-Beigi. Self-doping in boron sheets from first principles: A route to structural design of metal boride nanostructures. *Phys. Rev. B*, 80(13):134113, 2009. URL: http://link.aps.org/doi/10.1103/PhysRevB.80.134113.

[148] J. Tao, J. P. Perdew, A. Ruzsinszky, G. E. Scuseria, G. I. Csonka, and V. N. Staroverov. Meta-generalized gradient approximation: Non-empirical construction and performance of a density functional. *Philos. Mag.*, 87(7):1071–1084, 2007. URL: http://www.tandfonline.com/doi/abs/10.1080/14786430601021660, arXiv:http://www.tandfonline.com/doi/pdf/10.1080/14786430601021660.

[149] R. C. Tatar and S. Rabii. Electronic properties of graphite: A unified theoretical study. *Phys. Rev. B*, 25(6):4126–4141, 1982. URL: http://link.aps.org/doi/10.1103/PhysRevB.25.4126.

[150] J. Tersoff and D. R. Hamann. Theory and application for the scanning tunneling microscope. *Phys. Rev. Lett.*, 50(25):1998–2001, 1983. URL: http://dx.doi.org/10.1103/PhysRevLett.50.1998.

[151] U. Tietze and C. Schenk. *Halbleiter- Schaltungstechnik*. Springer Verlag, Berlin, 1993. URL: http://www.tietze-schenk.de/.

[152] M. Topsakal and S. Ciraci. Elastic and plastic deformation of graphene, silicene, and boron nitride honeycomb nanoribbons under uniaxial tension: A first-principles density-functional theory study. *Phys. Rev. B*, 81(2):024107, 2010. URL: http://link.aps.org/doi/10.1103/PhysRevB.81.024107.

[153] M. Treier, C. A. Pignedoli, T. Laino, R. Rieger, K. Müllen, D. Passerone, and R. Fasel. Surface-assisted cyclodehydrogenation provides a synthetic route towards easily processable and chemically tailored nanographenes. *Nature Chem.*, 3(1):61–67, 2011. URL: http://dx.doi.org/10.1038/nchem.891.

[154] F. Ullmann and J. Bielecki. Über Synthesen in der Biphenylreihe. *Ber. Dtsch. Chem. Ges.*, 34(2):2174–2185, 1901. URL: http://dx.doi.org/10.1002/cber.190103402141.

[155] H. Valdes, V. Klusak, M. Pitonak, O. Exner, I. Stary, P. Hobza, and L. Rulisek. Evaluation of the intramolecular basis set superposition error in the calculations of larger molecules: [n]helicenes and phe-gly-phe tripeptide. *J. Comput. Chem.*, 29(6):861–870, 2008. URL: http://dx.doi.org/10.1002/jcc.20841.

[156] H. Walch, R. Gutzler, T. Sirtl, G. Eder, and M. Lackinger. Material- and orientation-dependent reactivity for heterogeneously catalyzed carbon-bromine bond homolysis. *J. Phys. Chem. C*, 114(29):12604–12609, 2010. URL: http://dx.doi.org/10.1021/jp102704q.

[157] Z. Wang, H. Ni, C. Zhao, X. Li, G. Zhang, K. Shao, and H. Na. Influence of the hydroquinone with different pendant groups on physical and electro-chemical behaviors of directly polymerized sulfonated poly(ether ether sulfone) copolymers for proton exchange membranes. *J. Membr. Sci.*, 285(1-2):239–248, 2006. URL: http://www.sciencedirect.com/science/article/pii/S0376738806005795.

[158] S. Weigelt, C. Busse, C. Bombis, M. Knudsen, K. Gothelf, E. Lagsgaard, F. Besenbacher, and T. Linderoth. Surface synthesis of 2D branched polymer nanostructures. *Angew. Chem., Int. Ed.*, 47(23):4406–4410, 2008. URL: http://dx.doi.org/10.1002/anie.200705079.

[159] F. Weinhold. Chemistry: A new twist on molecular shape. *Nature*, 411(6837):539–541, 2001. URL: http://dx.doi.org/10.1038/35079225.

[160] M. Wieser. Atomic weights of the elements 2005. *Pure Appl. Chem*, 78(11):2051–2066, 2006. URL: http://www.iupac.org/publications/pac/78/11/2051/.

[161] J. Wintterlin and M. Bocquet. Graphene on metal surfaces. *Surf. Sci.*, 603(10-12):1841–1852, 2009. URL: http://dx.doi.org/10.1016/j.susc.2008.08.037.

[162] J. Xhie, K. Sattler, M. Ge, and N. Venkateswaran. Giant and supergiant lattices on graphite. *Phys. Rev. B*, 47(23):15835, 1993. URL: http://link.aps.org/doi/10.1103/PhysRevB.47.15835.

[163] M. Xi and B. E. Bent. Mechanisms of the Ullmann coupling reaction in adsorbed monolayers. *J. Am. Chem. Soc.*, 115(16):7426–7433, 1993. URL: http://dx.doi.org/10.1021/ja00069a048.

[164] J. Yates Jr and L. Rubin. Experimental innovations in surface science: A guide to practical laboratory methods and instruments. *Phys. Today*, 51:66, 1998. URL: http://www.physicstoday.org/resource/1/phtoad/v51/i8/p66_s1?isAuthorized=no.

[165] Y. Zhang, X. Xu, and W. A. Goddard. Doubly hybrid density functional for accurate descriptions of nonbond interactions, thermochemistry, and thermochemical kinetics. *PNAS*, 106(13):4963–4968, 2009. URL: http://www.pnas.org/content/106/13/4963.abstract, arXiv:http://www.pnas.org/content/106/13/4963.full.pdf+html.

[166] M. Zhong, S. Natesakhawat, J. P. Baltrus, D. Luebke, H. Nulwala, K. Matyjaszewski, and T. Kowalewski. Copolymer-templated nitrogen-enriched porous nanocarbons for CO_2 capture. *Chem. Commun.*, 48(94):11516–11518, 2012. URL: http://dx.doi.org/10.1039/C2CC36652E.

[167] N. Zwaneveld, R. Pawlak, M. Abel, D. Catalin, D. Gigmes, D. Bertin, and L. Porte. Organized formation of 2D extended covalent organic frameworks at surfaces. *J. Am. Chem. Soc.*, 130(21):6678–6679, 2008. URL: http://dx.doi.org/10.1021/ja800906f.

Acknowledgments - Danksagung